DESIGN AND MODELLING OF INTERDIGITATED AND NANOSTRUCTURED POLYMER SOLAR CELLS

Pedro Granero Secilla

Dipòsit Legal: T 891-2015

ADVERTIMENT. L'accés als continguts d'aquesta tesi doctoral i la seva utilització ha de respectar els drets de la persona autora. Pot ser utilitzada per a consulta o estudi personal, així com en activitats o materials d'investigació i docència en els termes establerts a l'art. 32 del Text Refós de la Llei de Propietat Intel·lectual (RDL 1/1996). Per altres utilitzacions es requereix l'autorització prèvia i expressa de la persona autora. En qualsevol cas, en la utilització dels seus continguts caldrà indicar de forma clara el nom i cognoms de la persona autora i el títol de la tesi doctoral. No s'autoritza la seva reproducció o altres formes d'explotació efectuades amb finalitats de lucre ni la seva comunicació pública des d'un lloc aliè al servei TDX. Tampoc s'autoritza la presentació del seu contingut en una finestra o marc aliè a TDX (framing). Aquesta reserva de drets afecta tant als continguts de la tesi com als seus resums i índexs.

ADVERTENCIA. El acceso a los contenidos de esta tesis doctoral y su utilización debe respetar los derechos de la persona autora. Puede ser utilizada para consulta o estudio personal, así como en actividades o materiales de investigación y docencia en los términos establecidos en el art. 32 del Texto Refundido de la Ley de Propiedad Intelectual (RDL 1/1996). Para otros usos se requiere la autorización previa y expresa de la persona autora. En cualquier caso, en la utilización de sus contenidos se deberá indicar de forma clara el nombre y apellidos de la persona autora y el título de la tesis doctoral. No se autoriza su reproducción u otras formas de explotación efectuadas con fines lucrativos ni su comunicación pública desde un sitio ajeno al servicio TDR. Tampoco se autoriza la presentación de su contenido en una ventana o marco ajeno a TDR (framing). Esta reserva de derechos afecta tanto al contenido de la tesis como a sus resúmenes e índices.

WARNING. Access to the contents of this doctoral thesis and its use must respect the rights of the author. It can be used for reference or private study, as well as research and learning activities or materials in the terms established by the 32nd article of the Spanish Consolidated Copyright Act (RDL 1/1996). Express and previous authorization of the author is required for any other uses. In any case, when using its content, full name of the author and title of the thesis must be clearly indicated. Reproduction or other forms of for profit use or public communication from outside TDX service is not allowed. Presentation of its content in a window or frame external to TDX (framing) is not authorized either. These rights affect both the content of the thesis and its abstracts and indexes.

UNIVERSITAT ROVIRA I VIRGILI
DESIGN AND MODELLING OF INTERDIGITATED AND NANOSTRUCTURED POLYMER SOLAR CELLS
Pedro Granero Secilla
Dipòsit Legal: T 891-2015

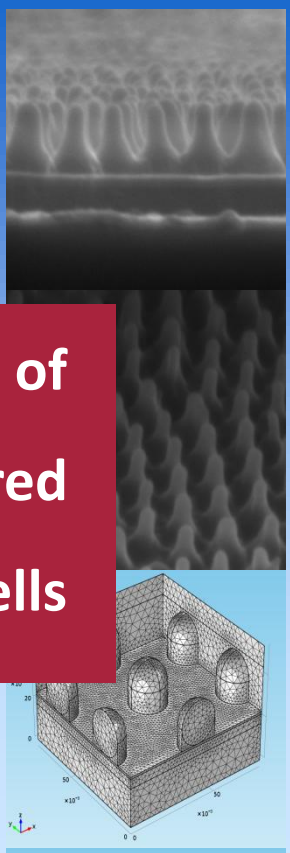

Design and Modelling of Interdigitated and Nanostructured Polymer Solar Cells

Ph. D. Thesis

Pedro Granero Secilla

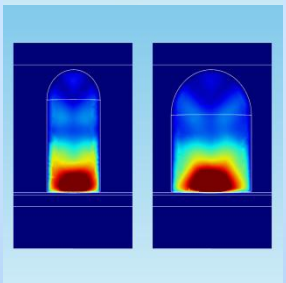

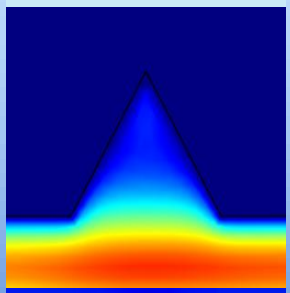

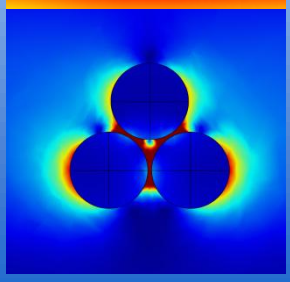

UNIVERSITAT ROVIRA I VIRGILI
Department of Electronic, Electrical and Automatic Control Engineering

UNIVERSITAT ROVIRA I VIRGILI
DESIGN AND MODELLING OF INTERDIGITATED AND NANOSTRUCTURED POLYMER SOLAR CELLS
Pedro Granero Secilla
Dipòsit Legal: T 891-2015

UNIVERSITAT ROVIRA I VIRGILI
DESIGN AND MODELLING OF INTERDIGITATED AND NANOSTRUCTURED POLYMER SOLAR CELLS
Pedro Granero Secilla
Dipòsit Legal: T 891-2015

UNIVERSITAT ROVIRA I VIRGILI
DESIGN AND MODELLING OF INTERDIGITATED AND NANOSTRUCTURED POLYMER SOLAR CELLS
Pedro Granero Secilla
Dipòsit Legal: T 891-2015

UNIVERSITAT ROVIRA I VIRGILI
DESIGN AND MODELLING OF INTERDIGITATED AND NANOSTRUCTURED POLYMER SOLAR CELLS
Pedro Granero Secilla
Dipòsit Legal: T 891-2015

Pedro Granero Secilla

Design and modelling of interdigitated and nanostructured polymer solar cells

Ph. D. Thesis

Supervised by

Dr. Lluís Francesc Marsal Garví

&

Dr. Josep Ferré-Borrull

Department of Electronic, Electrical and Automatic Control Engineering

Nano-Electronic and Photonic Systems (NePhoS)

UNIVERSITAT ROVIRA I VIRGILI

Tarragona

2015

UNIVERSITAT ROVIRA I VIRGILI
DESIGN AND MODELLING OF INTERDIGITATED AND NANOSTRUCTURED POLYMER SOLAR CELLS
Pedro Granero Secilla
Dipòsit Legal: T 891-2015

UNIVERSITAT ROVIRA I VIRGILI

Departament d'Enginyeria Electrònica, Elèctrica i Automàtica
Escola Tècnica Superior D'Enginyeria
Campus Sescelades
Avinguda dels Països Catalans, 26
43007 Tarragona
Espanya
Tel.: + 34 977 559 610 / 559 728
Fax: + 34 977 559 605

We, Lluís Francesc Marsal Garví and Josep Ferré-Borrull, full and aggregate professor, respectively, of the Departament of Electronic, Electrical and Automatic Control Engineering of the Universitat Rovira i Virgili,

CERTIFY:

That the present study, entitled "Design and modelling of interdigitated and nanostructured polymer solar cells", presented by Pedro Granero Secilla for the award of the degree of Doctor, has been carried out under our supervision at the Department of Electronic, Electrical and Automatic Control Engineering of this university, and that it fulfils all the requirements to be eligible for the International Doctorate Award.

Tarragona, 2nd March 2015

Doctoral Thesis Supervisors

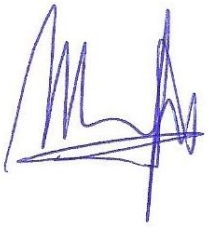

Lluís Francesc Marsal Garví

Josep Ferré-Borrull

UNIVERSITAT ROVIRA I VIRGILI
DESIGN AND MODELLING OF INTERDIGITATED AND NANOSTRUCTURED POLYMER SOLAR CELLS
Pedro Granero Secilla
Dipòsit Legal: T 891-2015

Acknowledgements

La presentación de esta tesis es la culminación de toda una vida dedicada al estudio. Una vida de esfuerzo y dedicación llena de sus más y sus menos. Afortunadamente no se ha tratado de una vida en solitario. Hay mucha gente a la que hay que agradecer su ayuda, ya sea en la propia realización de este trabajo, ya que aunque esté al nombre de uno una tesis es un trabajo de equipo, o por su apodo moral.

En primer lugar quisiera agradecer a mis directores de tesis su inestimable ayuda. Al Dr. Lluís Francesc Marsal, que en su día decidió darme la oportunidad de trabajar en su grupo de investigación. Su apoyo y ánimos siempre han sido de gran ayuda. Es de agradecer también su confianza al permitirme ir a muchos congresos para poder exponer mi, nuestro, trabajo. Al Dr. Josep Ferré-Borrull, que un buen día me hizo una proposición más que decente mientras esperaba en la cola de la secretaria del departamento: hacer un doctorado. Recibí su propuesta como un regalo del cielo. Estaba interesado en el tema, pero no sabía muy bien por dónde empezar a mirar. Espero que haya sido una buena inversión para él. No siempre es fácil trabajar con alguien tan independiente como yo. Aún así, el trato recibido, su paciencia y su ayuda han sido inmejorables.

Especial mención también a todos los profesores que han pasado por mi vida a lo largo de todos estos años, no podría nombrarlos a todos. He procurado llevarme un poco de cada uno de ellos en forma de conocimientos de todo tipo. Conocimientos para saciar mi sed de saber. A parte de conocimiento, también me llevé algo más de uno de ellos. Me refiero a Xema Campos, del IES Vila-seca. Dar clase es fácil, enseñar, no tanto, educar, menos. Y si todo el mundo recuerda a este profesor muchos años después de haber pasado por sus clases, por algo será. Quisiera agradecerle también

que estos últimos años se haya dedicado a educar tan bien como lo hizo conmigo a mi sobrino Xavi Fuertes. Me habla mucho de usted y me explica cosas que le enseña que yo no sabía o que ya no recordaba bien. Así que aún me sigue enseñando. Y como decimos nosotros: “Si lo dice Xema, tiene que ser cierto”.

Estos años de doctorado hubieran sido muy aburridos sino hubiera sido por la grata compañía de los miembros de NePhoS. Antiguos, coetáneos y recientes miembros que han hecho estos años mucho más llevaderos tanto en la hora del café, como en congresos, como en el tiempo libre. Procuraré nombrarlos a todos, pero pido disculpas por adelantado ya que es probable que me deje a alguien. Gracias a Joaquín, Raquel, Abel, María Méndez, Mahbubur, Víctor, María Alba, Gerard, Peilin, Pilar, Agata, Maggy, Laura, María Porta, José, Agustín, Elisabet, Elisabetta y, por si acaso, etc.

También quisiera agradecer a los miembros del grupo MaCEPV del Laboratory ICube de la Universidad de Estrasburgo su cálida acogida durante mi estancia de movilidad en Francia. Realmente me sentí como en casa a pesar de la distancia. Agradecimientos a Anne-Sophie Cordan, Yann Leroy, Adam Raba, Rixatdil Dilmurat (au revoir) y Damir Aidarkhanov.

Por supuesto también agradecer a los nuevos miembros de mi familia, que empezaron a formar parte de ella al poco de empezar el doctorado, su apoyo. Todo por culpa de Antonio, mi hermano. Dicen que el mejor regalo que te puede hacer un hermano es un sobrino, pues él me trajo tres casi de golpe. De diferentes edades, para que no me aburriera. Mi más sincero agradecimiento a Lidia, Xavi, Vero y Sergio, y el pequeño Alex (nene). Por los buenos momentos pasados que me hacían olvidar el estrés del día a día. Por acordarse de mí en mi exilio francés. Por recibirme con una pancarta como si fuera un famoso. Por todas esas comidas (pizzas). Porque después

de tanto tiempo por fin pude verte marcar un gol. Podría escribir otra tesis solamente de agradecimientos hacia vosotros. Disculpas por teneros un poco abandonados últimamente.

A mis padres, por su apoyo incondicional todos estos años. Mi más sincero apoyo de vuelta en estos difíciles momentos que les ha tocado vivir ahora.

Por último también agradecer el apoyo económico en forma de beca por parte del extinto Ministerio de Ciencia e Innovación.

UNIVERSITAT ROVIRA I VIRGILI
DESIGN AND MODELLING OF INTERDIGITATED AND NANOSTRUCTURED POLYMER SOLAR CELLS
Pedro Granero Secilla
Dipòsit Legal: T 891-2015

List of Figures

UNIVERSITAT ROVIRA I VIRGILI
DESIGN AND MODELLING OF INTERDIGITATED AND NANOSTRUCTURED POLYMER SOLAR CELLS
Pedro Granero Secilla
Dipòsit Legal: T 891-2015

List of Tables

UNIVERSITAT ROVIRA I VIRGILI
DESIGN AND MODELLING OF INTERDIGITATED AND NANOSTRUCTURED POLYMER SOLAR CELLS
Pedro Granero Secilla
Dipòsit Legal: T 891-2015

List of Contributions

Journal Articles

P. Granero, V.S. Balderrama, J. Ferré-Borrull, J. Pallarès, and L.F. Marsal, "Two-dimensional finite-element modeling of periodical interdigitated full organic solar cells", *J. Appl. Phys.* **113** 043107, (2013).

P. Granero, V.S. Balderrama, J. Ferré-Borrull, J. Pallarès, L.F. Marsal, "Light absorption modeling of ordered bulk heterojunction organic solar cells", *Curr. Appl. Phys.* **13** 1801-1807, (2013).

M. Alba, N. Pazos-Perez, B. Vaz, P. Formentin, M. Tebbe, M.A. Correa-Duarte, P. Granero, J. Ferré-Borrull, R. Alvarez, J. Pallarès, A. Fery, A.R. de Lera, L.F. Marsal, and R.A. Alvarez-Puebla, "Macroscale plasmonic substrates for highly sensitive surface-enhanced Raman scattering", *Angew. Chem. Int. Ed.* **52** 6459-6463, (2013).

V.S. Balderrama, M. Estrada, P.L. Han, P. Granero, J. Pallarés, J. Ferré-Borrull, and L.F. Marsal, "Degradation of electrical properties of PTB1:PCBM solar cells under different environments", *Sol. Energ. Mat. Sol. C.* **125** 155-163, (2014).

V.S. Balderrama, J. Albero, P. Granero, J. Ferré-Borrull, J. Pallarès, E. Palomares, and L.F. Marsal, "Design, fabrication and charge recombination analysis of interdigitated heterojunction nanomorphology on P3HT/$PC_{70}BM$ solar cells", *Nanoscale*, (2015) (Submitted).

Communications to Conferences

P. Granero, J. Ferré-Borrull, J. Pallarès, and L.F. Marsal, "2D-FDTD analysis of light propagation in nanostructured organic solar cells", *8ª Conferencia de Dispositivos Electrónicos (CDE)*, Palma de Mallorca (Spain), FEBRUARY/02/2011, Poster

P. Granero, J. Ferré-Borrull, J. Pallarès, and L.F. Marsal, "2D finite-element analysis of light absorption in ordered bulk heterojunction organic solar cells", *8th International Caribbean Conference on Devices, Circuits and Systems (ICCDCS)*, Playa del Carmen (Mexico), MARCH/2012, Oral presentation

P. Granero, V.S. Balderrama, J. Ferré-Borrull, J. Pallarès, and L.F. Marsal, "2D finite-element modeling of periodical interdigitated full organic solar cells", *E-MRS 2012 SPRING MEETING*, Strasbourg (France), MAY/2012, Poster

P. Granero, V.S. Balderrama, J. Ferré-Borrull, J. Pallarès, and L.F. Marsal, "Optimal design modelling of interdigitated full organic solar cells", *8th International Conference on Organic Electronics (ICOE)*, Tarragona (Spain), JUNE/2012, Poster

J. Ferré-Borrull, M.M. Rahman, P. Granero, P. Formentín, J. Pallarès, and L.F. Marsal, "Photonic properties and applications of nanoporous anodic alumina", *Fifth International Conference on Optical, Optoelectronic and Photonic Materials and Applications (ICOOPMA12)*, Nara (Japan), JUNE/2012, Oral presentation

P. Granero, V.S. Balderrama, J. Ferré-Borrull, J. Pallarès, and L.F. Marsal, "2D and 3D light absorption modeling of interdigitated full organic solar cells", *Conferencia Española de Nanofotonica 2012 (CEN2012)*, Carmona (Spain), OCTOBER/2012, Poster

P. Granero, V.S. Balderrama, J. Ferré-Borrull, J. Pallarès, and L.F. Marsal, "Finite-element modeling of interdigitated heterojunction organic photovoltaic devices, *8ª Conferencia de Dispositivos Electrónicos (CDE)*, Valladolid (Spain), FEBRUARY/2013, Poster

P. Granero, V.S. Balderrama, J. Ferré-Borrull, J. Pallarès, and L.F. Marsal, "Optical and electrical modeling of interdigitated organic solar cells", *9th International Conference on Organic Electronics (ICOE)*, Grenoble (France), JUNE/2013, Oral presentation

V.S. Balderrama, P. Granero, P.L. Han, J. Ferré-Borrull, J. Pallarès, and L.F. Marsal, "Fabrication, characterization and design modeling of well-ordered interdigitated organic solar cells", *28th European PV Solar Energy Conference and Exhibition (EU PVSEC 2013)*, París (France), SEPTEMBER/2013, Poster

V.S. Balderrama, M. Estrada, P.L. Han, P. Granero, J. Pallarés, J. Ferré-Borrull, and L.F. Marsal, "Stability analysis of organic solar cells fabricated with PTB1:PCBM in accordance with established ISOS-D1 protocols", *Conferencia Española de Nanofotonica 2014 (CEN2014)*, Santander (Spain), MAY/2014; Poster and Oral presentation

J. Ferré-Borrull, V. S. Balderrama, P. Granero, P.L. Han, A. Mihi, J. Pallarès, and L.F. Marsal, "Fabrication, modeling and degradation studies of ordered bulk heterojunction organic solar cells with nanostructured interfaces", *Congreso Internacional de Metalurgia y Materiales SAM-CONAMET / IBEROMAT 2014*, Santa Fe (Argentina), 10/ 2014, Oral presentation - Conference - Symposium

UNIVERSITAT ROVIRA I VIRGILI
DESIGN AND MODELLING OF INTERDIGITATED AND NANOSTRUCTURED POLYMER SOLAR CELLS
Pedro Granero Secilla
Dipòsit Legal: T 891-2015

UNIVERSITAT ROVIRA I VIRGILI
DESIGN AND MODELLING OF INTERDIGITATED AND NANOSTRUCTURED POLYMER SOLAR CELLS
Pedro Granero Secilla
Dipòsit Legal: T 891-2015

"Aprende a aprender."

Xavi Fuertes

"Any sufficiently advanced technology

is indistinguishable from magic."

Sir Arthur C. Clarke

UNIVERSITAT ROVIRA I VIRGILI
DESIGN AND MODELLING OF INTERDIGITATED AND NANOSTRUCTURED POLYMER SOLAR CELLS
Pedro Granero Secilla
Dipòsit Legal: T 891-2015

Take two of them

UNIVERSITAT ROVIRA I VIRGILI
DESIGN AND MODELLING OF INTERDIGITATED AND NANOSTRUCTURED POLYMER SOLAR CELLS
Pedro Granero Secilla
Dipòsit Legal: T 891-2015

CONTENTS

UNIVERSITAT ROVIRA I VIRGILI
DESIGN AND MODELLING OF INTERDIGITATED AND NANOSTRUCTURED POLYMER SOLAR CELLS
Pedro Granero Secilla
Dipòsit Legal: T 891-2015

CHAPTER 1

INTRODUCTION

The constant technology development has brought us amenities that have increased our quality of life to standards unthinkable only few generations ago, and this increase seems to be continued in the future. Obviously, this fact is associated to an increase of resources consumption, such as raw materials and electricity. Nowadays, the rise in electrical consumption can be supplied by the current energy sources. However this will mean an increase of pollution, causing many problems around the world, since nowadays most of the energy that we use comes from non-renewable sources.

Among others, photovoltaics have the potential to become a big part of the solution to this problem. In past decades, solar cells have started to be introduced gradually into the wide group of energy sources. We have now from big power plants that can supply thousands of homes to small devices for little toys. However photovoltaics still represents a small percentage of the total amount of generated electrical energy, even if we only consider the renewable energy sources. This even happens in countries with a high solar irradiation such as Spain, as it is shown in Figure 1.1 [Red Eléctrica de España-2013]. One of the main problems is that photovoltaics technology is still not profitable compared with the rest of energy sources. Solar grade silicon and other materials that are constituents of solar cells are expensive. Also these devices have many limitations of where they can be placed, since for big powers we need big rigid structures.

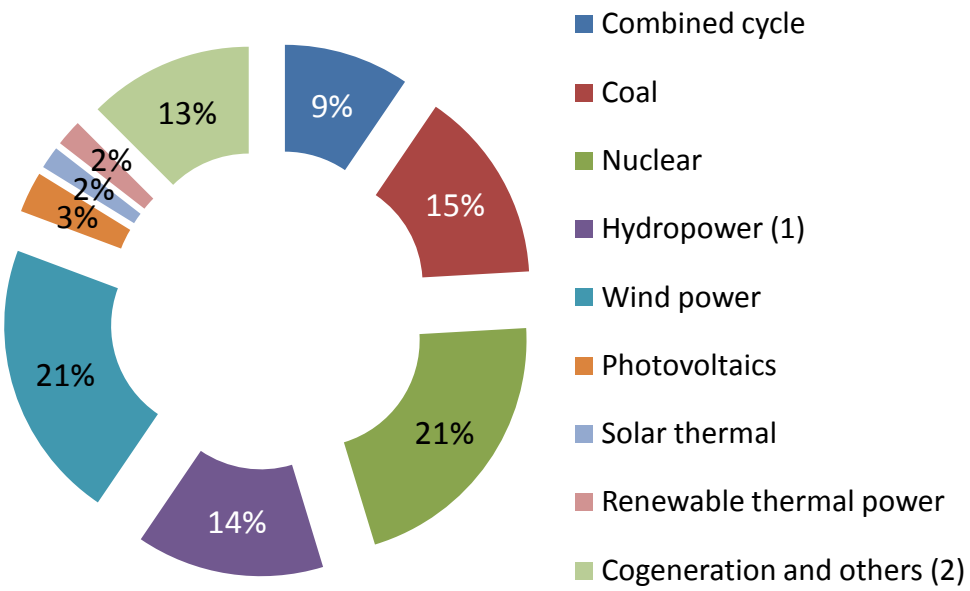

Figure 1.1 *Electric energy sources in Spain (mainland) in 2013 [Red Eléctrica de España-2013]. (1) Pumped-storage non-included, (2) Non-renewable thermal power and fuel/gas included.*

UNIVERSITAT ROVIRA I VIRGILI
DESIGN AND MODELLING OF INTERDIGITATED AND NANOSTRUCTURED POLYMER SOLAR CELLS
Pedro Granero Secilla
Dipòsit Legal: T 891-2015

One promising solution can be organic solar cells (OSC), developed in recent years. The interest of this kind of solar cells lies in the unique properties of the materials that conform them: the organic semiconductors. In contrast to the inorganic semiconductors, like silicon, the organic ones need much less thickness to absorb the maximum sunlight. This fact causes that the resulting devices can be flexible, as they can be very thin, and much cheaper, since although organic semiconductors are expensive they are used in small quantities. Furthermore, with a spread of the technology, a decrease in mass production cost of the organic substances can be expected. The organic semiconductor properties allow OSC to be used in many situations where inorganic cell cannot, such as in complex surfaces (more flexible), as windows coating (thinner so partially transparent) or on indoor applications (higher efficiencies for low light intensities). These facts give OSC the possibility to fill a niche where inorganic solar cells are weak, avoiding to compete with such a mature technology. However, this technology stills needs to be developed.

Organic solar cells differ from inorganic ones in the photovoltaic conversion process. For the inorganic case, when photons are absorbed the material is able to generate electron-hole pairs that become free charges directly at room temperature. But for the organic case these electron-hole pairs remain in an intermediate state called exciton that needs to be dissociated to obtain the free charges. Excitons move by diffusion and to dissociated they need to reach the exciton dissociation interface, which corresponds to the union of the different organic semiconductors that conforms the cell (Donor–Acceptor, D–A, interface). Unfortunately, the exciton diffusion length of the organic materials is very short, been only of few nm. So, only those excitons generated close to the D–A interface will contribute to the photogenerated current. This fact is a very big restriction in OSC efficiency. One solution has been to mix the different organics materials in an interpenetrating blend. So anywhere an exciton is created will be close enough to the dissociation interface.

UNIVERSITAT ROVIRA I VIRGILI
DESIGN AND MODELLING OF INTERDIGITATED AND NANOSTRUCTURED POLYMER SOLAR CELLS
Pedro Granero Secilla
Dipòsit Legal: T 891-2015

However, as a blend it is always complex to control, other solutions have been developed. In this thesis we focus on the interdigitated approach.

In the interdigitated approach, the different organic semiconductors are joined in a complex structure, where one of the materials forms pillars and the other fills the interpillar space. To avoid exciton dissociation losses, the junction between them should be in the scale of the exciton diffusion length. A method to fabricate this kind of structures has been developed in our facilities in the Nano-Electronic and Photonic Systems (NePhoS) group of the Universitat Rovira i Virgili [Santos-2010; Balderrama-2014]. By using the template-assisted synthesis method with nanoporous anodic alumina templates, nanopillars with a hexagonal lattice distribution have been manufactured. However, such small sizes are complex to work with and require long times to be manufactured. So a way of reducing times is crucial to help to develop and to optimize this kind of OSC.

In many fields, numerical simulation models have helped to develop many technologies and understand their mechanisms. They are able to predict results without the need to fabricate real devices. This fact allows reducing development times, since simulations are usually faster than a device fabrication, and costs, since we can reduce material waste by avoiding the fabrication of non-optimal devices. Since many years ago, several accurate models exist for the case of inorganic cells, however the behaviour of OSC is still not perfectly known. Additionally, it is difficult to know a priori if the existing models for OSC will be suitable and accurate enough for the small geometries of the interdigitated organic devices. So, there is still work to do to obtain a precise numerical simulation model for OSC.

UNIVERSITAT ROVIRA I VIRGILI
DESIGN AND MODELLING OF INTERDIGITATED AND NANOSTRUCTURED POLYMER SOLAR CELLS
Pedro Granero Secilla
Dipòsit Legal: T 891-2015

The main objectives of this thesis are:

- Develop a complete model to simulate the different steps of the photovoltaic conversion process in interdigitated organic solar cells. This model will be based on the finite element method, which can give us information of every magnitude as a function of the position. Most of the existing models consider the active region of the devices as a uniform material from the point of view of light interaction. This simplification is not important when we have an interpenetrating blend, but it may affect the final results in the case of interdigitated cells
- Show that this model can be used to make a systematic study of interdigitated OSC that will help to predict which geometrical characteristic will be better to optimize this kind of devices and how to increase their efficiency
- Validate the model with experimental results of real devices obtained in our facilities and, if necessary, improve, adjust or correct the model
- Demonstrate that the developed method can simulate correctly different devices and structures, by making some adaptations, and not only interdigitated full organic solar cells

To achieve these objectives, this thesis is organized as follows:

In Chapter 2 we introduce the basic concepts of organic photovoltaics. From the organic semiconductors properties, which work in a different way than the inorganic ones, to the photovoltaic conversion process in OSC. The different types of organic semiconductors (electron donors and electron acceptor) are introduced, with also the concept of exciton and what this state represents to the photovoltaic conversion process. Then, a detailed description of the different architectures that exist for OSC

UNIVERSITAT ROVIRA I VIRGILI
DESIGN AND MODELLING OF INTERDIGITATED AND NANOSTRUCTURED POLYMER SOLAR CELLS
Pedro Granero Secilla
Dipòsit Legal: T 891-2015

and their evolution since the first organic semiconductors where discovered is given. Finally, a state of the art of the existing simulation models completes this chapter.

Chapter 3 is focused on the numerical method developed in this work. By using the finite element method (FEM), we introduce a model where the different magnitudes related to the photovoltaic conversion process can be calculated as a function of the position. The complete Maxwell equations, the *exciton diffusion equation* and the drift-diffusion model are solved within the same numerical framework. The model can be divided into two main parts: the optical and the electrical behaviour. The results of each step of the photovoltaic conversion process are used as an input of the subsequent step, in all cases as function of the position.

In Chapter 4, we present the results of this numerical simulation method applied to the interdigitated OSC. By varying the devices geometry of the dissociation interface in a wide range of values, we present a systematic study. Several conclusions can be extracted from the results that can be used as an optimization guide to help to improve experimental devices obtained in our facilities and to increase its efficiency reducing times and costs. After this study, a validation of the simulation method with experimental results, manufactured in our facilities, is presented. By using the template-assisted synthesis method with nanoporous anodic alumina templates (NAAT) we have obtained functional devices that can be compared with our models. This devices have the structure of ITO/PEDOT:PSS/P3HT/PCBM/Ag. Some parameter adjustments are also presented to totally fit the model to the real devices.

Chapter 5 is devoted to the application of the improved numerical simulation procedure to organic solar cells with the same structure but with different nanostructured D–A junctions. By varying the D–A interface geometry, we have modelled planar bilayer, nanopillars, nanowells and nanopyramids D–A junctions. The

UNIVERSITAT ROVIRA I VIRGILI
DESIGN AND MODELLING OF INTERDIGITATED AND NANOSTRUCTURED POLYMER SOLAR CELLS
Pedro Granero Secilla
Dipòsit Legal: T 891-2015

purpose of this chapter is to compare these kinds of nanostructured junctions in OSC for the two existing configurations, the conventional and the inverted one. An optical and an exciton diffusion study are carried out to check which configuration is better in terms of efficiency for each case. In this study, the exciton diffusion length is used as a parameter since it can vary due to the nanoconfinement of polymer chains.

Chapter 6 discusses about the application and adaptation of the simulation method to other devices and structures to demonstrate and to show that it can work correctly not only for the full organic solar cells that we have previously seen. The simulation model is applied to two situations: hybrid solar cells and gold nanospheres pyramids. For case of the hybrid solar cell, we have that the active region is a blend of the different organic semiconductors and has a nanostructured TiO_2 electrode. Several modifications of the method presented in Chapter 3 are explained here to adapt the model to this different technology. Simulation results are also compared with experimental data provided from the group of Dr. Monica Lira-Cantu (from the Laboratory of Nanostructured Materials for Photovoltaic Energy, CIN2, Barcelona). After this comparison, a final parameter fit completes this adapted simulation model. Regarding the gold nanospheres pyramids, a work about the simulation of the plasmonic effect in gold nanospheres pyramids is shown. This kind of structures is intended to provide cheap ultrasensitive and ultrafast sensors with surface-enhanced Raman scattering (SERS) spectroscopy as the transducer, in our case, to develop a handheld reversible SERS sensor for the live monitoring of carbon monoxide in the atmosphere. The aim of this chapter is to demonstrate that the optical part of the simulation procedure can be used to model different effects in geometries in the range of the nm so it is not only restricted to solar cells.

Finally, Chapter 7 completes the thesis with the summary of what we have seen, the final conclusions and some tips for possible related future work.

UNIVERSITAT ROVIRA I VIRGILI
DESIGN AND MODELLING OF INTERDIGITATED AND NANOSTRUCTURED POLYMER SOLAR CELLS
Pedro Granero Secilla
Dipòsit Legal: T 891-2015

UNIVERSITAT ROVIRA I VIRGILI
DESIGN AND MODELLING OF INTERDIGITATED AND NANOSTRUCTURED POLYMER SOLAR CELLS
Pedro Granero Secilla
Dipòsit Legal: T 891-2015

CHAPTER 2

FUNDAMENTALS OF ORGANIC PHOTOVOLTAICS

In this chapter we introduce the basic concepts of organic photovoltaics. The interest of organic solar cells (OSC) lies in the unique properties of the materials that conform them: the organic semiconductors. In contrast to the inorganic semiconductors, like silicon, the organic ones need much less thickness to absorb the maximum sunlight [Würfel-2009]. This fact causes that the resulting devices can be flexible, as they can be very thin, and much cheaper, since although organic semiconductors are expensive they are used in small quantities. OSC also differ from inorganic ones in the photovoltaic conversion process. For the inorganic case, when photons are absorbed,

UNIVERSITAT ROVIRA I VIRGILI
DESIGN AND MODELLING OF INTERDIGITATED AND NANOSTRUCTURED POLYMER SOLAR CELLS
Pedro Granero Secilla
Dipòsit Legal: T 891-2015

the material is able to generate electron-hole pairs that become free charges directly at room temperature. But for the organic case these electron-hole pairs remain in an intermediate state called exciton that needs to be dissociated to obtain the free charges. These properties and characteristics come from the physical and chemical characteristics of the organic semiconductors, that will be explained in this chapter. Then, a detailed description of the different architectures that exist for OSC and their evolution since the first organic semiconductors where discovered is given. Finally, a state of the art of the existing simulation models completes this chapter.

2.1.- ORGANIC SEMICONDUCTORS

2.1.1.- FUNDAMENTALS OF ORGANIC SEMICONDUCTORS

The main difference between the organic solar cells and the inorganic ones is the material used for the active region. Instead of using inorganic semiconductors as constituents, such as silicon, cadmium telluride, gallium arsenide (GaAs), or copper indium gallium selenide (CIGS) for instance, OSC are made of organic materials. This kind of semiconductors has several differences if compared with the inorganic ones. However, we can find some analogies too. In organic photovoltaics an equivalent nomenclature to the inorganic is used. Instead of the *conduction band* the equivalent concept is the LUMO level (*Lowest Unoccupied Molecular Orbital*), and instead of *valence band* there is the HOMO level (*Highest Occupied Molecular Orbital*). The energy difference between these two parameters is the band gap of the material.

Organic semiconductor properties come from the atypical carbon atom properties. Among other configurations, the carbon atom can form the sp_2 hybridization. Here, the sp_2 orbitals form a triangle in a plane while the p_z orbitals are perpendicular to

such plane. Then, with the superposition of two sp_2 orbitals in two neighbouring carbon atoms, a bond σ can be formed as it can be seen in Figure 2.1A. The energy difference between the *bonding orbitals* (σ− or σ in Figures 2.1B and 2.2 respectively) and the *antibonding orbitals* (σ+ or σ* in Figures 2.1B and 2.2 respectively) is quite high, being much beyond the visible spectrum range. Consequently, longer bonded carbon atom chains will form a material with a high bandgap, so this material will have the characteristic isolator behaviour of organic materials.

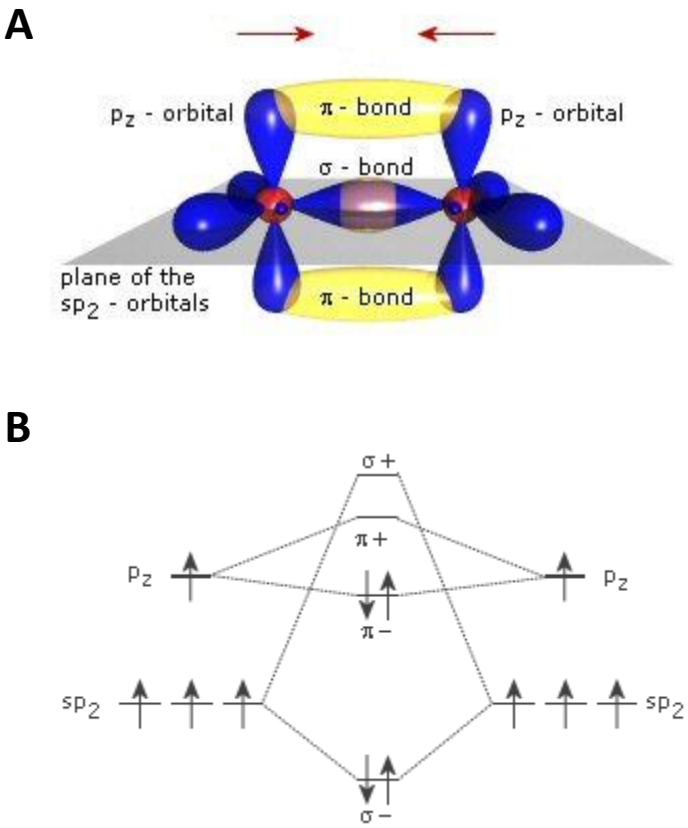

Figure 2.1 *Orbital and bonds scheme (A), and energy levels for the different bounds (B) for two carbon atoms in sp_2 hybridization.*

UNIVERSITAT ROVIRA I VIRGILI
DESIGN AND MODELLING OF INTERDIGITATED AND NANOSTRUCTURED POLYMER SOLAR CELLS
Pedro Granero Secilla
Dipòsit Legal: T 891-2015

However, in the sp_2 hybridization, the p_z orbitals also form additional bonds of π type. These bonds have a much lower energy difference between the HOMO and the LUMO levels, as it can be seen in Figures 2.1B and 2.2 (π– - π+, π - π* respectively). So, the weaker excitations of the conjugated molecules will be the π - π* transitions, with a typical energy between 1.5 and 3 eV [Brütting-2005]. This allows the organic materials to have a high light absorption or emission in the visible spectrum range, or close to it, and to show semiconductor properties.

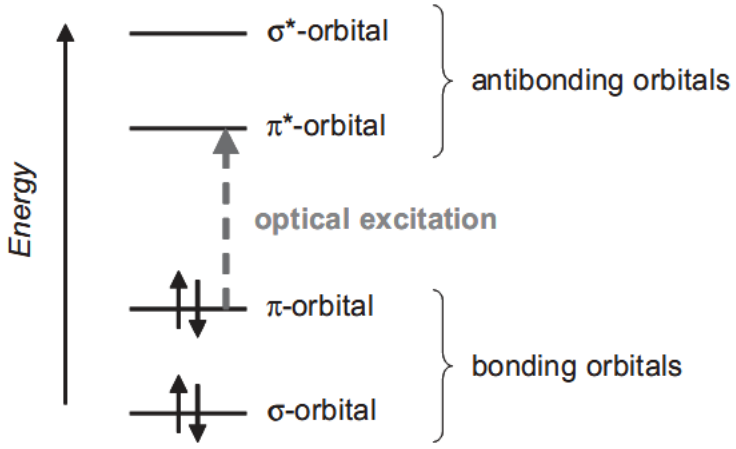

Figure 2.2 *Simplified scheme of the energy levels for the different orbitals in two bonded carbon atoms in sp_2 hybridization.*

UNIVERSITAT ROVIRA I VIRGILI
DESIGN AND MODELLING OF INTERDIGITATED AND NANOSTRUCTURED POLYMER SOLAR CELLS
Pedro Granero Secilla
Dipòsit Legal: T 891-2015

2.1.2.- TYPES OF ORGANIC SEMICONDUCTORS

There exist two main categories of organic semiconductors:

- **Conjugated polymers**: macromolecules formed by the union of repetitive structural units.
  Deposition techniques from a solution: spin-coating or imprinting

- **Small molecule**: low molecular weight.
  Deposition techniques from gas: sublimation or evaporation

The optical and the electrical properties of these two types of organic semiconductors are very similar, being the deposition technique to obtain thin layers the main difference between them.

Unlike inorganic semiconductors, the organic ones do not need to be doped since its nature depends on the electronegativity of the material. So, organic semiconductors can be *electron donors*, if they show a low electronegativity, or *electron acceptors***,** when they have a high electronegativity.

Following the analogy with the inorganic semiconductors, we have that the organic semiconductors of electron donor type act and have the characteristics and the behaviour of the inorganic p-type. This is because they have a higher hole mobility than electron mobility. In Figure 2.3 it is shown several electron donor materials used as constituents of OSC.

UNIVERSITAT ROVIRA I VIRGILI
DESIGN AND MODELLING OF INTERDIGITATED AND NANOSTRUCTURED POLYMER SOLAR CELLS
Pedro Granero Secilla
Dipòsit Legal: T 891-2015

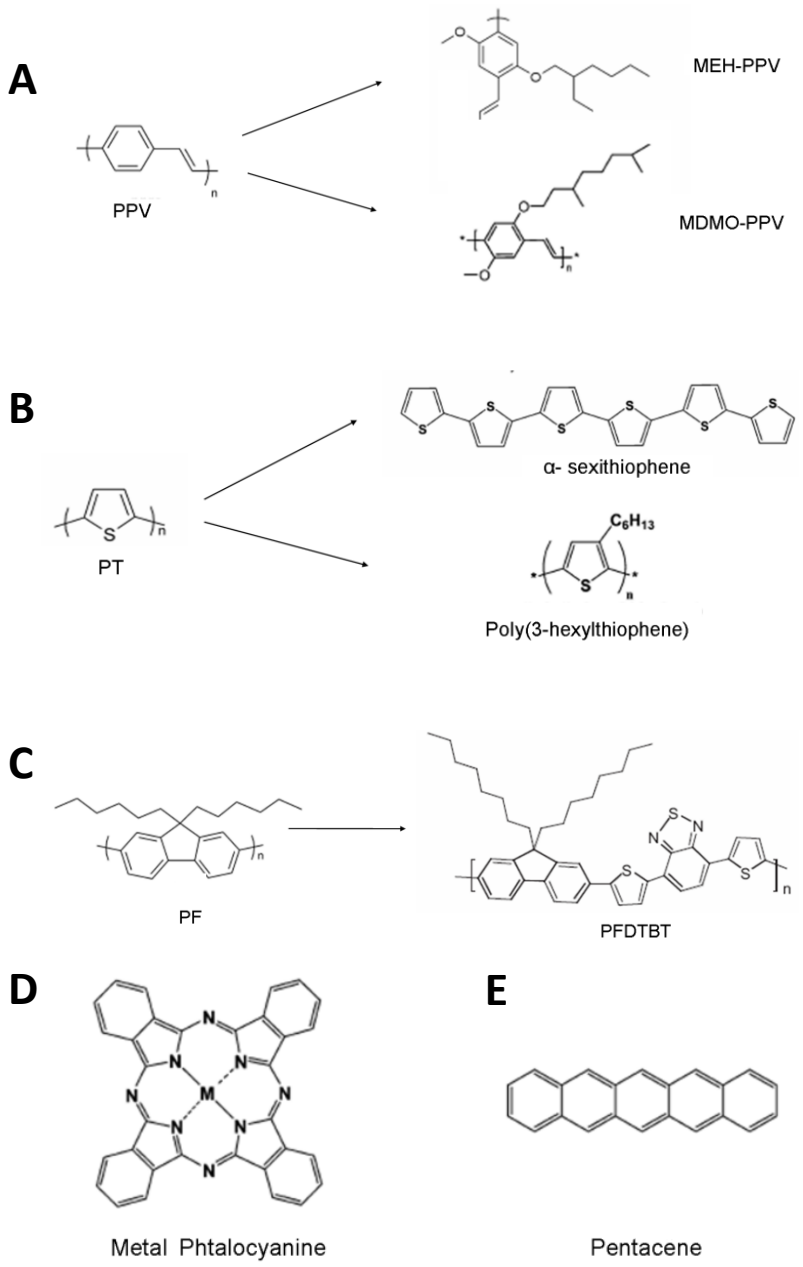

Figure 2.3 *Molecular structure of several electron donor materials used as constituents of OSC. (A), (B) and (C) are conjugated polymers, on the right there are their derivates, and (D) and (E) are small molecule ones.*

UNIVERSITAT ROVIRA I VIRGILI
DESIGN AND MODELLING OF INTERDIGITATED AND NANOSTRUCTURED POLYMER SOLAR CELLS
Pedro Granero Secilla
Dipòsit Legal: T 891-2015

To end with the analogy with the inorganic semiconductors, on the other hand the organic semiconductors of electron acceptor type act and have the characteristics and the behaviour of the inorganic n-type. So, in this case the materials have a higher electron mobility than the hole one. In Figure 2.4 it is shown several electron acceptor materials used as constituents of OSC.

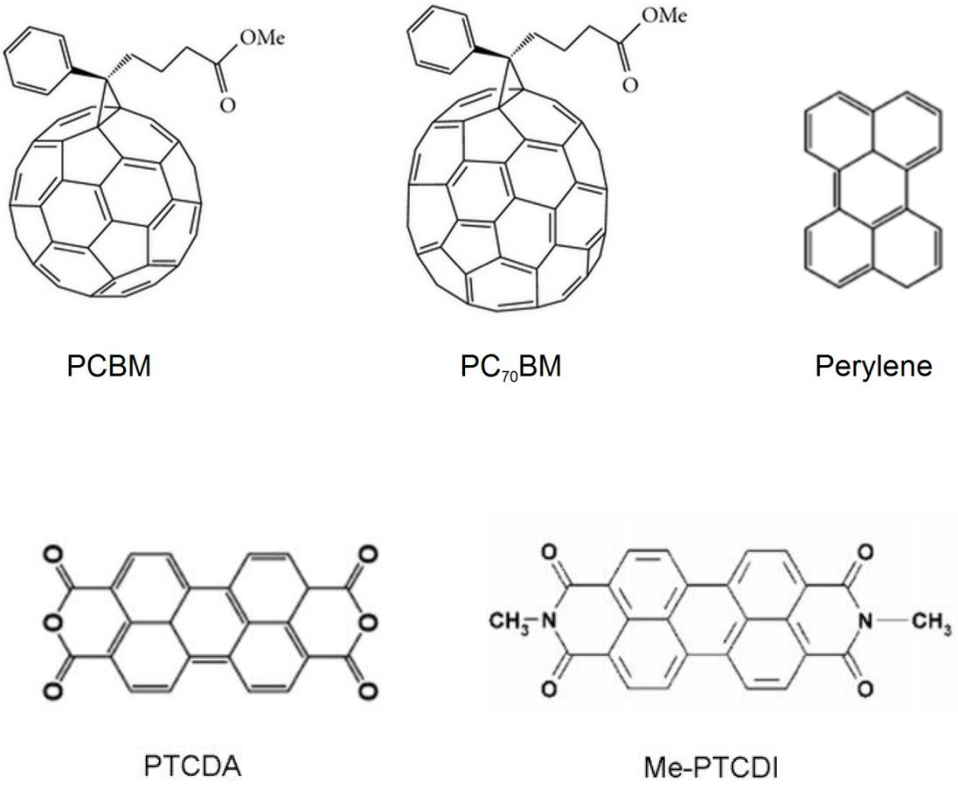

Figure 2.4 *Molecular structure of several electron acceptor materials used as constituents of OSC. All of them are small molecule type.*

2.1.3.- EXCITONS

There is also an important difference between the organic semiconductors and the organic ones regarding the free charge generation. In both cases, for organic and inorganic semiconductors, the absorption of a photon by the material does not cause the generation of free an electron-hole pair directly. This happens because the electron and the hole attract each other due to their opposite charge. This entity, where the electron and the hole are still bounded by Coulomb forces, is called *exciton*. This quasiparticle can travel through the semiconductor and it is electrically neutral.

Since the exciton is very similar to the hydrogen atom, which consists only in a proton (positive charge) and an electron (negative charge), the same model can be used to analyze it. Hence, we can consider the exciton *binding energy* a special case of the one of an electron in the hydrogen atom [Würfel-2009]:

$$\varepsilon_{exc} = \frac{m_{red} \cdot e^4}{2(4\pi\varepsilon\varepsilon_0)^2 \cdot \hbar^2} \tag{2.1}$$

$$m_{red} = \frac{m_e^* \cdot m_h^*}{m_e^* + m_h^*} \tag{2.2}$$

where m_{red} is the exciton reduced mass, ε the relative permittivity of the material, ε_0 the vacuum permittivity, $\hbar = h/(2\pi)$ the reduced Planck constant, m_e^* the electron effective mass and m_h^* the hole effective mass.

This energy is the minimum required to separate the whole in the different parts, in our case to dissociate an exciton into a free hole and an electron. For most of inorganic semiconductors, the binding energy is much smaller than *kT* at room temperature (25.85 meV at 300 K). This is due to the high relative permittivity of the inorganic materials, typically ε over 10 [Würfel-2009], and to a lower electron and hole effective masses than their real ones. As a consequence of this, in the inorganic semiconductors excitons only exist at low temperature due to the thermal dissociation that affects them. At room temperature, the electron and the hole are free just after the exciton generation due to the photon absorption. So, there is no need to make a difference between the minimum energy that a photon needs to generate in the material an electron-hole pair and the minimum energy to dissociate this pair.

This does not happen in organic semiconductors, as they consist of molecules that are weakly bonded to each other by van der Waals forces. As a result, they have a low relative permittivity and a high electron and hole effective masses. From Equation 2.1, it can be deduced that this fact will increase the exciton binding energy. Additionally, this also reduces the exciton radius to values in the range of interatomic distances. For these sizes, Equation 2.1 is not accurate enough and the real binding energies will be even higher that the predicted mathematically. In some cases, these energies can achieve tenths of eV. Such values are much higher than *kT* at room temperature, so there will not be exciton thermal dissociation in the materials. In the next table it is shown some binding energies for organic semiconductors. As it can be seen, all the values are higher than the binding energy for silicon and than *kT* at 300 K.

Material	***Binding energies (eV)***
Si	*0,0147*
Alq_3	*1,40*
CuPc	*0,60*
MEH-PPV	*0,35*
PPV	*0,05−1,10*
PTCDA	*0,80*

Table 2.1 *Silicon and several organic semiconductors binding energies. Data from [Monestier-2008; Knupfer-2003].*

Hence, for the case for organic semiconductors, most of the absorbed photons will result in generated excitons. In contrast, the direct frees charge generation will be extremely low. Consequently, the solar energy conversion process for organic devices will need to include an additional step, which it is not considered for the inorganic cells, in order to ensure exciton dissociation and that will require additional energy.

2.2.- STEPS OF THE SOLAR ENERGY CONVERSION PROCESS

In the previous section we have seen that in the organic semiconductors the pairs electron-hole remain in the bonded form of excitons instead of becoming free charge as it happens for the case of inorganic devices. To separate this union, that is to dissociate the exciton, a system Donor–Acceptor (D–A) is required. In Figure 2.5A it is shown this system. This structure is formed with a layer of an electron donor material and another of electron acceptor material. When an exciton reaches the

UNIVERSITAT ROVIRA I VIRGILI
DESIGN AND MODELLING OF INTERDIGITATED AND NANOSTRUCTURED POLYMER SOLAR CELLS
Pedro Granero Secilla
Dipòsit Legal: T 891-2015

donor/acceptor interface, the electron is transferred to the material with a higher electronegativity, that is the acceptor material, and the hole will be accepted by the semiconductor with the lower electronegativity, in this case the donor material.

The complete solar energy conversion process, which starts with the photon absorption by the material and ends with the extraction of free charges trough the electrodes, is depicted in Figure 2.5:

- First, a photon is absorbed by the electron donor material (Figure 2.5B), this causes the generation of an exciton.

- This exciton diffuses trough the material and eventually reaches the D–A interface (Figure 2.5C).

- There, the electron will be transferred to the acceptor material and the hole will remain in the donor one (Figure 2.5D). In this moment, even being its components in different materials, the exciton is still bonded and it will be necessary to be dissociated into free charges.

- After that process, electrons and holes will be transported through the corresponding semiconductor until they reach the electrodes (Figure 2.5E).

- Finally, there the free charges will be collected and extracted to an external circuit (Figure 2.5F).

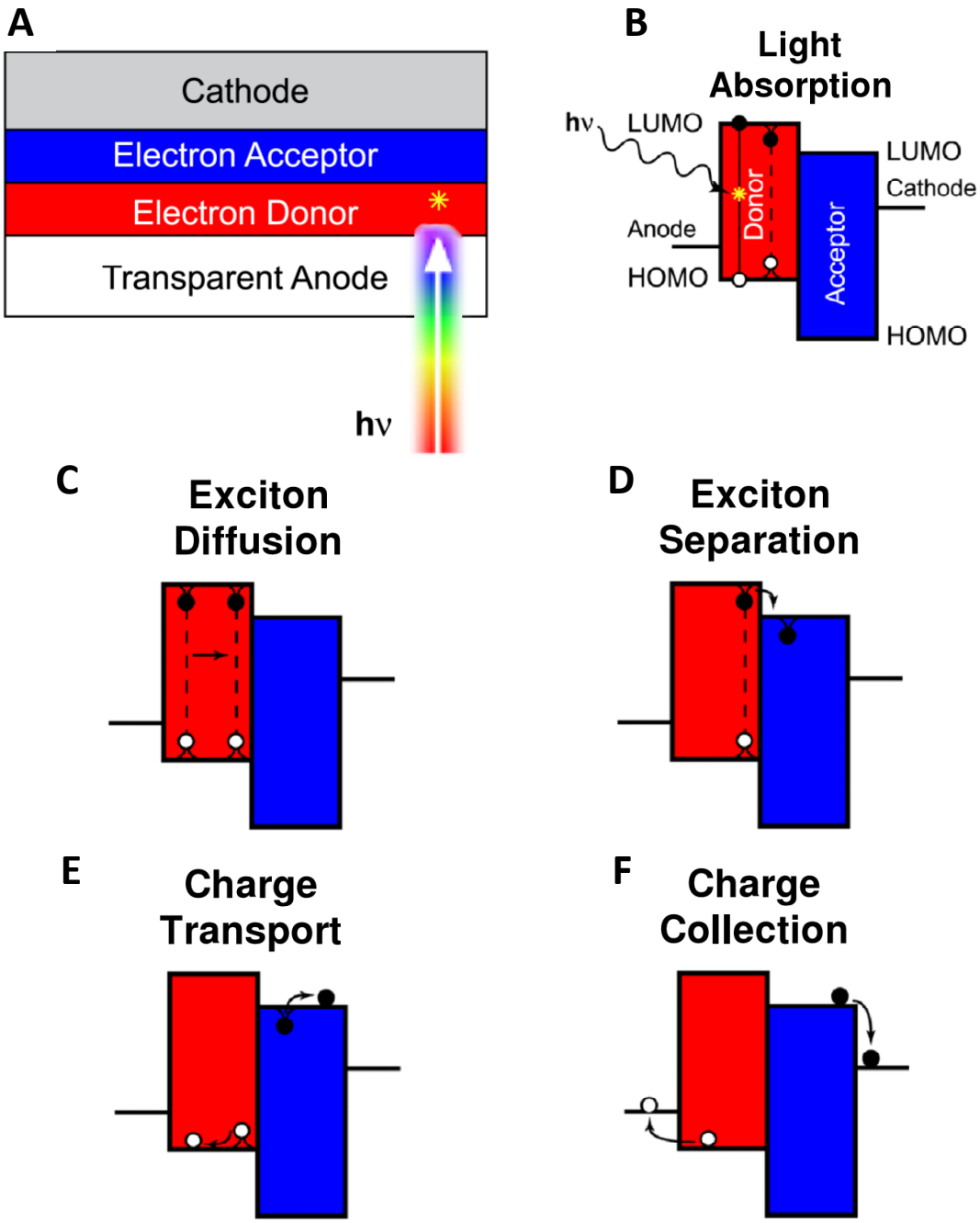

Figure 2.5 *Scheme of a D–A system (A) and the steps of the solar energy conversion process in OSC (B-F). White dots stand for holes and black dots stands for electrons.*

2.3.- OTHER FACTORS INFLUENCING THE ENERGY CONVERSION PROCESS

The energy conversion process can present several losses in every step that will reduce the overall efficiency of an organic solar cell. These losses are caused by the limitations of the organic semiconductors. Figure 2.6 displays some of the most common losses mechanisms. The first issue is that the active layer will not absorb all the incident photons (Figure 2.6-1). Organic materials do not absorb the entire solar spectrum due to their high bandgap. Once created, excitons can decay if they do not reach the dissociation interface quickly, i.e., the Donor–Acceptor interface (Figure 2.6-2). Due to the short exciton diffusion lengths in organic semiconductors, this loss mechanism is a big issue for organic photovoltaics and it is a key limitation. The germinate recombination (Figure 2.6-3) is related to the amount of free charge carriers that recombine after the electron transference but before the exciton dissociation. Finally, a portion of the free charges will recombine during their path to the electrodes (Figure 2.6-4). It is the so-called bimolecular recombination.

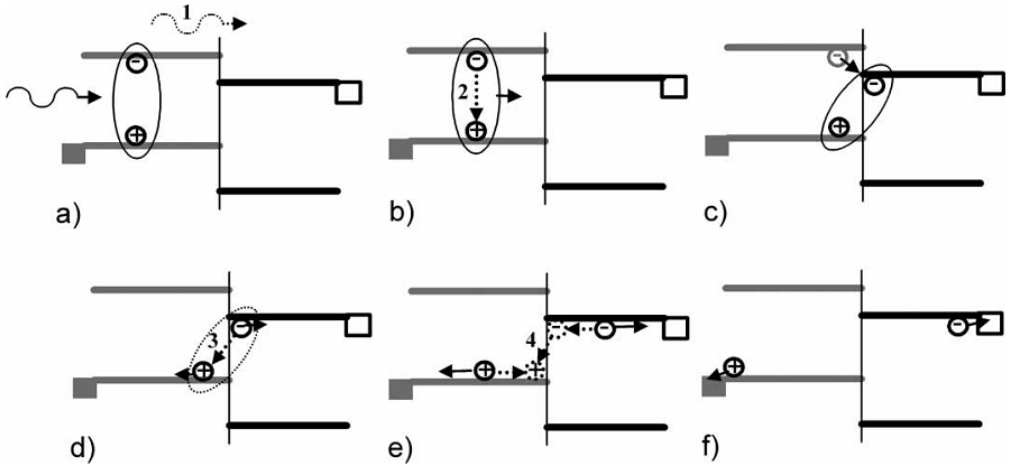

Figure 2.6 *Scheme of the steps of the solar energy conversion process showing several loss mechanisms. Non-absorbed photons (1), exciton decay (2), germinate recombination (3), and bimolecular recombination (4).*

UNIVERSITAT ROVIRA I VIRGILI
DESIGN AND MODELLING OF INTERDIGITATED AND NANOSTRUCTURED POLYMER SOLAR CELLS
Pedro Granero Secilla
Dipòsit Legal: T 891-2015

2.4.- REVIEW OF ORGANIC SOLAR CELLS ARCHITECTURE EVOLUTION

Since its invention, organic materials have always been considered as insulators. The first use of this kind of materials in solar cells appeared in the 1950's, however they only were used due to their photoconductive properties (organic dyes) [Spanggaard-2004]. It was not until the 70's that chemists started to investigate the possibility of controlling the mechanical, optical and electrical properties of the organic materials by modifying their chemical structure. With the discovery of the first conductive inorganic polymer, the sulfur polynitride (with a conductivity of 10^3 S/cm), this research was intensified [MacDiarmid-1976; Monestier-2008].

In 1977, Heeger, MacDiarmid and Shirakawa demonstrate that polyacetylene $(C_2H_2)_n$ can be doped to form a new class of conducting polymers in which the electrical conductivity can be systematically varied in a range of eleven orders of magnitude. So it was able to change its behaviour from an isolator to a conductive material with tunable conductivity properties in between, that means passing through the semiconductor regime [Chiang-1977]. Their experiments showed this huge increase in electrical conductivity of the polyacetylene when doped with controlled amounts of the halogens chlorine, bomine, or iodine, and with arsenic pentafluoride (AsF_5).

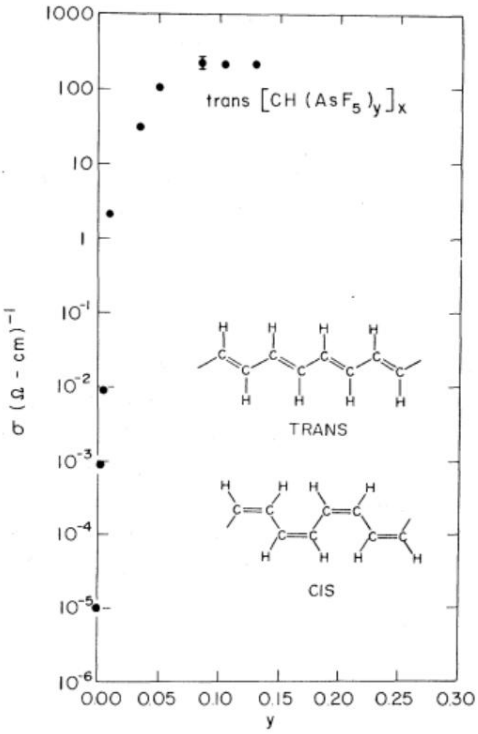

Figure 2.7 *Electrical conductivity of trans-$(CH)_x$ as a function of AsF_5 dopant concentration. Reproduced from [Chiang-1977].*

The discovery and development of the conductive polymers was laureate with the Nobel Prize on Chemistry in 2000 [Nobel Foundation-2000]. With this event a new field in research was opened that was able to bring us materials with the optoelectronic and semiconductor properties of the inorganic materials and the advantages of organic materials such as transparency, flexibility and cost. These new materials would be applied to solar cells.

2.4.1.- SINGLE LAYER

The first OSC were based on single thermally evaporated molecular organic layers sandwiched between two metal electrodes of different work functions (Figure 2.8). The rectifying behaviour of these devices can be explained by the metal-insulator-metal (MIM) model (for insulators) or by the formation of a Schottky barrier (for doped materials) between the metal with the lower work function and the p-type (electron donor) organic layer [Hoppe-2004].

In Figure 2.8B there is a scheme for the case of a Schottky junction at the aluminium contact. Close to the contact, in the depletion region *W*, the resulting band bending from the Schottky contact is shown. This is due to that the difference between the two work functions of the electrodes generates an electric field in the organic material. This corresponds to an electric field in which excitons can be dissociated. This electric field allow excitons to be dissociated so that the free charges are then pushed to the respective electrodes to be collected.

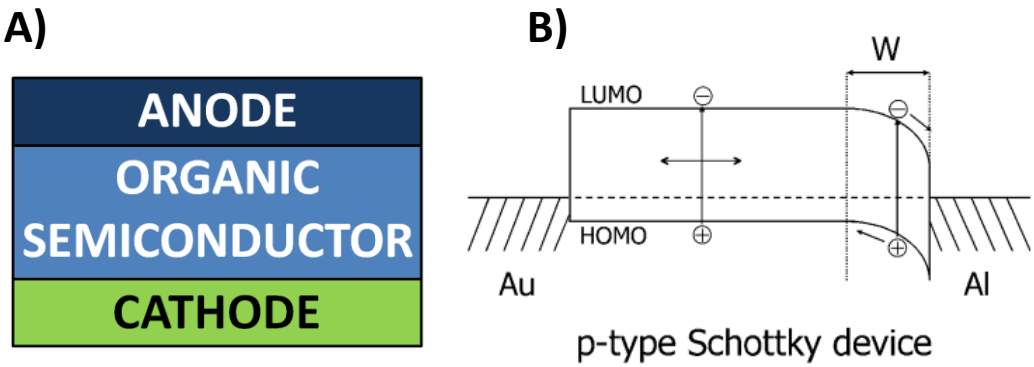

Figure 2.8 *Scheme of a single layer OSC architecture (A) and of the exciton diffusion and dissociation process in a single layer device with a Schottky contact at the aluminium contact (B) [Hoppe-2004].*

UNIVERSITAT ROVIRA I VIRGILI
DESIGN AND MODELLING OF INTERDIGITATED AND NANOSTRUCTURED POLYMER SOLAR CELLS
Pedro Granero Secilla
Dipòsit Legal: T 891-2015

In this architecture, the photogenerated excitons can only be dissociated in the depletion layer *W* localized close to the electrode. This region is very thin so the exciton dissociation efficiency will be very low. Additionally, the generated electric field is very weak, being usually not enough to dissociate all the excitons. Hence this architecture has too many losses to be an efficient method to build a profitable OSC.

Several authors reported results of OSC with this architecture, in all cases with very low efficiency in the solar energy conversion process. P.H. Fang obtained an efficiency in the order of 10^{-5}% in devices where the organic material was tetracene in 1974 [Fang-1974], and Merritt and Hovel reported an efficiency of 0.1% in cells based on hydroxy squarylium in 1976 [Merritt-1976]. However, we had to wait until 1978 to find a remarkable efficiency of 0.7%, with a device manufactured by Ghosh and Feng [Ghosh-1978]. The structure of this OSC consisted of a layer of merocyanine embedded between one electrode of aluminium and another of silver, with a total area of 1cm^2 approximately. This work represented a big increase in the efficiency of OSC. Nevertheless with this kind of devices it was not possible to achieve high efficiencies, so a new architecture needed to be developed.

2.4.2.- PLANAR BILAYER

To solve the problems of the previous architecture and to help to increase the efficiency of OSC, a bilayer structure was developed. In devices with this kind of architecture, organic semiconductors of two different types (electron donor and electron acceptor) are joined together in a planar interface. This junction is embedded between two electrodes with appropriated energy levels to the donor (D) HOMO and the acceptor (A) LUMO levels to ensure an efficient charge extraction (Figure 2.9). The donor contacts the higher work function metal and the acceptor the

lower one to achieve good hole and electron collection, respectively. With this architecture, excitons dissociate in the D–A interface because of the differential of electron affinity of the materials, instead of a built-in electric field in a space-charge region. The solar energy conversion process in this kind of OSC is the one that all the nowadays OSC follows (see section 2.2 for more details).

This architecture was developed for the first time in 1986 by the research group of Dr. Tang, who achieved and efficiency of 1% [Tang-1986]. Their device was based on a planar bilayer structure with two different organic semiconductors, one with a high hole mobility (donor) and the other with a high electron mobility (acceptor). In this case the donor material was copper phthalocyanine (CuPc) and the acceptor material was a perylene tetracarboxylic derivative (PV).

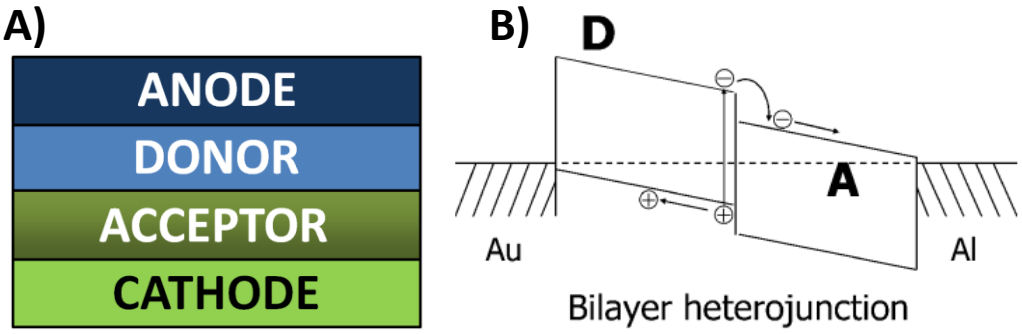

Figure 2.9 *Scheme of a planar bilayer OSC architecture (A) and of the exciton dissociation and charge transport (B) [Hoppe-2004].*

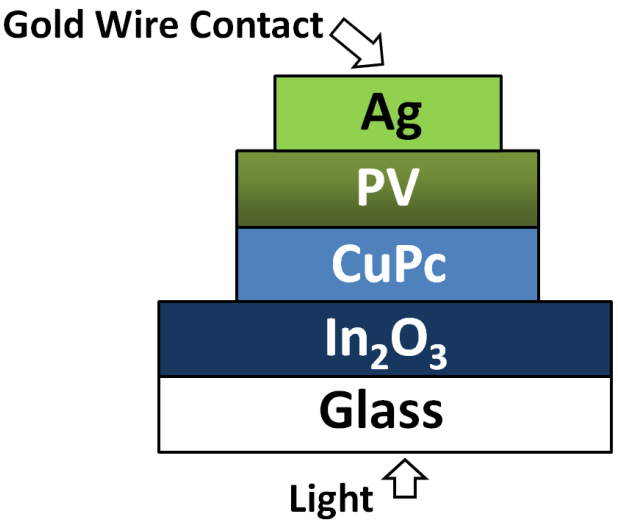

Figure 2.10 *Schematic of Dr. Tang's device, where it can be seen the two organic semiconductor layers of different type [Tang-1986]. It was the first OSC with the planar bilayer typology.*

In the case of the single layer cells, the photovoltaic properties of the devices strongly depend on both electrode characteristics. In contrast, in the planar bilayer architecture these properties depend on the D–A interface. As a result, higher efficiencies could be achieved. One of the characteristic parameters of the solar cells that had a higher improvement was the *Fill Factor* (*FF*), which was very low in single layer OSC. The introduction of this new architecture, with a behaviour totally different from the previous cases and with the most efficient solar energy conversion process until today, can be considered the most important progress in Organic Photovoltaics.

Despite being this structure an important improvement, it had still a very important limitation: the short exciton diffusion length of the organic materials. As seen before, if an exciton is not created close enough to an exciton dissociation interface (the D–A interface), there is a high probability of recombination before it can contribute to the

UNIVERSITAT ROVIRA I VIRGILI
DESIGN AND MODELLING OF INTERDIGITATED AND NANOSTRUCTURED POLYMER SOLAR CELLS
Pedro Granero Secilla
Dipòsit Legal: T 891-2015

photocurrent. So the active region of the planar bilayer OSC should have a thickness comparable to the exciton diffusion length of the material. However, such thin layer will not be able to absorb all the photons that otherwise it would absorb if it were infinitely thick. Hence, the active region must be also thick enough from the point of view of light absorption. So the optimal thickness for this architecture should be a trade-off of these two opposite conditions. This fact limits the efficiency of planar bilayer OSC.

2.4.3.- BULK HETEROJUNCTION

To try to compensate the issue that the short exciton diffusion length of the organic semiconductors represents to the efficiency of the devices, a new architecture was developed. It was the bulk heterojunction (BHJ) configuration. The principle of operation of this architecture is the same than that of the planar bilayer. Excitons are dissociated in the D–A interface and each free carrier is transported though the corresponding semiconductor to the electrodes. But now, the donor and the acceptor materials are blended together in an interpenetrating mixture instead of being two different layers (Figure 2.11).

An important advantage of this kind of structure is that here the D–A exciton dissociation interface is much more extensive than in the planar bilayer architecture. The blend is so interpenetrated that, ideally, all the generated excitons will be able to dissociate by finding the D–A interface before recombine since distances will be lower that the main exciton diffusion lengths of the materials. So, with this architecture it was expected to achieve high efficiencies.

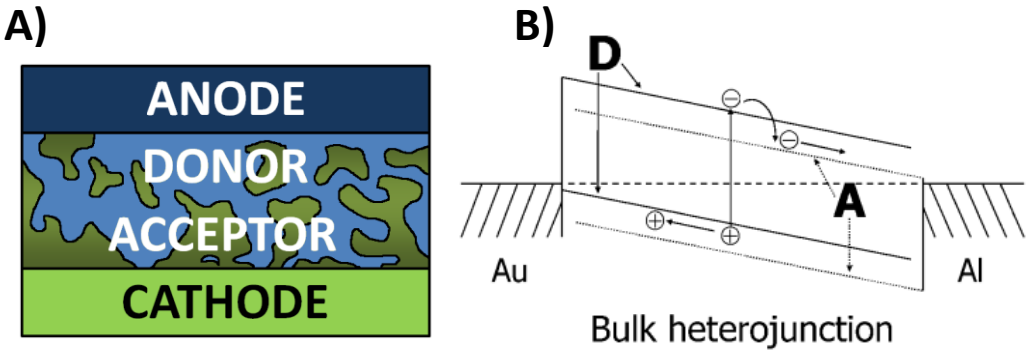

Figure 2.11 *Scheme of a bulk heterojunction OSC architecture (A) and of the exciton dissociation and charge transport (B) [Hoppe-2004].*

The BHJ configuration was reported for the first time in 1995 by Yu *et al.* [Yu-1995]. Their devices used poly(2-methoxy-5-(2'-ethylhexyloxy)-1,4- phenylene vinylene) (MEH-PPV, a conjugated polymer) as the electron donor, and buckminsterfullerene (C_{60}, a fullerene) derivatives as the electron acceptor. Due to problems of solubility and crystallization during the formation of thin films of pure C_{60}, they used the C_{60} derivatives [5,6]-PCBM and [6,6]-PCBM to improve the results. In Figure 2.12 it is shown the molecular structure of the organic semiconductors and the schematic of the complete device.

With this architecture they achieved an efficiency of 1.45% for the case of a blend MEH-PPV:[6,6]-PCBM with a concentration of 1:4. From then, the BHJ configuration became one of the most studied architectures and, with small modifications, the one that had bring higher efficiencies.

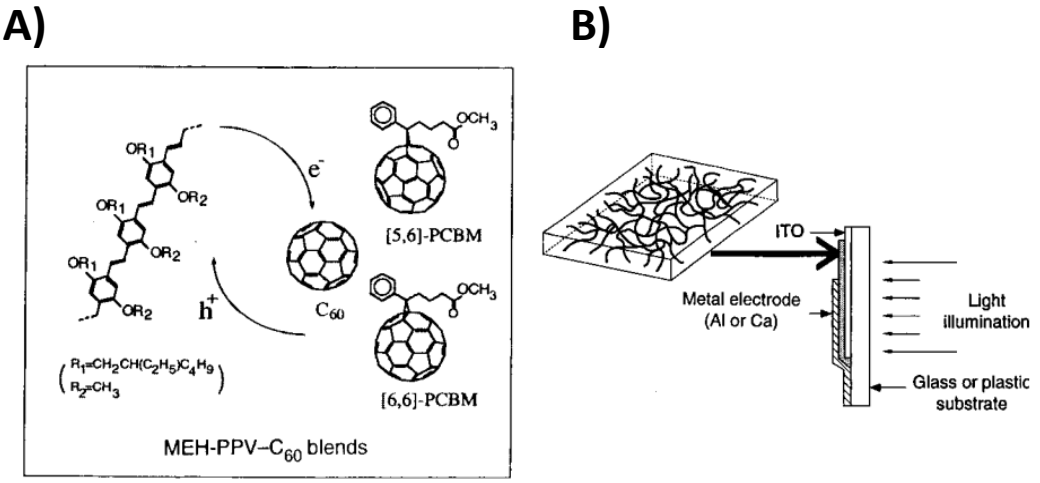

Figure 2.12 *Charge transference process at the D–A interface in the blend MEH-PPV:C_{60} and the molecular structure of this organic semiconductors used by Yu et al. (A). Schematic of the resulting blend of the two materials and of the complete device (B) [Yu-1995].*

Soon, organics photovoltaics started to get more interest from researchers and its development started to accelerate. In 2004 Xue *et al.* overcame the barrier of the 5% [Xue-2004]. They manufactured a device with a tandem configuration, which means putting different cells one over the previous to absorb a broader range of the solar radiation. In this case, they used two subcells in a series association. Here, the absorption of the incident light is maximized by locating the subcell tuned to absorb long-wavelength light nearest to the transparent anode, and tuning the second subcell closest to the reflecting metal cathode to preferentially absorb short-wavelength solar energy. The achieved efficiency was 5.7%, with an open circuit voltage (V_{oc}) as high as 1.2 V due to this series association.

UNIVERSITAT ROVIRA I VIRGILI
DESIGN AND MODELLING OF INTERDIGITATED AND NANOSTRUCTURED POLYMER SOLAR CELLS
Pedro Granero Secilla
Dipòsit Legal: T 891-2015

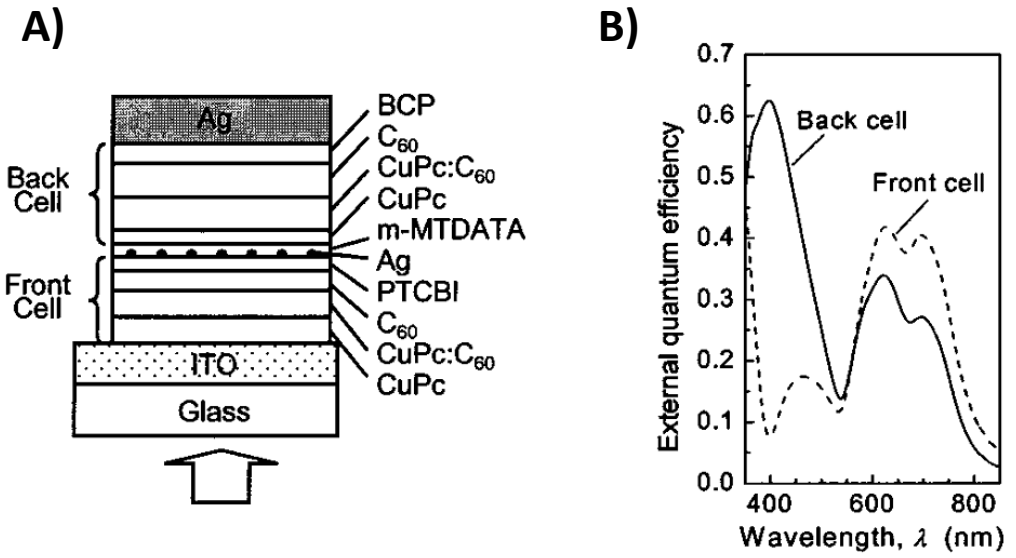

Figure 2.13 *Schematic of the tandem cell of Xue et al. (A) and a graph of the EQE as a function of the wavelength. It also can be seen the contribution of each subcell (B). The asymmetric spectral responses from the two subcells result from the placement of the layers within the asymmetric tandem cell structure [Xue-2004].*

Another example of the good results of the tandem configuration is the work reported by Kim *et al.* [Kim-2007] in 2007, who manufactured the devices shown in Figure 2.14A. This OSC consist in two subcells, each one with an architecture BHJ with semiconducting polymers as electrons donors and fullerene derivatives as electron acceptors. By choosing organic materials with different and complementary absorption spectra, it is possible to absorb a broader range of the solar radiation. A transparent titanium oxide (TiO_x) layer separates and connects the two sections. This TiO_x layer serves both as an electron transport and recollection layer for the frontal subcell and as a support to fabricate the back subcell. With this configuration they achieved an efficiency of 6.7% in the solar energy conversion process.

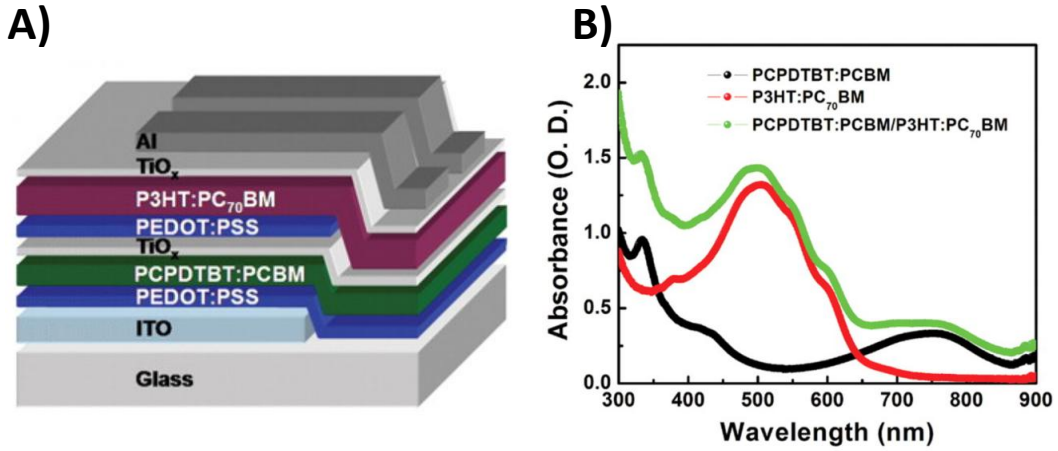

Figure 2.14 *Schematic of the tandem devices of Kim et al. (A) an the graph of absorbance as a function of the wavelength for each subcell and for the complete device (B).*

Nowadays, one of the most promising ways to increase the efficiency in BHJ OSC is by creating new organic semiconductors or improving already existing ones. Special attention has been put in the electron donor material, which are usually conjugated polymers. Ideally, these materials should have a high hole mobility for a proper charge transport, and an extended absorption spectrum for a high exciton generation rate. Additionally, the energy levels of the materials should be appropriated to the electron acceptors. This includes a high HOMO level (absolute value), to produce a high V_{oc}, and a LUMO level with a proper offset with respect to the electron acceptor, to maximize charge carriers separation. Finally, the electron donor should allow an interpenetrating blend with the electron acceptor in the range of the exciton diffusion length.

In this line, Liang *et al.* [Liang-2010] developed a new family of semiconducting polymers based on alternating ester substituted thieno[3,4-*b*]thiophene and

UNIVERSITAT ROVIRA I VIRGILI
DESIGN AND MODELLING OF INTERDIGITATED AND NANOSTRUCTURED POLYMER SOLAR CELLS
Pedro Granero Secilla
Dipòsit Legal: T 891-2015

benzodithiophene units in 2010. These polymers have a very interesting combination of properties from the point of view of organic photovoltaics:

- Relatively low bandgap (1.6 eV), to take advantage of a broad solar spectrum.

- Good hole mobility, for an efficient charge carriers transport.

- Good solubility in organic solution and suitable miscibility (ability of being mix in any ratio producing a homogenous solution) with the fullerene acceptor, to allow a correct blend formation.

- High HOMO level (absolute value), for a high V_{oc}.

All these characteristics make the PTBs family a good choice for the donor material in BHJ OSC. Among all of them, PTB7 showed the best results in terms of efficiency. Blended together with $PC_{71}BM$ as the electron acceptor to form a BHJ structure, an efficiency of 7.4 % was achieved.

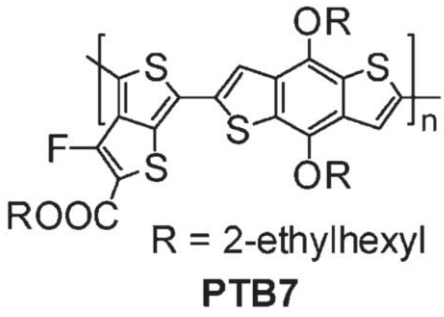

Figure 2.15 *Molecular structure of PTB7.*

Nowadays, the highest reported and confirmed efficiency in an OSC was achieved by Mitsubishi Chemical in 2011, being of 11.1% [Service-2011; Green-2014]. Although the BHJ architecture is still the most efficiency configuration, it has some issues that limit the potential of the OSC. For the case of the planar bilayer configuration, we have that the donor and the acceptor materials connect the anode and the cathode respectively through direct paths selectively. This not always happens for the BHJ configuration, since in this case we have a disordered blend. If the blend is not perfectly bicontinuous and interpenetrated, some regions of the donor and the acceptor materials can easily become isolated without direct paths for the charge carriers to the respective electrodes. These carriers will not contribute to the photocurrent and will be lost due to recombination. Hence, to achieve high efficiencies with BHJ devices, we must control perfectly the blend morphology. However this constraint is not easy to achieve.

2.4.4.- INTERDIGITATED APPROACH

One promising alternative to the BHJ architecture is the interdigitated heterojunction approach. Developed in recent years, this architecture provides devices with a widespread D–A interface. The advantage over the bulk heterojunction approach is that the interdigitated cells provide uninterrupted direct paths for charge carrier collection to the electrodes [Hoppe-2004]. However, this advantage is achieved at the expense of a reduced D–A interface area and longer average paths for excitons from the generation point to this interface in comparison with the bulk heterojunction structure. Previous works have shown that the improvements in the electrical behaviour of the interdigitated heterojunction cells can lead to an increase in their efficiency [Kim-2010; Yang-2005; Yu-2011; He-2011; Zheng-2009; Wiedemann-2010].

UNIVERSITAT ROVIRA I VIRGILI
DESIGN AND MODELLING OF INTERDIGITATED AND NANOSTRUCTURED POLYMER SOLAR CELLS
Pedro Granero Secilla
Dipòsit Legal: T 891-2015

The interdigitated D–A interface can be obtained with the template-assisted synthesis method since it allows obtaining nanometer scale structures [Kim-2010; Baek-2009; Kim2-2010; Santos-2010; Palacios-2008; Balderrama-2014]. In previous works, our research group (Nano-Electronic and Photonic Systems, NePhoS, group from the Universitat Rovira i Virgili) demonstrated the possibility of obtaining polymer nanopillars onto indium-tin-oxide (ITO)/coated glass substrates from nanoporous anodic alumina templates (NAAT) [Santos-2010; Balderrama-2014]. Once the NAAT are made [Masuda-1997], the polymer is inserted in the template with a combination of the spin-coating and the melt-assisted template wetting methods. Finally, the NAAT is dissolved in a solution of sodium hydroxide (NaOH), obtaining the polymer nanopillars [Santos-2010; Balderrama-2014]. The detailed process to obtain a complete OSC with a structure Glass/ITO/PEDOT:PSS/P3HT-Nanopillars/$PC_{70}BM$/Ca/Ag is showed in Figures 2.16 and 2.17.

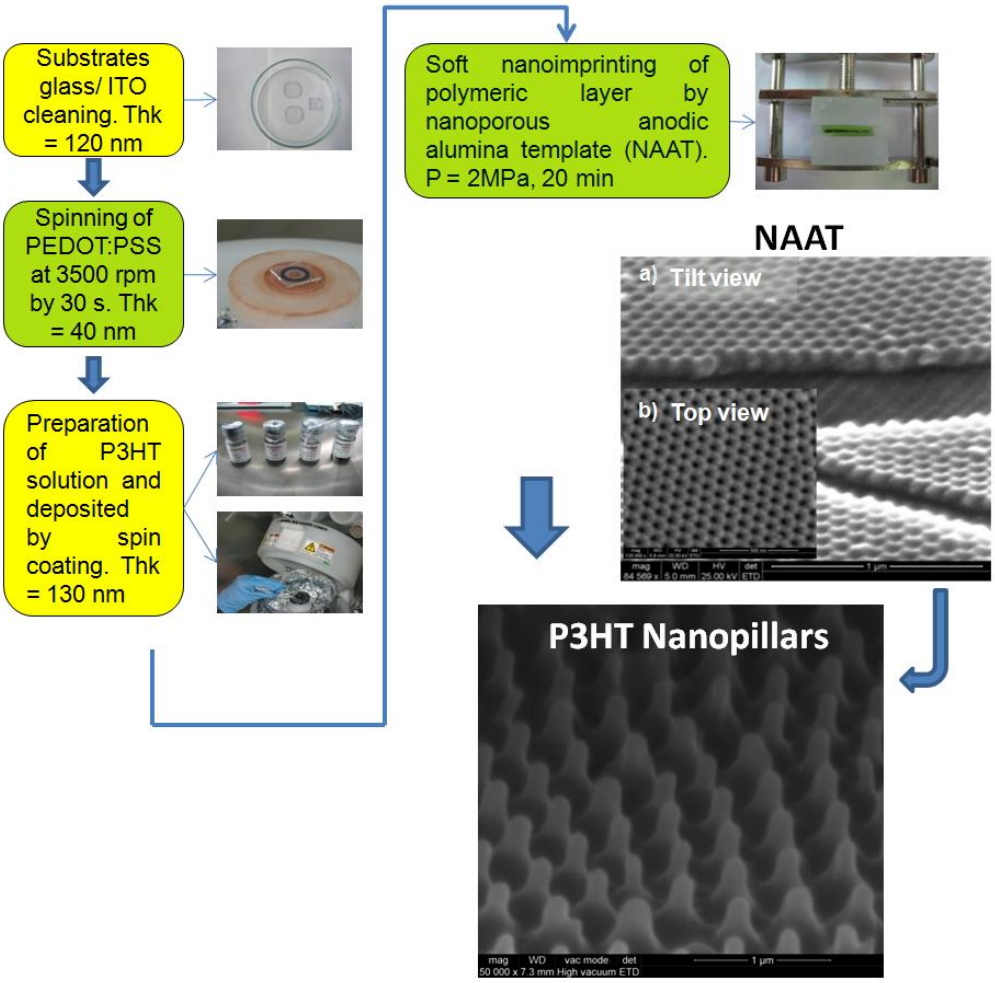

Figure 2.16 *Detailed process to obtain an interdigitated heterojunction OSC with a structure Glass/ITO/PEDOT:PSS/P3HT-Nanopillars/$PC_{70}BM$/Ca/Ag (first part) [Balderrama-2014]. Thk stands for thickness.*

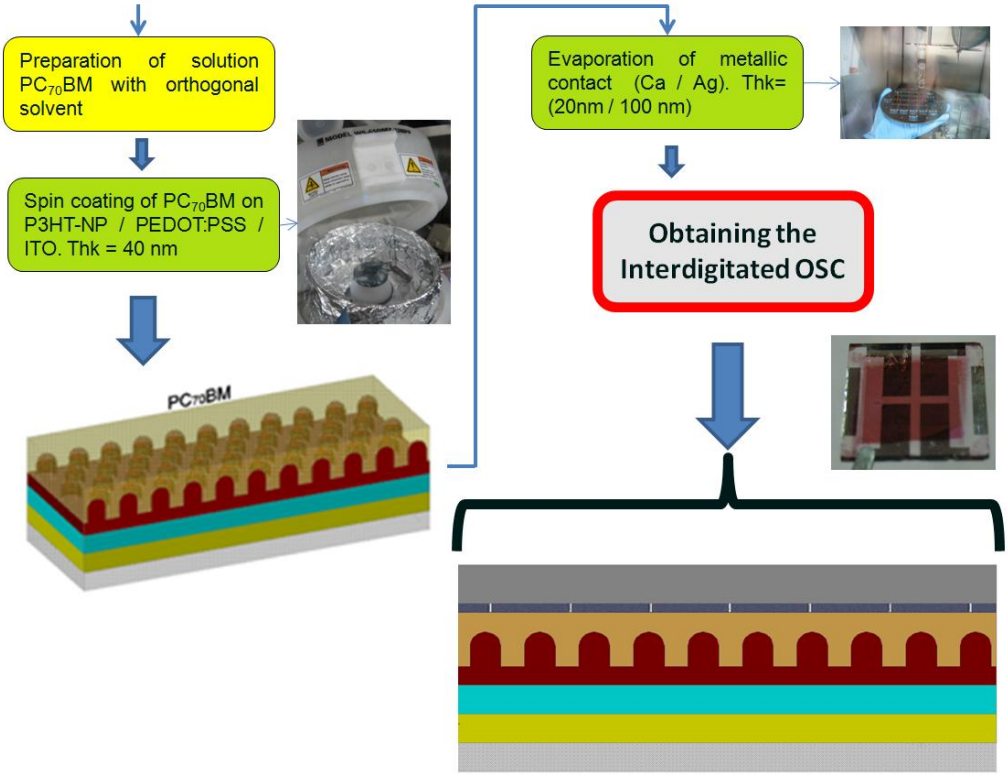

Figure 2.17 *Detailed process to obtain an interdigitated heterojunction OSC with a structure Glass/ITO/PEDOT:PSS/P3HT-Nanopillars/$PC_{70}BM$/Ca/Ag (second part) [Balderrama-2014]. Thk stands for thickness.*

The geometrical features of the NAAT such as pore diameter, interpore distance, porosity, degree of hexagonal pore arrangement and thickness are rather controllable by the anodization parameters (anodization voltage, temperature, and type and concentration of the acid electrolyte) [Masuda-1997]. Figure 2.18 shows two environmental scanning electron microscopy (*ESEM*) images of poly(3-hexylthiophene) (P3HT) nanopillars obtained by using NAAT manufactured under different anodization conditions. Figure 2.18A shows nanopillars with an average height of 380 nm, a diameter of 180 nm and an interpillar distance of 490 nm. The

UNIVERSITAT ROVIRA I VIRGILI
DESIGN AND MODELLING OF INTERDIGITATED AND NANOSTRUCTURED POLYMER SOLAR CELLS
Pedro Granero Secilla
Dipòsit Legal: T 891-2015

nanopillars are standing on a 220 nm thick P3HT base layer, which is in contact with the ITO-coated glass. Figure 2.18B shows P3HT nanopillars on a 260 nm thick base layer and with 100 nm height, 70 nm diameter and 100 nm interpillar distance.

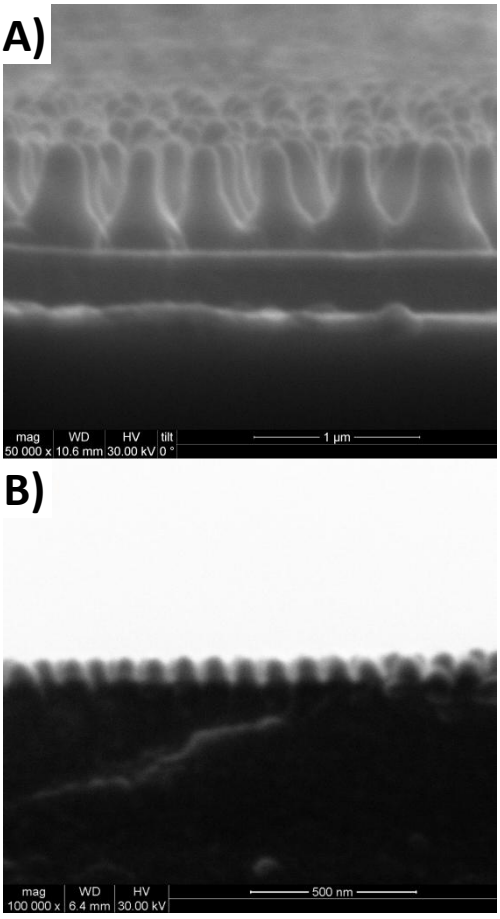

Figure 2.18 *Environmental scanning electron microscopy (ESEM) cross section image of P3HT nanopillars with 380 nm high, 180 nm diameter and 490 nm interpillar distance (A) and of P3HT nanopillars with 100 nm high, 70 nm diameter and 100 nm interpillar distance (B).*

UNIVERSITAT ROVIRA I VIRGILI
DESIGN AND MODELLING OF INTERDIGITATED AND NANOSTRUCTURED POLYMER SOLAR CELLS
Pedro Granero Secilla
Dipòsit Legal: T 891-2015

Although nowadays the BHJ architecture is still reaching the higher efficiencies, an optimization of the interdigitated D–A interface and a better understanding of this kind of structures can contribute to increase the efficiency in OSC and, possibly, will lead to the next technological leap in organic photovoltaics.

2.5.- REVIEW OF NUMERICAL MODELLING METHODS FOR ORGANIC SOLAR CELLS

In many fields, numerical simulation models have helped to develop many technologies and understand their mechanisms. They are able to predict results without the need to fabricate real devices. This fact allows reducing development times, since simulations are faster than a device fabrication, and costs, since material waste from fabricating non-optimal devices can be reduced. Since many years ago, several models exist for the case of inorganic cells, however the behaviour of OSC is still not perfectly known. We can find some studies reporting OSC models [Pettersson-1999; Barker-2003; Paulus-2012; Koster-2005; Andersson-2008; Dennler-2007; Kirchartz-2008; Shang-2011; Kotlarski-2008; Yang-2008; Meng-2010; Kim-2011; Raba-2014]. Nevertheless, most of them correspond to the planar bilayer or the bulk heterojunction architecture. For the case of the interdigitated approach, the topic of this thesis, it is more difficult to find previously reported work [Yang-2008; Meng-2010; Kim-2011; Raba-2014].

The cases of the bulk heterojunction architecture models [Koster-2005; Andersson-2008; Dennler-2007; Kirchartz-2008; Shang-2011; Kotlarski-2008] are difficult to compare with the interdigitate ones since the active regions are blends of the different organic semiconductors. These blends are usually considered effective mediums of the two materials that conforms them. On the other hand, we have that the planar bilayer architecture is closer to the interdigitated one, since in both cases

the donor and the acceptor materials are not mixed together [Pettersson-1999; Barker-2003; Paulus-2012].

Regarding interdigitated OSC models, Yang *et al.* [Yang-2008] have simulated the photocurrent generation in interdigitated devices by using a dynamical Monte Carlo model that includes the generation and transport properties of both excitons and free charges. They compare planar and planar-mixed heterojunction structures, homogeneous and phase-separated Donor–Acceptor (D–A) mixtures, idealized structures composed of D–A pillars, and nanocrystalline D–A networks. Despite their extensive study, only values for the internal and external quantum efficiencies are calculated while the achievable energy conversion efficiencies are only estimated by using typical experimental values for the open circuit voltage and the *Fill Factor*.

The method proposed by Meng *et al.* [Meng-2010] method describes the main processes (the generation, diffusion, and dissociation at the interface of the excitons; and the drift, the injection from the electrodes, and the collection by the electrodes of the charge carries) in the OSC also by the dynamic Monte Carlo approach. In their simulations, excitons are created at randomly chosen sites in either the hole or electron conducting polymer at constant rate, neglecting light wave features such as diffraction and interferences.

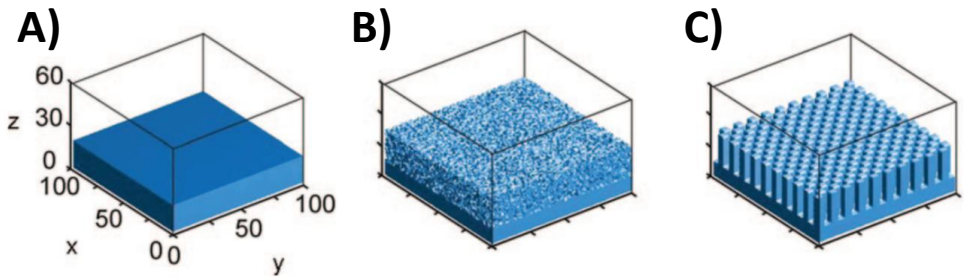

Figure 2.19 *Models used in Yang et al. study.* (A) *Planar bilayer, (B) bulk heterojunction, and (C) interdigitate configurations.*

UNIVERSITAT ROVIRA I VIRGILI
DESIGN AND MODELLING OF INTERDIGITATED AND NANOSTRUCTURED POLYMER SOLAR CELLS
Pedro Granero Secilla
Dipòsit Legal: T 891-2015

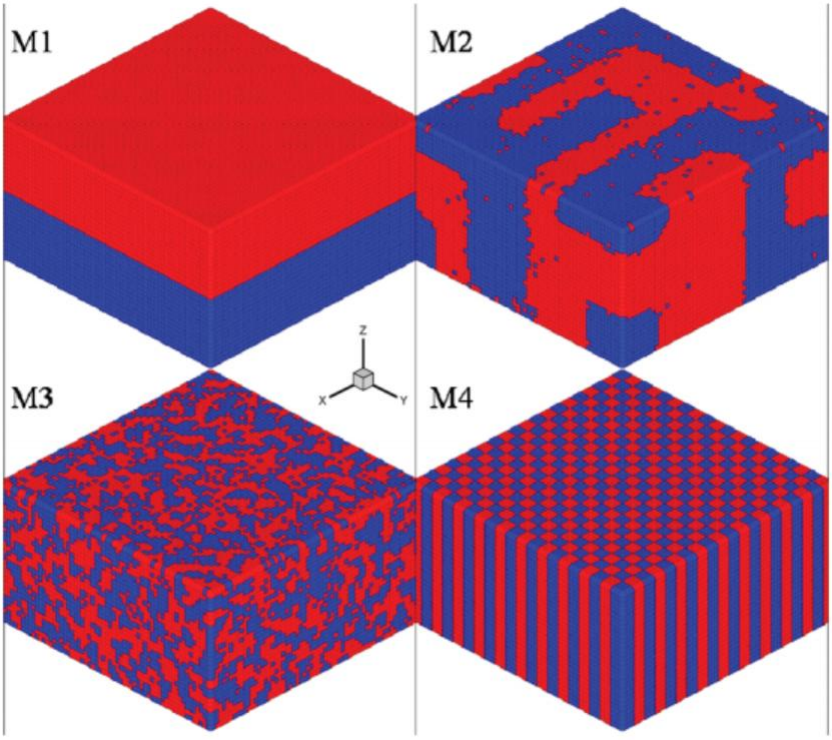

Figure 2.20 *Models used in Meng et al. study. M1 is a planar bilayer, M2 and M3 are blends, and M4 is an interdigitated structure.*

A more accurate model has been presented by Kim *et al.* [Kim-2011]. In their approach the absorbed light in the active layer was computed by considering the wave nature of light with Maxwell's equations and the photocurrent density was calculated by considering the generation, diffusion, and dissociation of excitons following the exciton diffusion equation. However, the electron and hole transport in the polymer materials were computed using an equivalent circuit model.

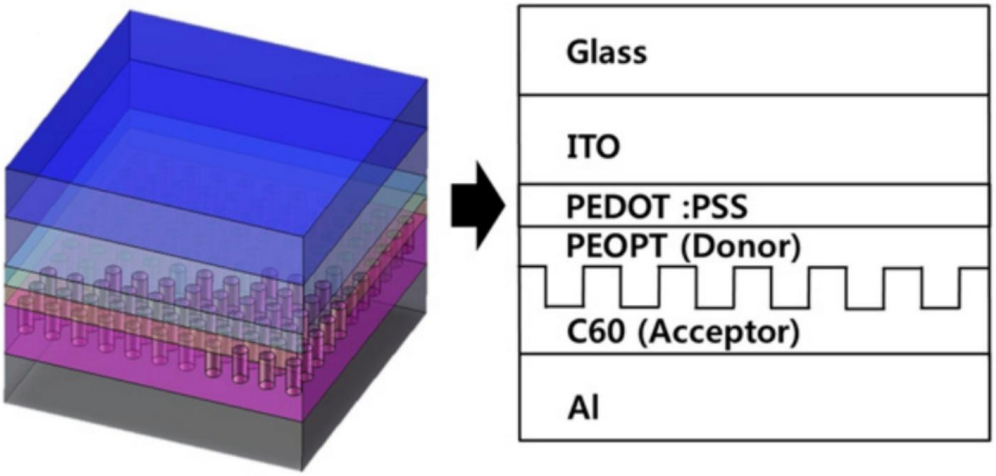

Figure 2.21 *Model used in Kim et al. study. The interdigitated D–A interface geometry was variable.*

Raba *et al.*, [Raba-2014], proposed a mathematically rigorous approach to generate the current density–voltage (*J*–*V*) characteristics of OSC. Their model includes charge transfer (CT) states as intermediate states between the excitons and the free carriers. The CT state was assumed to be pinned at the interface between the donor and acceptor domains and is thus explicitly considered as a 2D species. Consequently, their model allows taking into account the morphology of the active layer, contrarily to the 1D models commonly used. The rigorous derivation of the boundary conditions associated with the interface between the donor and acceptor domains, a critical point for models that treat the interface as a 2D surface, is also detailed and entails an integral formulation. Despite the complex and detailed electrical modelling in their work, they used a constant exciton generation rate, avoiding the use of an optical model.

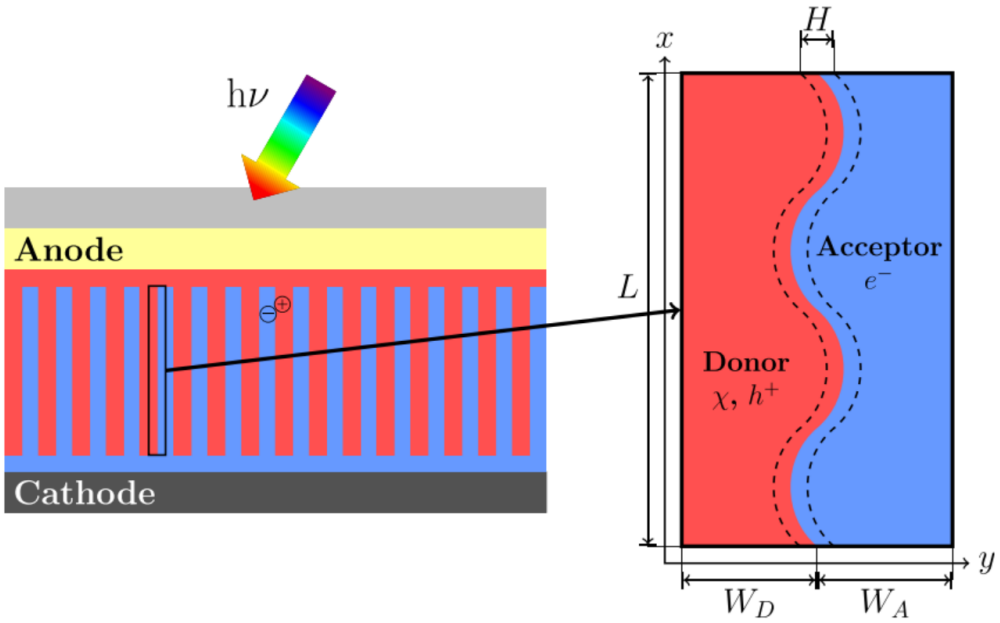

Figure 2.22 *Model used in Raba et al. study.*

The novelty of the work presented in this Ph. D. dissertation, if compared with these examples of previous reported studies, is that in our case we develop a numerical model, based on the finite elements method, for the complete simulation of interdigitated heterojunction full organic solar cells. We integrate in the same model the different steps of the solar energy conversion process: light propagation and absorption, exciton diffusion, and charge carrier transport. The main advantages of such approach is that it allows evaluating all the relevant magnitudes as a function of position and that the result of each step can be used seamlessly as the input for the next step. This method will be explained in next chapter.

UNIVERSITAT ROVIRA I VIRGILI
DESIGN AND MODELLING OF INTERDIGITATED AND NANOSTRUCTURED POLYMER SOLAR CELLS
Pedro Granero Secilla
Dipòsit Legal: T 891-2015

UNIVERSITAT ROVIRA I VIRGILI
DESIGN AND MODELLING OF INTERDIGITATED AND NANOSTRUCTURED POLYMER SOLAR CELLS
Pedro Granero Secilla
Dipòsit Legal: T 891-2015

CHAPTER 3

NUMERICAL SIMULATION OF THE STEPS OF THE SOLAR ENERGY CONVERSION PROCESS IN ORGANIC SOLAR CELLS

3.1.- THE FINITE-ELEMENT METHOD

In mathematics, the finite-element method (FEM) is a numerical technique for finding approximate solutions to boundary value problems for partial differential equations. It uses subdivision of a whole problem domain into simpler parts, called finite elements, and variational methods from the calculus of variations to solve the problem by minimizing an associated error function. Analogous to the idea that connecting many tiny straight lines can approximate a larger circle, FEM encompasses methods for connecting many simple element equations over many small subdomains, named finite elements, to approximate a more complex equation over a larger domain [Reddy-2005].

UNIVERSITAT ROVIRA I VIRGILI
DESIGN AND MODELLING OF INTERDIGITATED AND NANOSTRUCTURED POLYMER SOLAR CELLS
Pedro Granero Secilla
Dipòsit Legal: T 891-2015

The subdivision of a whole domain into simpler parts has several advantages:

- Accurate representation of complex geometry
- Inclusion of dissimilar material properties
- Easy representation of the total solution
- Capture of local effects

A typical work out of the method involves (1) dividing the domain of the problem into a collection of subdomains, with each subdomain represented by a set of element equations to the original problem, followed by (2) systematically recombining all sets of element equations into a global system of equations for the final calculation. The global system of equations has known solution techniques, and can be calculated from the initial values of the original problem to obtain a numerical answer.

In the first step above, the element equations are simple equations that locally approximate the original complex equations to be studied, where the original equations are often partial differential equations (PDE). To explain the approximation in this process, FEM is commonly introduced as a special case of Galerkin method. The process, in mathematical language, is to construct an integral of the inner product of the residual and the weight functions and set the integral to zero. In simple terms, it is a procedure that minimizes the error of approximation by fitting trial functions into the PDE. The residual is the error caused by the trial functions, and the weight functions are polynomial approximation functions that project the residual. The process eliminates all the spatial derivatives from the PDE, thus approximating the PDE locally with:

- a set of algebraic equations for steady state problems
- a set of ordinary differential equations for transient problems

These equation sets are the element equations. They are linear if the underlying PDE is linear, and vice versa. Algebraic equation sets that arise in the steady state problems are solved using numerical linear algebra methods, while ordinary differential equation sets that arise in the transient problems are solved by numerical integration using standard techniques such as Euler's method or the Runge-Kutta method.

In step (2) above, a global system of equations is generated from the element equations through a transformation of coordinates from the subdomains' local nodes to the domain's global nodes. This spatial transformation includes appropriate orientation adjustments as applied in relation to the reference coordinate system. The process is often carried out by FEM software using coordinate data generated from the subdomains.

FEM is best understood from its practical application, known as finite element analysis (FEA). FEA as applied in engineering is a computational tool for performing engineering analysis. It includes the use of mesh generation techniques for dividing a complex problem into small elements, as well as the use of software program coded with FEM algorithm. In applying FEA, the complex problem is usually a physical system with the underlying physics such as the Euler-Bernoulli beam equation, the heat equation, or the Navier-Stokes equations expressed in either PDE or integral equations, while the divided small elements of the complex problem represent different areas in the physical system.

UNIVERSITAT ROVIRA I VIRGILI
DESIGN AND MODELLING OF INTERDIGITATED AND NANOSTRUCTURED POLYMER SOLAR CELLS
Pedro Granero Secilla
Dipòsit Legal: T 891-2015

FEA is a good choice for analyzing problems over complicated domains (like cars and oil pipelines), when the domain changes (as during a solid state reaction with a moving boundary), when the desired precision varies over the entire domain, or when the solution lacks smoothness. For instance, in a frontal crash simulation it is possible to increase prediction accuracy in important areas like the front of the car and reduce it in its rear (thus reducing cost of the simulation). Another example would be in numerical weather prediction, where it is more important to have accurate predictions over developing highly nonlinear phenomena (such as tropical cyclones in the atmosphere, or eddies in the ocean) rather than relatively calm areas.

Our work has been carried out on the basis of the finite-element method by using COMSOL Multiphysics®. This commercial software is a finite element analysis, solver and simulation software / FEA Software package for various physics and engineering applications, especially coupled phenomena, or multiphysics. The packages are cross-platform (Windows, Mac, Linux). In addition to conventional physics-based user interfaces, COMSOL Multiphysics® also allows for entering coupled systems of partial differential equations (PDE). The PDE can be entered directly or using the so-called weak form [COMSOL-2010].

The main product in COMSOL Multiphysics® is COMSOL Desktop which is an integrated user interface environment designed for cross-disciplinary product development with a unified workflow for electrical, mechanical, fluid, and chemical applications. The add-on modules blend into COMSOL Desktop, and the way of operation of the software remains the same no matter which add-on products are engaged. COMSOL Multiphysics® also provides application programming interfaces (APIs). The COMSOL API for use with Java comes included with COMSOL Multiphysics®, and provides a programmatic way of driving the software through

UNIVERSITAT ROVIRA I VIRGILI
DESIGN AND MODELLING OF INTERDIGITATED AND NANOSTRUCTURED POLYMER SOLAR CELLS
Pedro Granero Secilla
Dipòsit Legal: T 891-2015

compiled object oriented code. LiveLink for MATLAB allows to work with COMSOL Multiphysics® in combination with MATLAB.

The Physics Builder, which is included in COMSOL Desktop, allows creating custom made physics interfaces accessible from the COMSOL Desktop with the same look-and-feel as the built-in physics interfaces. In the case of the Physics Builder, no programming is needed as it works in the COMSOL Desktop from the Physics Builder Tree, defining new user interface components. The Applications Builder is also available with COMSOL Desktop and allows saving models as specialized applications for use without going into the details of the simulations model. Two editors are available for designing applications; using drag-and-drop tools, in the Form Editor, or by programming using the Method Editor. There is scope to include specific features from the model or introduce new ones through programming using the Method Editor.

Several add-on products are available for COMSOL Multiphysics®, each one related to one specific field. These modules have been categorized according to several applications areas (Figure 3.1):

- Electrical
- Mechanical
- Fluid
- Chemical
- Multipurpose
- Interfacing

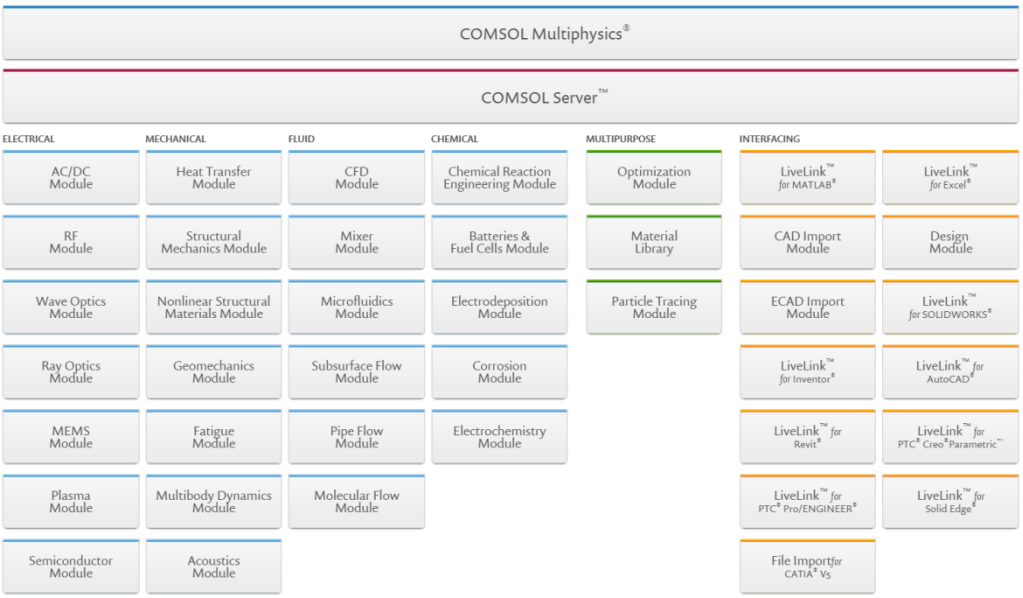

Figure 3.1 *Add-on products available for COMSOL Multiphysics®. These have been categorized according to several applications areas: Electrical, Mechanical, Fluid, Chemical, Multipurpose, and Interfacing. Reproduced from COMSOL Multiphysics® website (http://www.comsol.com).*

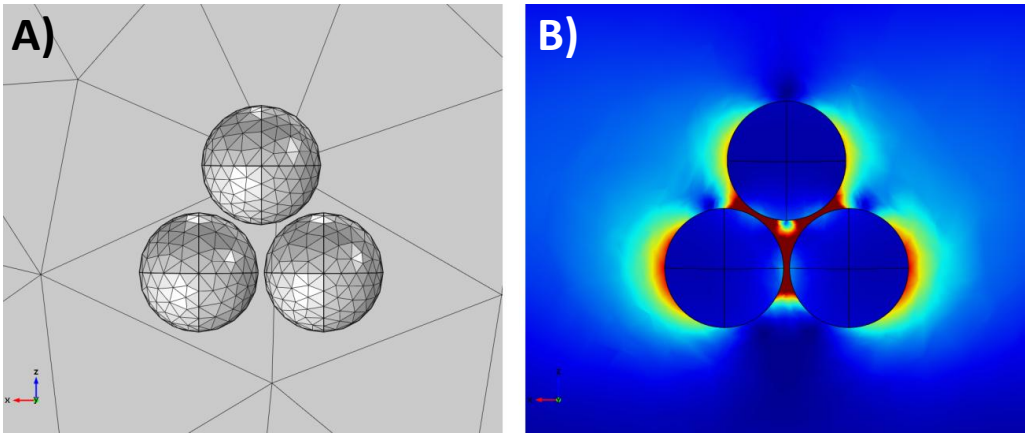

Figure 3.2 *Example of application of the FEM by using COMSOL Multiphysics®. Mesh of calculation points (A) and the resulting map of the amplitude of the electric field, |E| in V/m, for three gold nanospheres when an incident light is applied (B).*

UNIVERSITAT ROVIRA I VIRGILI
DESIGN AND MODELLING OF INTERDIGITATED AND NANOSTRUCTURED POLYMER SOLAR CELLS
Pedro Granero Secilla
Dipòsit Legal: T 891-2015

Figure 3.2 shows an example of application of the FEM by using COMSOL Multiphysics®. In this figure it is depicted the defined mesh of calculation points (Figure3.2A) and the resulting map of the amplitude of the electric field, $|E|$ in V/m, of three gold nanospheres when an incident light is applied (Figure3.2B). As mentioned above, the aim of the FEM is to divide the simulation domain into simpler parts. The use of a mesh of calculation points allow this.

In our work the possibility of using this mesh, which in COMSOL Multiphysics® can be controlled and adapted by the user, is exploited to develop a numerical simulation procedure of the photovoltaic conversion process with all the magnitudes calculated as a function of the position. The complete Maxwell equations, the *exciton diffusion equation*, and the drift-diffusion model are solved within the same numerical framework. The model can be divided into two main parts: the optical and the electrical behaviour. The results of each step of the photovoltaic conversion process are used as an input of the subsequent step, in all cases as a function of the position.

3.2.- OPTICAL MODELLING: LIGHT ABSORPTION

3.2.1.- OPTICAL SIMULATION PROCEDURE

This step of the photovoltaic conversion process has been modelled by using the RF Module of COMSOL Multiphysics®. This module is required to model electromagnetic fields, currents and waves for radio frequency (RF), microwave, optical, and other high-frequency devices [COMSOL RF-2010].

The finite-element method allows the simulation of light propagation inside the cell nanostructure and the computing of the absorbed light power as a function of the

position. This magnitude, obtained by solving the complete Maxwell equations, is expressed as the *total power dissipation density* (*Q)*. At any position $\vec{r}$ in the structure, such dissipation $Q(\vec{r};\lambda)$, expressed in W/m^3, for a monochromatic wave of wavelength λ is defined as follows [Andersson-2008]:

$$Q(\vec{r};\lambda) = \left\langle -\vec{\nabla}\cdot\vec{S} \right\rangle \tag{3.1}$$

where $\vec{S}$ is the Poynting vector, which represents the energy flux (in W/m^2) of an electromagnetic field [Born-Wolf-1999]. The *total power dissipation density* that will contribute to exciton generation is obtained by integrating *Q* over the entire active area.

However, we only have considered the excitons generated in the donor material layer (in our case P3HT) since the contribution to the photocurrent of the ones generated in the acceptor material (in our studies PCBM) will be very small. The exciton diffusion length in the acceptor material is very short so most of the excitons will recombine before reaching the dissociation interface [Burkhard-2009; Cook-2009]. This happens even for the case of the bulk heterojunction approach where the internal quantum efficiency (IQE) is very low for the wavelengths where PCBM absorbs and P3HT does not (around 700 nm) [Brabec-2004; Dennler-2007]. In addition, light absorption in the PCBM is weak at these wavelengths [Defranoux-2010]. Hence, in order to reduce computational times, we have neglected the excitons generated in the PCBM. So only the *total power dissipation density* in the P3HT layer will be analyzed:

$$Q(\lambda) = \int_{P3HT} Q(\vec{r};\lambda)dV \,. \tag{3.2}$$

Then, by summing it for all wavelengths, we obtain the total light absorption of a device for the incident light source:

$$Q_{Total} = \sum_i Q(\lambda_i). \tag{3.3}$$

3.2.2.- MODEL VALIDATION

In the simulation studies it is always important to know if the implemented numerical procedure is reproducing in an accurate manner the real devices behaviour. A usual way to procedure is by comparing the obtained results with the ones obtained with a different simulation tool for the same device model. In our case we have make a comparison between our numerical procedure and the program OpenFilters for the case of bulk heterojunction organic solar cells.

OpenFilters is an open-source program, under the GNU General Public License, an open-source license, for the design of optical filters. It is programmed in Python and C++, and the graphical user interface is implemented with wxPython. It allows creation of multilayer and graded-index filters and calculation of reflection, transmission, absorption, phase, group delay, group delay dispersion, colour, ellipsometric variables, admittance diagram, circle diagram, electric field distribution, and generation of reflection, transmission, and ellipsometric monitoring curves. It also provides the refinement, needle, step, and Fourier transform methods [Larouche-2008].

This program has been developed to simulate optical filters, which are devices that selectively transmit light of different wavelengths, usually implemented as plane glass or plastic devices in the optical path which are either dyed in the bulk or have interference coatings. Optical filters are completely described by their frequency response, which specifies how the magnitude and phase of each frequency

component of an incoming signal is modified by the filter. The different layers of the bulk heterojunction (BHJ) organic solar cells (OSC) can be considered optical filters, since they also transmit light selectively depending on the wavelength of the incident light.

In this section we have calculated the light absorption of bulk heterojunction OSC with the structure ITO/PEDOT:PSS/P3HT:PCBM. The ITO and the PEDOT:PSS layers thicknesses are 180 nm and 45 nm, respectively, while the thickness of the P3HT:PCBM blend have been varied in a range of values. The optical properties of the materials have been modelled by using the refractive index (n) and the extinction coefficient (k) of the complex index of refraction ($\tilde{n} = n + ik$), which have been obtained from the literature [Synowicki-1998; Pettersson-2002; Monestier-2007].

Figures 3.3 and 3.4 show light absorption for a structure of ITO/PEDOT:PSS/P3HT:PCBM for several blend thicknesses for the results obtained by using COMSOL Multiphysics® and OpenFilters. The trend of the absorption curves are very similar between them for any P3HT:PCBM thickness for the cases of the simulations with COMSOL. The curves have a noticeable absorption peak for wavelengths at around 350 nm and then an abrupt decrease of the absorption for wavelengths above the 600 nm. It can be seen also that as the thickness of the P3HT:PCBM increases the light absorption increases too. The same behaviour can be observed in the results given by OpenFilters, with only minor differences. Hence, it can be concluded that our numerical simulation procedure is working correctly since the same results have been achieved with two different simulation methods.

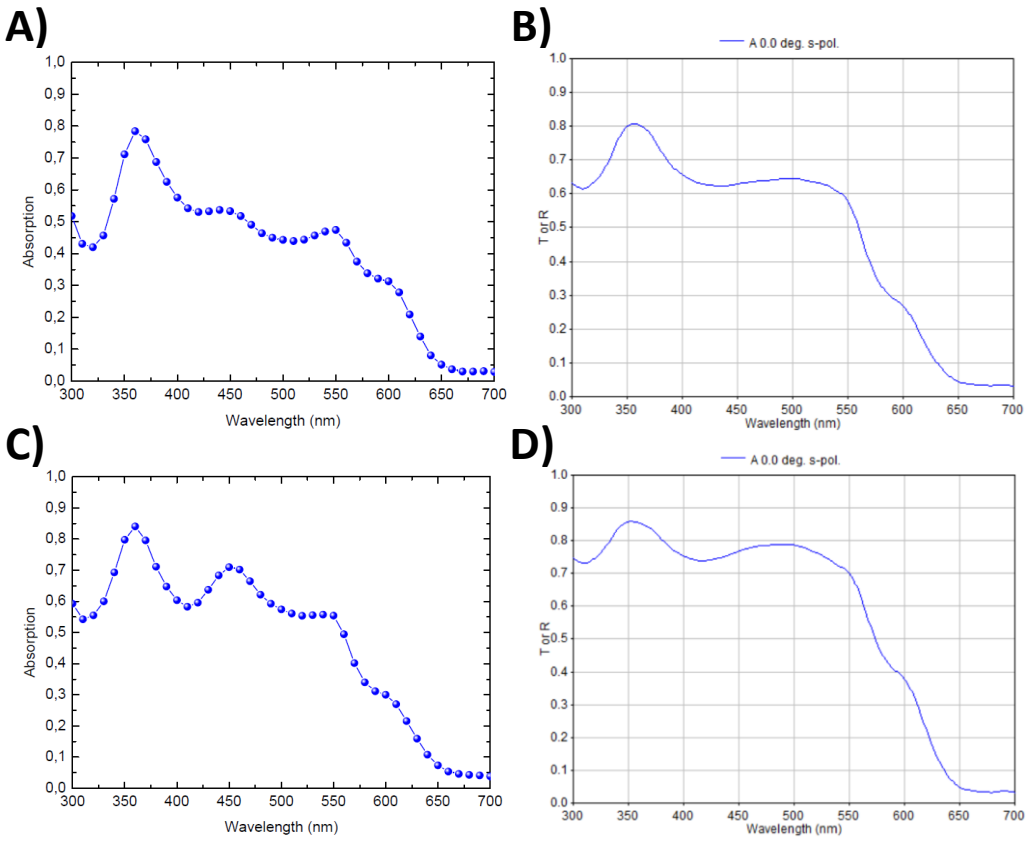

Figure 3.3 *Light absorption for a structure of ITO/PEDOT:PSS/P3HT:PCBM for a blend thickness of 60 nm (A and B) and 100 nm (C and D). Results have been obtained by using COMSOL Multiphysics® (A and C) and OpenFilters (B and D).*

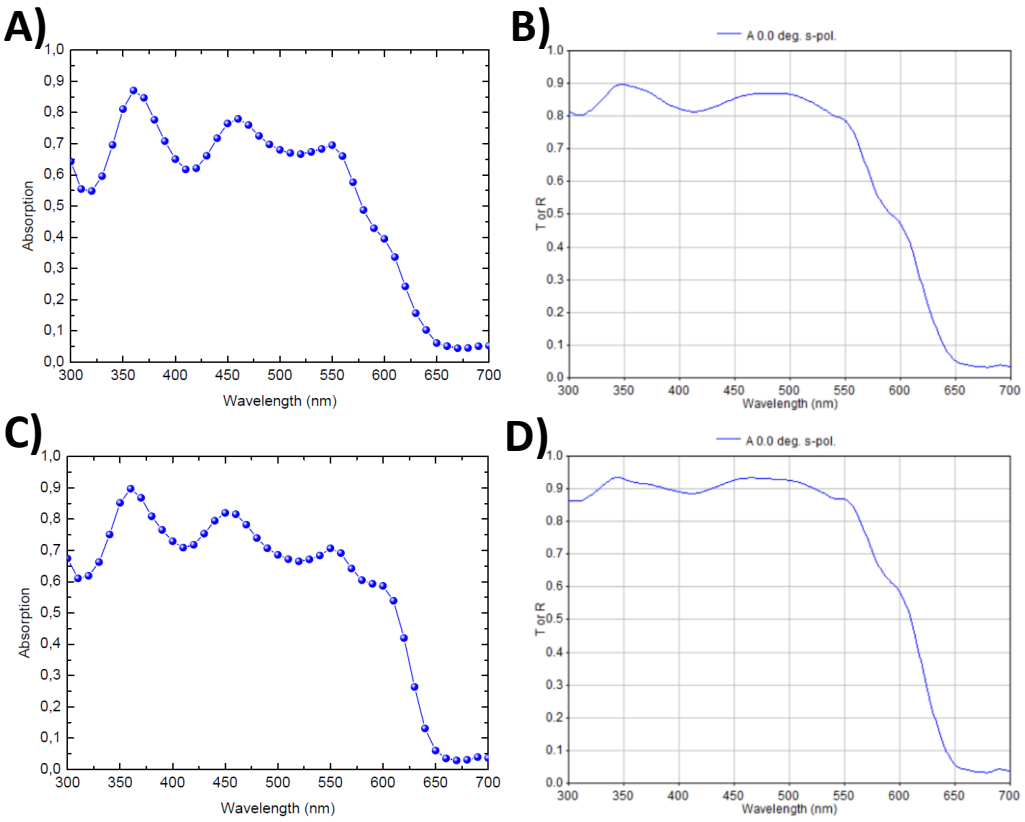

Figure 3.4 *Light absorption for a structure of ITO/PEDOT:PSS/P3HT:PCBM for a blend thickness of 140 nm (A and B) and 200 nm (C and D). Results have been obtained by using COMSOL Multiphysics® (A and C) and OpenFilters (B and D).*

3.2.3.- COMPARISON BETWEEN 2D AND 3D MODELLING

An issue of the FEM is that the computation times increase when increase the amount of calculation points of the mesh. For the case of a complex 3D structure, such as the interdigitated Donor–Acceptor interface of the studied OSC, the resulting computation times can be too large to make systematic studies. So it is necessary to make simplifications in order to obtain acceptable computational times.

In this section, we compare the absorbed light, from a standard AM1.5 light source model, in the P3HT layer of interdigitated OSC by using two models: a 2D and a 3D one. The 2D one (Figure 3.5A) is a simplification of a real 3D device where the nanostructured interface is composed of alternating blocks of each organic material. The advantages of this model over the 3D one are an easier geometry definition, shorter computing times and smaller simulation files. On the other hand, since it is a 2D definition, nanopillars are actually grooves. A more realistic 3D model is presented in Figure 3.5B, where a more complex geometry represents the nanopillars. In both cases we model a structure of indium tin oxide (ITO), Poly(3,4-ethylenedioxythiophene) poly(styrenesulfonate) (PEDOT:PSS), P3HT, PCBM and a back contact of aluminium (Al). The parameters under study are α (nanopillar diameter), β (structure period, 2D, or interpillar distance, 3D, where β = 2α) and *T* (nanopillar height including the supporting base).

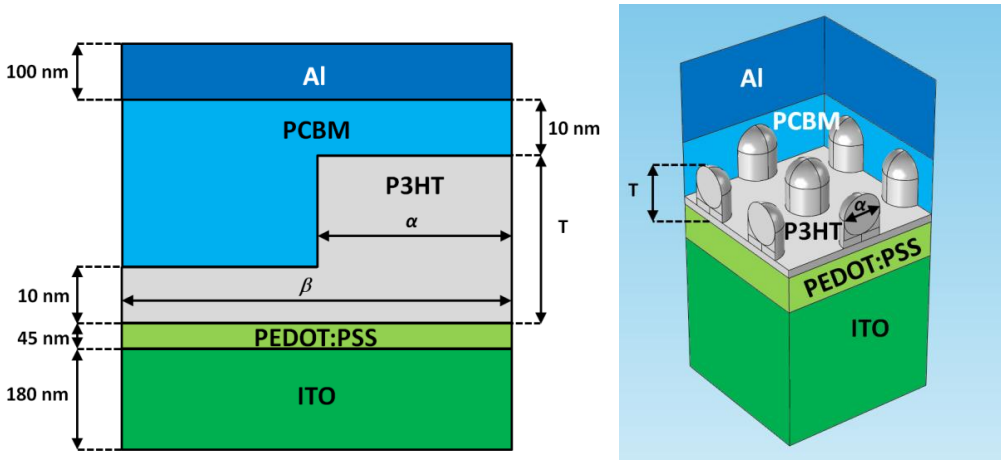

Figure 3.5 *Schematic unit cell (periodic conditions) of the structure ITO/PEDOT:PSS/P3HT/PCBM/Al for (A) the 2D and (B) the 3D models.*

UNIVERSITAT ROVIRA I VIRGILI
DESIGN AND MODELLING OF INTERDIGITATED AND NANOSTRUCTURED POLYMER SOLAR CELLS
Pedro Granero Secilla
Dipòsit Legal: T 891-2015

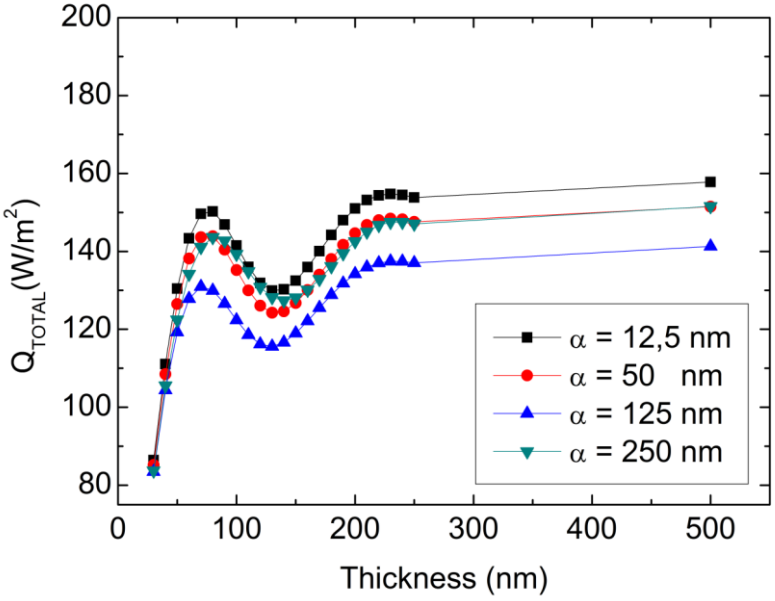

Figure 3.6 *Total absorbed light power (Q_{TOTAL}) in the P3HT layer of the 2D model as a function of the nanopillars height (T) for several nanopillar diameters (α).*

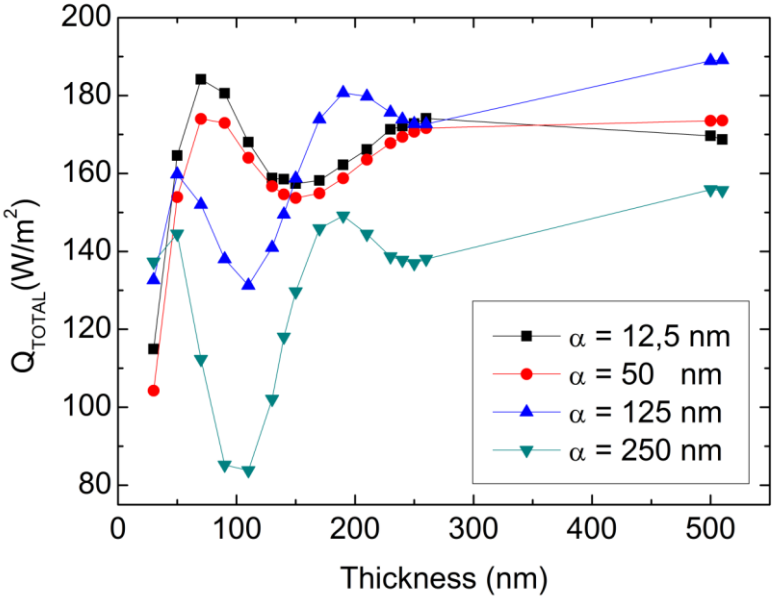

Figure 3.7 *Total absorbed light power (Q_{TOTAL}) in the P3HT layer of the 3D model as a function of the nanopillars height (T) for several nanopillar diameters (α).*

Figure 3.6 shows the total absorbed light power (Q_{TOTAL}) in the P3HT layer as a function of the nanopillars height (T) for several nanopillar diameters (α) for the 2D model. We can see that all the curves have a similar trend with two local maxima for T around 80 nm and 230 nm. A local minimum for T close to 130 nm is also present in all cases. The maximum absorption is achieved for α = 12.5 nm while the lower absorption is clearly for α = 125 nm. Figure 3.7 shows the total absorbed light power (Q_{TOTAL}) in the P3HT layer as a function of the nanopillars height (T) for several nanopillar diameters (α) for the 3D model. In this case we can see that the curves also follow a similar trend but with some differences. For α = 12.5 nm and 50 nm the maximum absorbed light take place for T = 70 nm and 260 nm while there is a local minimum for T = 150 nm. However, for the biggest diameters the local maxima are achieved for a pillar height of 50 nm and 190 nm, and the minimum Q_{TOTAL} take place for T = 110 nm. The amount of absorbed light for each height is also a bit different, being higher for the 3D model.

So, if we compare the results of the two models we can find some discrepancies. These differences come from the fact that in one model we have grooves while in the other there are actual nanopillars. Despite these differences, the two models follow a similar trend and both results are within the same order of magnitude. Hence, a 2D model of a real 3D interdigitated OSC can be a first accurate approximation to make a systematic analysis. However, we should keep in mind that it is not accurate enough to replace totally a 3D model.

UNIVERSITAT ROVIRA I VIRGILI
DESIGN AND MODELLING OF INTERDIGITATED AND NANOSTRUCTURED POLYMER SOLAR CELLS
Pedro Granero Secilla
Dipòsit Legal: T 891-2015

3.2.4.- ANALYSIS OF THE INFLUENCE OF THE ANGLE OF POLARIZATION OF THE INCIDENT LIGHT

Simulation models need to be as much as accurate as possible. However it is difficult to take into account all the possible parameters since it will increase computational times to unviable times, so simplifications must be applied. A simplification that can be applied in our numerical simulation procedure is to consider that the incident light in solar cells is linear polarized while sunlight is not. However simplifications must be checked if they can be applied without losing accuracy in the results. In this section we investigate light absorption in interdigitated heterojunction full OSC for the case of P3HT/PCBM devices. The aim of this study is to determinate if the angle and the polarization of the incident light must be taken in account in the optical simulation models or it can be neglected for a simplified analyse and to reduce computational times.

From the NAAT templates we can obtain devices where the P3HT layer consists of a regular hexagonal distribution of nanopillars. Our computational domain is a 3D model of one of this hexagonal unit cells (Figure 3.8). The model consists of a structure of indium tin oxide (ITO), poly(3,4-ethylenedioxythiophene) poly(styrenesulfonate) (PEDOT:PSS), P3HT, PCBM and aluminium (Al). In order to determinate if the angle of polarization of the incident light (ψ) must be taken in account in the optical simulation models or it can be neglected, we have performed simulations of different light source configurations. The incident light is assumed to be normal to the surface of the devices and incident from the ITO side. It has been modelled as a set of monochromatic waves with a planar wavefront. Since the hexagonal unit cell is symmetric, we only have to check the light polarization in one of the quadrants of the geometry, as it is displayed in Figure 3.9. The polarization angle

ranges from 0 to π/3 radians in intervals of π/12 radians. The optical properties of the materials have been modelled by using the refractive index (*n*) and the extinction coefficient (*k*) of the complex index of refraction ($\tilde{n} = n + ik$). We also have varied the nanopillar diameter ($Ø_{NP}$) and the diameter of the circle that circumscribes the hexagon ($Ø_{HEX}$) to determine if the possible variations in the amount of absorbed light depend on the unit cell geometry. The rest of the geometry remains fixed.

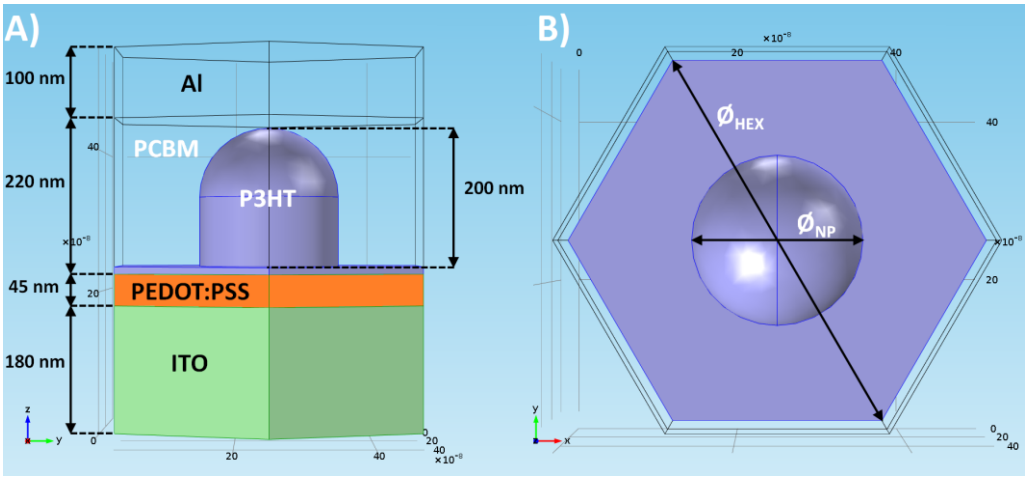

Figure 3.8 *Schematic unit cell (periodic conditions) of the structure ITO/PEDOT:PSS/P3HT/ PCBM/Al. Cross section (A) and top view (B) showing the geometrical characteristics and the variables under study. The residual layer of the nanopillar is 10 nm thick.*

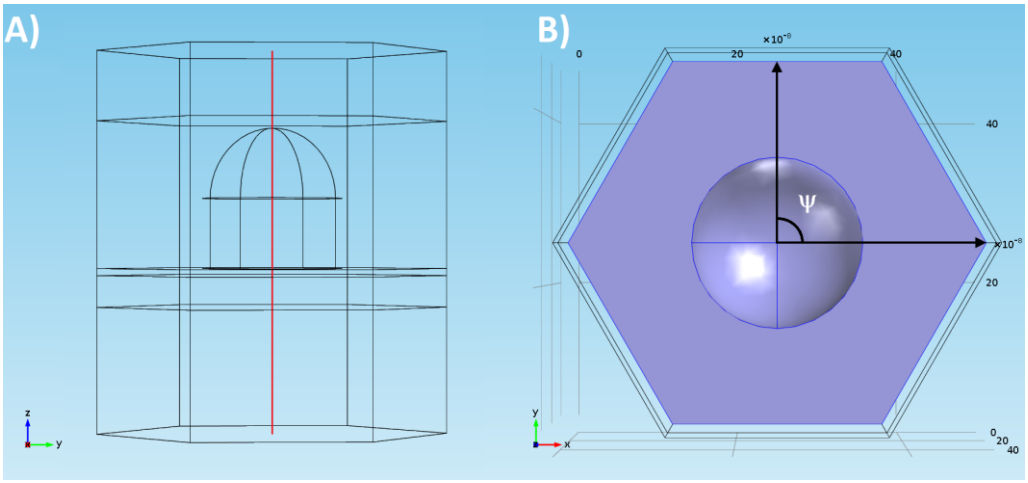

Figure 3.9 *Schematic unit cell (periodic conditions) of the structure ITO/PEDOT:PSS/P3HT/PCBM/Al. Cross section showing the unit cell height (z-direction) along the centre of the nanopillar in red (A) and top view showing the polarization angle (ψ) (B).*

Figure 3.10 shows the *total power dissipation density* as a function of the unit cell height (z-direction) along the centre of the nanopillar for several angles of polarization (ψ), for several $Ø_{NP}$ and $Ø_{HEX}$, for a wavelength of 450 nm: (A) $Ø_{NP}$ = 100 nm, $Ø_{HEX}$ = 500 nm; (B) $Ø_{NP}$ = 100 nm, $Ø_{HEX}$ = 300 nm; (C) $Ø_{NP}$ = 100 nm, $Ø_{HEX}$ = 150 nm; (D) $Ø_{NP}$ = 50 nm, $Ø_{HEX}$ = 500 nm; (E) $Ø_{NP}$ = 200 nm, $Ø_{HEX}$ = 500 nm; (F) $Ø_{NP}$ = 350 nm, $Ø_{HEX}$ = 500 nm. In all six cases the curves show a similar trend. Until the 180 nm, which corresponds with the ITO layer, the amount of absorbed light is very low. This changes in the PEDOT:PSS layer, 180 to 225 nm, which shows a higher power dissipation. However, most of the light is absorbed in the P3HT region, especially in the first tens of nm due to the high absorption coefficient of this material at this wavelength, showing a very high peak. In the following layers the amount of absorbed light is lower since most of the incident light has been absorbed in the P3HT region. In Figures 3.10A, B, C and D we also can see a peak of amount of absorbed light centered on the 400 nm. This height corresponds to the round top of the nanopillar.

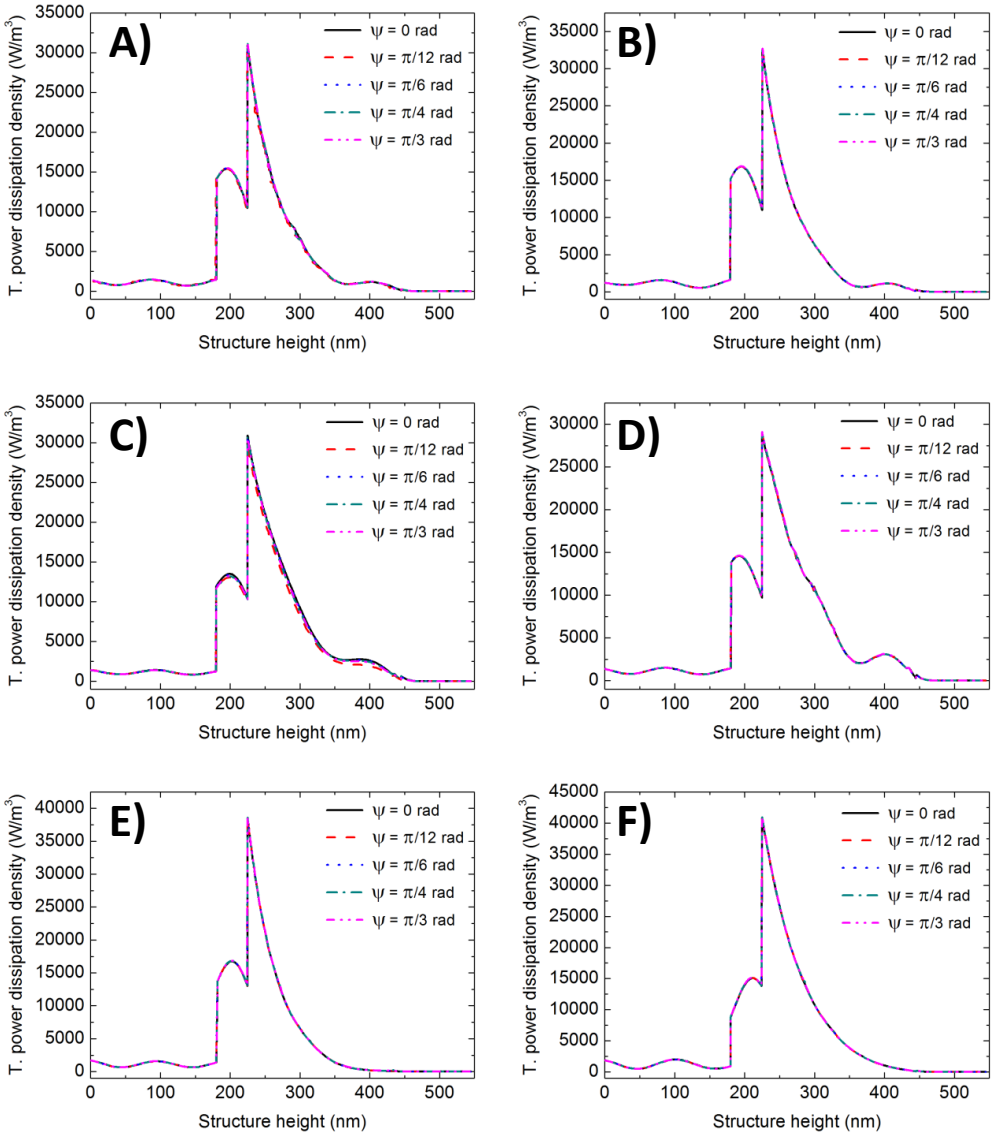

Figure 3.10 *Total power dissipation density as a function of the unit cell height (z-direction) along the centre of the nanopillar for several angles of polarization (ψ), for several $Ø_{NP}$ and $Ø_{HEX}$, for a wavelength of 450 nm: (A) $Ø_{NP}$ = 100 nm, $Ø_{HEX}$ = 500 nm; (B) $Ø_{NP}$ = 100 nm, $Ø_{HEX}$ = 300 nm; (C) $Ø_{NP}$ = 100 nm, $Ø_{HEX}$ = 150 nm; (D) $Ø_{NP}$ = 50 nm, $Ø_{HEX}$ = 500 nm; (E) $Ø_{NP}$ = 200 nm, $Ø_{HEX}$ = 500 nm; (F) $Ø_{NP}$ = 350 nm, $Ø_{HEX}$ = 500 nm.*

Regarding the angle ψ, we can observe a very similar behaviour in each case, especially for the geometries of Figures 3.10 B, E and F. For the other cases, we can find some differences in the amount of the absorbed light for each ψ. However, most of these small dissimilarities occur out of the active region, P3HT volume, that goes from z = 225 to 435 nm. Additionally, the differences that occur inside the active region, as we can see especially in Figures 3.10A and C, are very small. So, they will not affect the exciton generation rate and they can be neglected.

Figure 3.11 shows the *total power dissipation density* as a function of the unit cell height (z-direction) along the centre of the nanopillar for several angles of polarization (ψ), for several wavelengths, and for $Ø_{NP}$ = 100 nm and $Ø_{HEX}$ = 500 nm: (A) λ = 350 nm; (B) λ = 420 nm; (C) λ = 475 nm; (D) λ = 550 nm; (E) λ = 600 nm; (F) λ = 650 nm. Since here we have varied the wavelength of the incident light, the curves are very different between them since the absorption coefficient of the different materials strongly depends of the wavelength. For Figure 3.11A, B and C, most of the light absorption occurs on the P3HT region. For longer wavelengths, Figure 3.11D and E, the absorbed light in the PCBM layer is comparable to the P3HT one. Finally for a wavelength of 650 nm (Figure 3.11F) most of the light is absorbed in the back metal contact since both organic materials, P3HT and PCBM, have a very low absorption in the red-infrared range.

Regarding the polarization angle ψ, as in Figure 3.10, we can observe a very similar behaviour in each case. This angle seems to not affect the amount of absorbed light as only minimum differences between the curves can be observed, mainly in Figure 3.11E around z = 400 nm. So ψ will not modify the amount of absorbed light for the spectrum range that we have to consider to simulate an OSC.

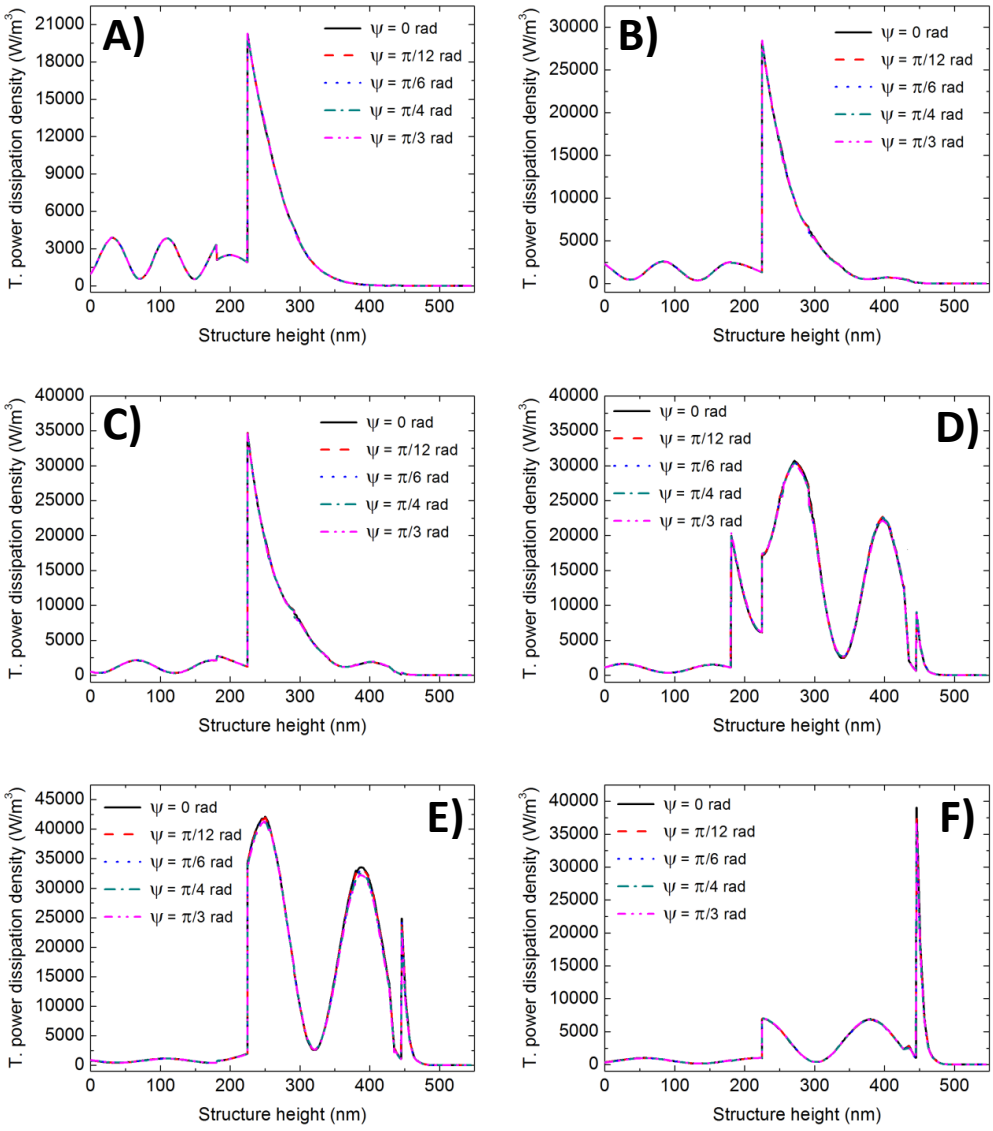

Figure 3.11 *Total power dissipation density as a function of the unit cell height (z-direction) along the centre of the nanopillar for several angles of polarization (ψ), for several wavelengths, and for* $Ø_{NP}$ *= 100 nm and* $Ø_{HEX}$ *= 500 nm: (A) λ = 350 nm; (B) λ = 420 nm; (C) λ = 475 nm; (D) λ = 550 nm; (E) λ = 600 nm; (F) λ = 650 nm.*

UNIVERSITAT ROVIRA I VIRGILI
DESIGN AND MODELLING OF INTERDIGITATED AND NANOSTRUCTURED POLYMER SOLAR CELLS
Pedro Granero Secilla
Dipòsit Legal: T 891-2015

Hence, we can conclude that a single angle computation is enough to obtain good optical simulations for interdigitated OSC with a regular hexagonal lattice distribution. This fact allows reducing computation times being sure that we are not going to lose accuracy in the results and that them will be as much as possible close to experimental studies data.

3.3.- ELECTRICAL MODELLING: EXCITON DIFFUSION, AND CHARGE TRANSPORT AND EXTRACTION

3.3.1.- LINK BETWEEN THE OPTICAL AND THE ELECTRICAL MODEL

One of the advantages of the FEM is that it is possible to obtain the calculated magnitudes as a function of the position. COMSOL Multiphysics® allows extracting them in a text file to facilitate a later use [COMSOL-2010]. In the numerical simulation procedure of this Ph. D. thesis, once an optical simulation is finished the light absorption maps as a function of the position are extracted. They are obtained also as a function of the incident light wavelength. Then, by summing them all, the resulting light absorption map is entered as a part of the exciton generation rate (exc_{gen}) to solve the *exciton diffusion equation*. In Figure 3.12 it is depicted an example of summation of light absorption maps for the absorption wavelength range of P3HT.

$$exc_{gen} = \sum_i \left(\frac{Q(\vec{r};\lambda_i)}{hc/\lambda_i} \right) \tag{3.4}$$

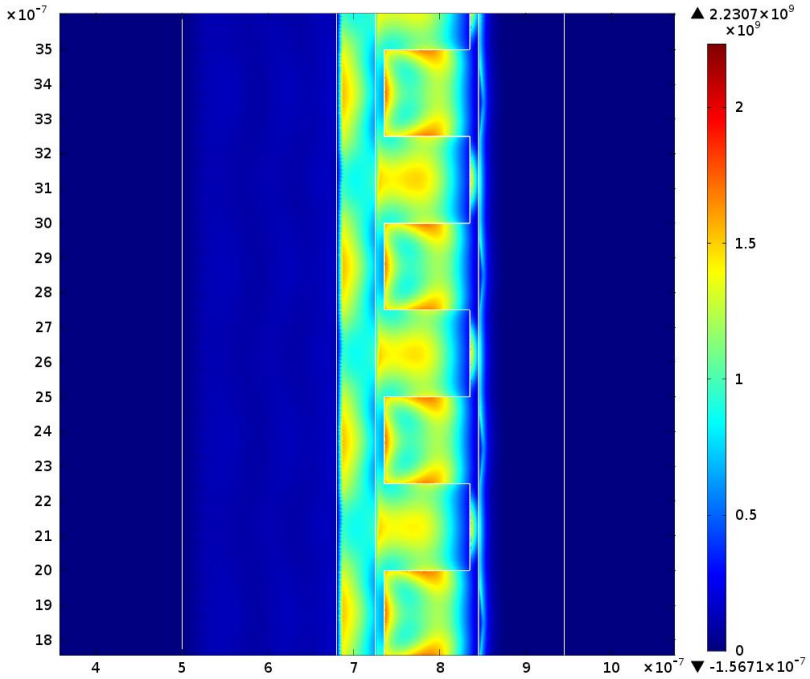

Figure 3.12 *Example of the resulting map for an organic solar cell obtained by summing several light absorption maps for different wavelengths. Units are in W/m^3.*

3.3.2.- ELECTRICAL SIMULATION PROCEDURE

As seen in the previous subsection, the total exciton generation rate can be obtained at every point of the P3HT layer by summing the exciton generation rate corresponding to each wavelength. However, in OSC only those excitons that reach the dissociation interface will contribute to photocurrent, hence it is also necessary to estimate the exciton flux to this interface. After being generated, excitons diffuse around their neighbourhood and eventually dissociate into free charges or recombine following the *exciton diffusion equation*. So the exciton density as a function of time at a position $\vec{r}$ can be set as follows:

UNIVERSITAT ROVIRA I VIRGILI
DESIGN AND MODELLING OF INTERDIGITATED AND NANOSTRUCTURED POLYMER SOLAR CELLS
Pedro Granero Secilla
Dipòsit Legal: T 891-2015

$$\frac{\partial exc}{\partial t} = D_{exc}\frac{\partial exc^2}{\partial \vec{r}^2} + \sum_i \left(\frac{Q(\vec{r};\lambda_i)}{hc/\lambda_i} \right) - \frac{exc}{\tau} \tag{3.5}$$

where $D_{exc} = L^2/\tau$ is the diffusion constant of the excitons, being L and τ the exciton diffusion length and mean lifetime respectively, h the Planck constant, and λ_i the wavelengths of the considered incident plane waves.

The photogenerated current density (J_{PHOTO}) is proportional to the exciton flux at the dissociation interface (J_{EXC}) [Pettersson-1999]:

$$J_{PHOTO} = q\theta J_{EXC} \tag{3.6}$$

where θ is the efficiency of exciton dissociation at the interface and q is the elementary charge. By assuming a 100% efficiency in exciton dissociation and in charge collection, we can obtain the maximum attainable J_{PHOTO}. This magnitude gives a first approximation of the amount of absorbed light that it is actually effective.

To obtain the complete current density–voltage (J–V) characteristics we have used the drift-diffusion model. This model uses the general semiconductor drift-diffusion equations for electrons and holes to describe charge transport [Kirchartz-2008; Barker-2003; Shang-2011]. We assume that the transport properties of the organic materials can be modelled by mobility, density of states (DOS), and doping levels together with a free charge generation and a bimolecular recombination terms.

UNIVERSITAT ROVIRA I VIRGILI
DESIGN AND MODELLING OF INTERDIGITATED AND NANOSTRUCTURED POLYMER SOLAR CELLS
Pedro Granero Secilla
Dipòsit Legal: T 891-2015

The continuity equations for electrons and holes set as follows:

$$\frac{\partial n}{\partial t} = \frac{1}{q}\frac{\partial J_n}{\partial \vec{r}} + G(\vec{r}) - R(\vec{r}), \tag{3.7}$$

$$\frac{\partial p}{\partial t} = -\frac{1}{q}\frac{\partial J_p}{\partial \vec{r}} + G(\vec{r}) - R(\vec{r}). \tag{3.8}$$

In Equations 3.7 and 3.8, the current density expressions for electrons and holes, J_n and J_p respectively, are:

$$J_n = -qn\mu_n \frac{\partial \psi}{\partial \vec{r}} + qD_n \frac{\partial n}{\partial \vec{r}}, \tag{3.9}$$

$$J_p = -qp\mu_p \frac{\partial \psi}{\partial \vec{r}} - qD_p \frac{\partial p}{\partial \vec{r}} \tag{3.10}$$

where *n* and *p* are the electron and the hole densities, *D* the diffusion constant of the free carriers, μ the carriers mobility, and ψ the electrostatic potential.

The free charge generation rate $G(\vec{r})$ is given by the exciton flux able to reach the dissociation interface. Since in OSC excitons only dissociate in the D–A interface, it is in this region were carriers will be generated. We have modelled a very thin generation zone in this interface to model this effect. For the recombination rate $R(\vec{r})$ we have used the bimolecular recombination definition since in OSC it is one of the most crucial charge carrier loss mechanism [Shang-2011]:

$$R(\vec{r}) = \frac{q(\mu_n \mu_p)}{\varepsilon}(np - ni^2) \tag{3.11}$$

where *ni* is the intrinsic carrier density of electrons or holes, and ε is the product of the vacuum permittivity ε_0 and the relative permittivity ε_r of the organic materials. All the parameters have been obtained from the literature [Würfel-2009; Hadziioannou-Malliaras-2007; Wang-2011; Monestier-2007].

Together with the continuity equations, the Poisson's equation also needs to be solved:

$$\frac{\partial^2 \psi}{\partial \vec{r}^{\,2}} = \frac{q}{\varepsilon}(n - p)\,. \tag{3.12}$$

Equations 3.7, 3.8 and 3.12 are solved in an iterative loop (Figure 3.13). To reduce the number of iterations needed to solve the three dependent equations, an initial value for ψ for the Poisson's equation must be supplied:

$$\psi_{init} = \begin{cases} -V_t \log(p_{init}/n_i) - \chi - 0.5E_{gap} & \text{for } N_{doping} < 0 \\ +V_t \log(n_{init}/n_i) - \chi - 0.5E_{gap} & \text{for } N_{doping} \geq 0 \end{cases} \tag{3.13}$$

where V_t is the thermal voltage, n_{init} and p_{init} the charge concentration at the interfaces of the active layer and the electrodes, N_{doping} the doping concentration, χ the electron affinity and E_{gap} the effective band gap between the lowest unoccupied molecular orbital (LUMO) of the acceptor and the highest occupied molecular orbital (HOMO) of the donor. In our case n_{init} and p_{init} are set as follow:

$$n_{init} = \begin{cases} (|N_{doping}|/2 + \sqrt{(N_{doping}^{\ 2}/4 + n_i^{\ 2})}) & \text{for } N_{doping} \geq 0 \\ n_i^{\ 2}/(|N_{doping}|/2 + \sqrt{(N_{doping}^{\ 2}/4 + n_i^{\ 2})}) & \text{for } N_{doping} < 0 \end{cases}, \quad (3.14)$$

$$p_{init} = \begin{cases} (|N_{doping}|/2 + \sqrt{(N_{doping}^{\ 2}/4 + n_i^{\ 2})}) & \text{for } N_{doping} < 0 \\ n_i^{\ 2}/(|N_{doping}|/2 + \sqrt{(N_{doping}^{\ 2}/4 + n_i^{\ 2})}) & \text{for } N_{doping} \geq 0 \end{cases}. \quad (3.15)$$

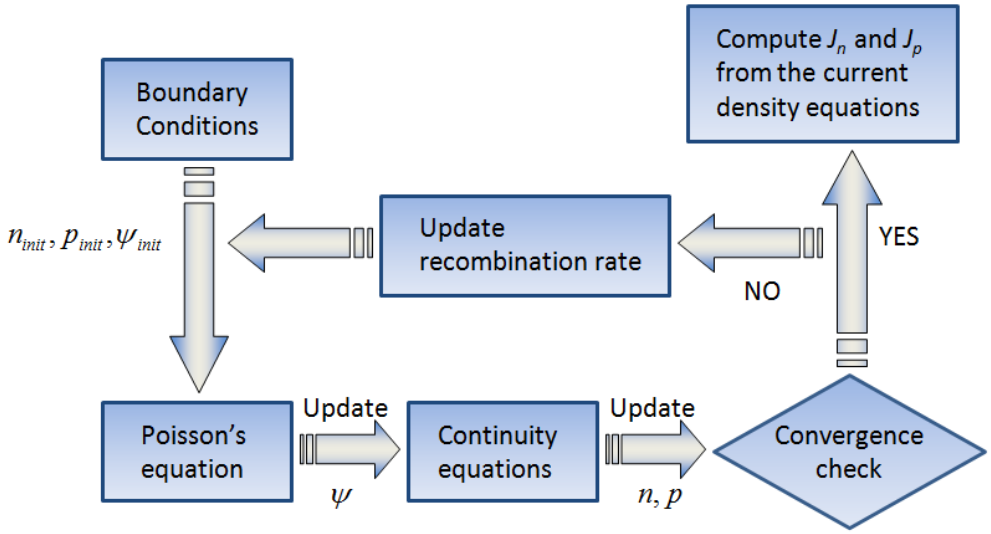

Figure 3.13 *Flow chart of the electrical model simulation process. It starts with an initial value for the potential and the carrier densities. The steady state is obtained by solving the Poisson's and the continuity equations iteratively.*

To obtain a unique solution for this system of equations, it is necessary to specify the carrier densities and the potential at both contacts, i.e., the boundary conditions. The contact at x = 0, where x denotes the position within the device, corresponds to the top contact and the contact at x = *L*, where *L* is the device thickness, corresponds to the bottom contact. The top contact is assumed to line up with the conduction band

UNIVERSITAT ROVIRA I VIRGILI
DESIGN AND MODELLING OF INTERDIGITATED AND NANOSTRUCTURED POLYMER SOLAR CELLS
Pedro Granero Secilla
Dipòsit Legal: T 891-2015

of the semiconductor and is therefore Ohmic. Using Boltzmann statistics, the boundary conditions are set as follows for this contact [Koster-2005]:

$$n(0) = N_c$$
$$p(0) = N_c \exp\left(-\frac{E_{gap}}{V_t}\right) \tag{3.16}$$

where N_c is the effective density of states of both the conduction and valence band. This implies that the contacts are in thermodynamic equilibrium, in contrast to the rest of the device. Since the exact values of the effective densities of states of valence and conduction band are not known and are of little importance, one value for both bands is used [Koster-2005]. Similarly, the bottom contact is assumed to be hole Ohmic, thus:

$$n(L) = N_c \exp\left(-\frac{E_{gap}}{V_t}\right) \tag{3.17}$$
$$p(L) = N_c$$

Finally, in order to obtain the solution of the continuity and the Poisson's equations, the effective band gap (E_{gap}) sets the boundary condition for the electrostatic potential:

$$\psi(0) - \psi(L) = E_{gap}/q - V_a \tag{3.18}$$

where V_a is the applied external voltage.

UNIVERSITAT ROVIRA I VIRGILI
DESIGN AND MODELLING OF INTERDIGITATED AND NANOSTRUCTURED POLYMER SOLAR CELLS
Pedro Granero Secilla
Dipòsit Legal: T 891-2015

3.3.3.- CHARACTERISTIC PARAMETERS OF SOLAR CELLS

The purpose of a solar cell, no matter which technology is behind, is to convert the sunlight radiation in to usable electricity by following the solar energy conversion process. To compare a solar cell with another and determinate which is better, it is necessary to know the amount of electricity that each device can generate for a given illumination, i.e. the efficiency of the cell. This information can be extracted from the characteristic current density–voltage (*J*–*V*) curves of the devices, which are obtained by applying different voltages to a solar cell and by measuring the obtained current density in the output.

Figure 3.14 shows a simple equivalent circuit model for a solar cell. The behaviour of a photovoltaic cell can be approximated by an ideal current source I_{ph} in a parallel association with a diode, which come from the photogenerated current and the pn junction, respectively. In order to describe more precisely the behaviour of a solar cell, two resistances are usually added to the circuit model: the shunt (R_{sh}) and the series (R_s) resistances. R_{sh} and R_s are equivalent resistances in a parallel association and in a series association with the source, respectively. Both resistances reproduce unwanted effects in a device. Hence, ideally, R_{sh} will be an open circuit and R_s will be a short circuit. High values of R_{sh} and low values of R_s will be present in good quality devices.

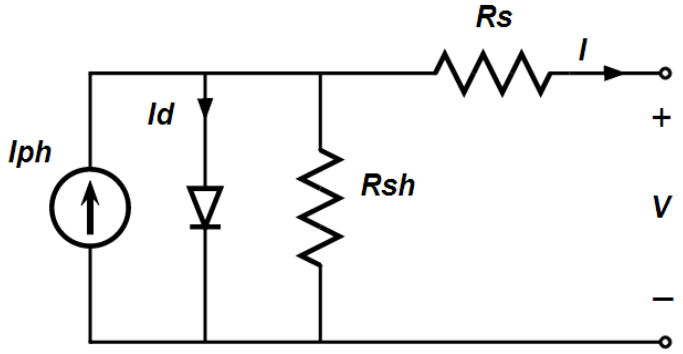

Figure 3.14 *Simplified equivalent circuit model for a solar cell.*

A solar cell works in the quadrant where the voltage is positive and the current is negative. In the ideal model ($R_{sh} = \infty$ and $R_s = 0$), the generated photocurrent density can be expressed as follows:

$$I = I_{ph} - I_0\left[\exp\left(\frac{eV}{kT}\right) - 1\right] \tag{3.19}$$

where *e* is the elementary charge, *k* is the Boltzmann constant, *T* is the temperature expressed in K and I_0 stands for the reverse saturation current.

The experimental current–voltage (*I*–*V*) curves are obtained by exposing a solar cell to a constant light radiation at a constant temperature. Then, while the value of a load resistance (R_L) is varied, the produced photogenerated current is measured. By modifying this load resistance, two important characteristic parameters of the solar cells can be obtained (Figure 3.15):

- **Short circuit current (I_{sc}), or current density (J_{sc}):** It is the generated current, or current density, when the terminals of the cell are in short circuit. In this case, the voltage is zero. The associated R_L is zero.

- **Open circuit voltage (V_{oc}):** It is the voltage for the condition of open circuit, i.e., when the current is zero. This case corresponds to a $R_L = \infty$.

These characteristic parameters can be calculated mathematically by using the equation 3.19 by considering different constraints:

- If V = 0 → I = I_{sc}
- If I = 0 → V = V_{oc}

The open circuit voltage and the short circuit current are related and they can be expressed one as a function of the other with the following expression:

$$V_{oc} = \frac{kT}{e} \cdot ln\left(\frac{I_{sc}}{I_0} + 1\right) \tag{3.20}$$

Apart from these two extreme points of the characteristic *I–V* curves, it also can be obtained the so called maximum power point (P_m). This point determines the operating point that will make that the delivered power to the load resistance will be the highest possible. The corresponding values of current and voltage are I_m and V_m, respectively (Figure 3.15).

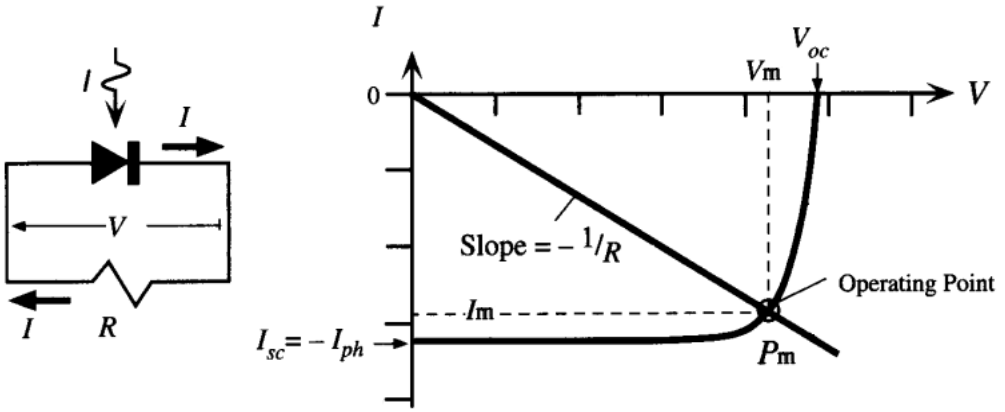

Figure 3.15 *Simplified equivalent circuit model which includes a load resistance (R), and the characteristic I–V curve of a solar cell. In the curve there are depicted several characteristic parameters of the solar cells.*

Another important characteristic parameter of the solar cells that determines its quality is the *Fill Factor* (*FF* < 1). This parameter is defined as follows:

$$FF = \frac{V_m \cdot I_m}{V_{oc} \cdot I_{sc}} \tag{3.21}$$

This parameter is strongly affected by the R_{sh} and the R_s resistances. In an ideal case ($R_{sh} = \infty$ and $R_s = 0$) the *FF* will achieve a value of one, however this will never be the case due to the losses in the real devices. High values of R_{sh} and low values of R_s will make that the *FF* will achieve a value close to unity. *Fill Factors* with a value close to one will indicate that the solar cell is close to be ideal and that the maximum power that will deliver to the load will be higher than for the case of devices with a low *FF*. Finally, the yield of a solar cell to convert the energy received from the solar radiation into electricity can be quantified through the *Power Conversion Efficiency* (*PCE* or η).

UNIVERSITAT ROVIRA I VIRGILI
DESIGN AND MODELLING OF INTERDIGITATED AND NANOSTRUCTURED POLYMER SOLAR CELLS
Pedro Granero Secilla
Dipòsit Legal: T 891-2015

This parameter can be defined as the relation between the maximum power delivered by the cell (P_m) and the power received from the sun (P_{in}):

$$\eta = \frac{P_m}{P_{in}} = \frac{V_{oc} \cdot I_{sc} \cdot FF}{P_{in}} = \frac{V_{oc} \cdot I_{sc} \cdot FF}{A \cdot \Phi_{in}} \tag{3.22}$$

where *A* is the illuminated area and Φ_{in} the incident light intensity in W/area units. The improvement of this efficiency is a key point in the research of the field of photovoltaics that can help to make this energy source at least as profitable as the traditional polluting energy sources.

UNIVERSITAT ROVIRA I VIRGILI
DESIGN AND MODELLING OF INTERDIGITATED AND NANOSTRUCTURED POLYMER SOLAR CELLS
Pedro Granero Secilla
Dipòsit Legal: T 891-2015

CHAPTER 4

ANALYSIS AND OPTIMIZATION OF INTERDIGITATED ORGANIC SOLAR CELLS

4.1.- STUDY OF THE INFLUENCE OF NANOSTRUCTURING IN LIGHT ABSORPTION AND CHARGE CARRIER GENERATION IN INTERDIGITATED OSC

In this section light absorption and charge carrier generation of organic nanostructures are studied by means of finite-element modelling for a wide range of structuring widths, periods and heights for poly(3-hexylthiophene):1-(3-methoxycarbonyl)-propyl-1-phenyl-(6,6)C_{61} (P3HT:PCBM) structures [Granero2-2013]. Since the structuring size range includes values of the order of magnitude of the incident light wavelength, some kind of light trapping and, with this, a possible increase in light absorption with respect to planar equivalent bilayer models can be

expected. It is also possible to await that for particular characteristic dimensions the nanostructure will start to behave like an effective medium. Exciton diffusion has also been studied to evaluate the effective amount of absorbed light contributing to photocurrent. This study can be used to optimize experimental devices, which can be achieved via nanoporous anodic alumina templates. After these theoretical studies, a validation of the simulation method with experimental results, manufactured in our facilities, is presented in section 4.3. Some parameter adjustments are exposed to totally fit the model to the real devices.

4.1.1.- COMPUTATIONAL DOMAIN

To evaluate the influence of the structural features on light absorption and on charge carrier generation in interdigitated BHJ OSC, in this section we have chosen to model only the organic structure in a 2D-computational domain, with size 5x5 μm^2, as shown in Figure 4.1. To avoid unwanted reflections from the light source at the domain boundaries we have used the Scattering Boundary Condition provided by COMSOL RF module. A boundary defined with this condition is transparent for an incoming plane wave [COMSOL RF-2010]. So, it will act as a perfectly absorbing boundary.

The structures under analysis are located to the right of the computational domain. They are 4 µm-width (y-direction) with a variable thickness (x-direction) that ranges from 30 to 100 nm. Such small thickness has been chosen because of two reasons: a) the small exciton diffusion length, and b) the very high absorption coefficient that the organic materials have. Because of a), in thicker layers the produced excitons would be too far from the dissociation interface. On the other hand, because of b), thinner layers would make the nanostructuring effects nearly negligible.

UNIVERSITAT ROVIRA I VIRGILI
DESIGN AND MODELLING OF INTERDIGITATED AND NANOSTRUCTURED POLYMER SOLAR CELLS
Pedro Granero Secilla
Dipòsit Legal: T 891-2015

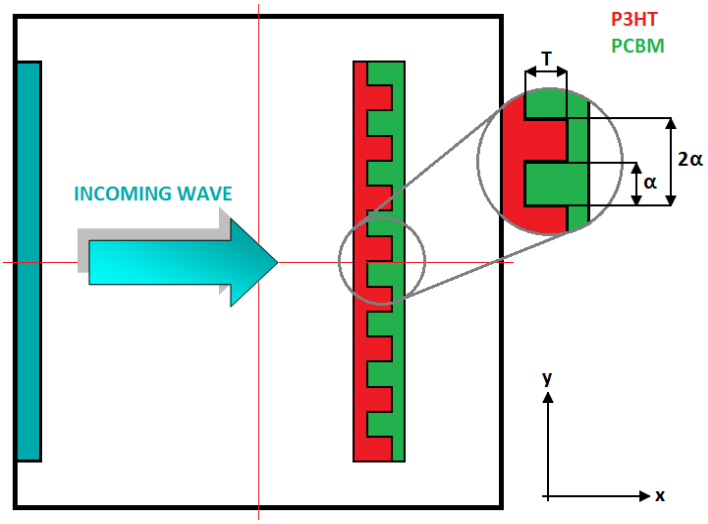

Figure 4.1 *Diagram, not to scale, of the computational domain used in simulations displaying the light source and the cell under study positions. It also shows the geometrical features of the nanostructuring and the coordinate system.*

Model cells are composed of three layers. The first layer (left), onto which light is incoming, is composed of poly(3-hexylthiophene) (P3HT) and has a thickness of 10 nm. The second layer (middle) corresponds to the nanostructured region, consisting of alternating blocks of P3HT and PCBM with α width and height *T*. Consequently, as it is indicated in Figure 4.1, the period is 2α. Finally, the third layer (right) is composed of 1-(3-methoxycarbonyl)-propyl-1-phenyl-(6,6)C_{61} (PCBM) an also has a thickness of 10 nm.

The parameter α has been varied in a range of values from 1.25 to 2000 nm (see Table 4.1). Only those values of α that allow an integer number of blocks of each material have been considered. In this way, since both P3HT and PCBM blocks are identical in size, there will be the same amount of each organic semiconductor and the same 1:1 proportion for all α. Thus any differences in the absorption properties can be

attributed to nanostructuring. The parameter *T* takes the values of 10, 20, 40 and 80 nm. From here this parameter will be indicated as the geometrical ratio to the fix 10 nm-thick planar layer, becoming the selected values 1:1, 1:2, 1:4 and 1:8. The results of the nanostructured materials will be compared with that of a reference that consists of a planar bilayer structure with the same amount of each organic material as the nanostructured devices for each geometrical ratio. This structure consists of two layers, being the first (left) of P3HT and the second (right) of PCBM.

In our case we have modelled the optical features of the involved materials by using the refractive index (*n*) and the extinction coefficient (*k*) of the complex index of refraction ($\tilde{n} = n + ik$) obtained from Ref. [Defranoux-2010].

α (nm)	***Period (2α) (nm)***	***α (nm)***	***Period (2α) (nm)***
1.25	*2.5*	*80*	*160*
2.5	*5*	*100*	*200*
5	*10*	*125*	*250*
10	*20*	*200*	*400*
12.5	*25*	*250*	*500*
20	*40*	*400*	*800*
25	*50*	*500*	*1000*
40	*80*	*1000*	*2000*
50	*100*	*2000*	*4000*
62.5	*125*		

Table 4.1 *List of the used nanostructuring sizes, width (α) and periodicity (2α).*

UNIVERSITAT ROVIRA I VIRGILI
DESIGN AND MODELLING OF INTERDIGITATED AND NANOSTRUCTURED POLYMER SOLAR CELLS
Pedro Granero Secilla
Dipòsit Legal: T 891-2015

The light source has been modelled with the *Scattering Boundary Condition* since it can also be used to simulate an incoming wave from an outer boundary of the domain. This light source is placed to the left of the computational domain and it emits a right-propagating monochromatic linear polarized wave, with Ex = Ey = 0, and Ez ≠ 0. The wavefront is planar and 4-μm width. In order to obtain the absorption spectrum, simulations for wavelengths in the range from 250 to 650 nm in intervals of 5 nm have been carried out. We have chosen this wavelength range because it corresponds to the absorption range of P3HT.

4.1.2.- LIGHT ABSORPTION STUDY

Figure 4.2 shows the relative light absorption in the P3HT material of the nanostructured devices if compared with that of the reference planar bilayer structure ($Q(\lambda)/Q^{Ref}(\lambda)$) as a function of wavelength (λ) for a geometrical ratio of 1:2. Our results can be divided into four groups, each one corresponding to one of the different behaviours that we have observed as a function of α. Figure 4.2A corresponds to the range of α from 1.25 to 12.5 nm. It can be observed that for wavelengths above 375 nm there is an important increase in the absorption if compared with the reference cell. However, for short λ there is a decrease instead. This is in agreement with other studies that also have reported this same behaviour in light absorption spectra [Kim-2010; Van Dijken-2011; He-2011]. From Figure 4.2A it can be also observed that all the curves follow the same behaviour showing very little differences between them. This fact suggests that the nanostructured region of these cells behaves as an effective medium, given the very small values of α if compared with λ.

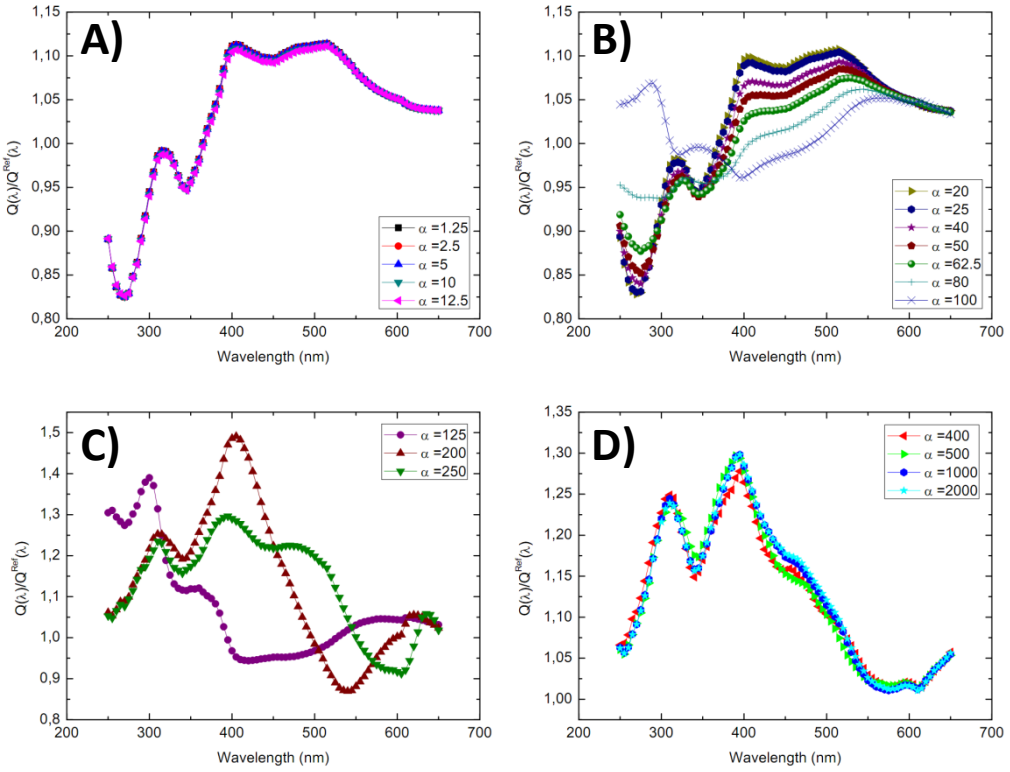

Figure 4.2 *Relative light absorption in the P3HT material of the nanostructures if compared with that of the reference planar bilayer device ($Q(\lambda)/Q^{Ref}(\lambda)$) as a function of wavelength for* α *from 1.25 to 12.5 nm (A), 20–100 nm (B), 125–250 nm (C), and 400–2000 nm (D) for a geometrical ratio of 1:2.*

To check the validity of this hypothesis, we show in Figure 4.3 the absorption maps (total power dissipation density in W/m^3) of the nanostructures for different values of α and for λ = 450 nm. Figure 4.3A corresponds to a structure where the nanostructured layer has been replaced by a homogeneous layer simulating an effective medium. The optical constants (*n* and *k*) of this middle layer have been obtained as an average of the P3HT and the PCBM optical constants. Figure 4.3B corresponds to α = 1.25 nm. In this case, materials boundaries are not displayed for a better comparison. Finally, the structure in Figure 4.3C corresponds to α = 12.5 nm. It

UNIVERSITAT ROVIRA I VIRGILI
DESIGN AND MODELLING OF INTERDIGITATED AND NANOSTRUCTURED POLYMER SOLAR CELLS
Pedro Granero Secilla
Dipòsit Legal: T 891-2015

can be seen that the absorption maps show the same distribution in the three cases, which indicates that for such a fine nanostructuring the central layer behaves as an effective medium.

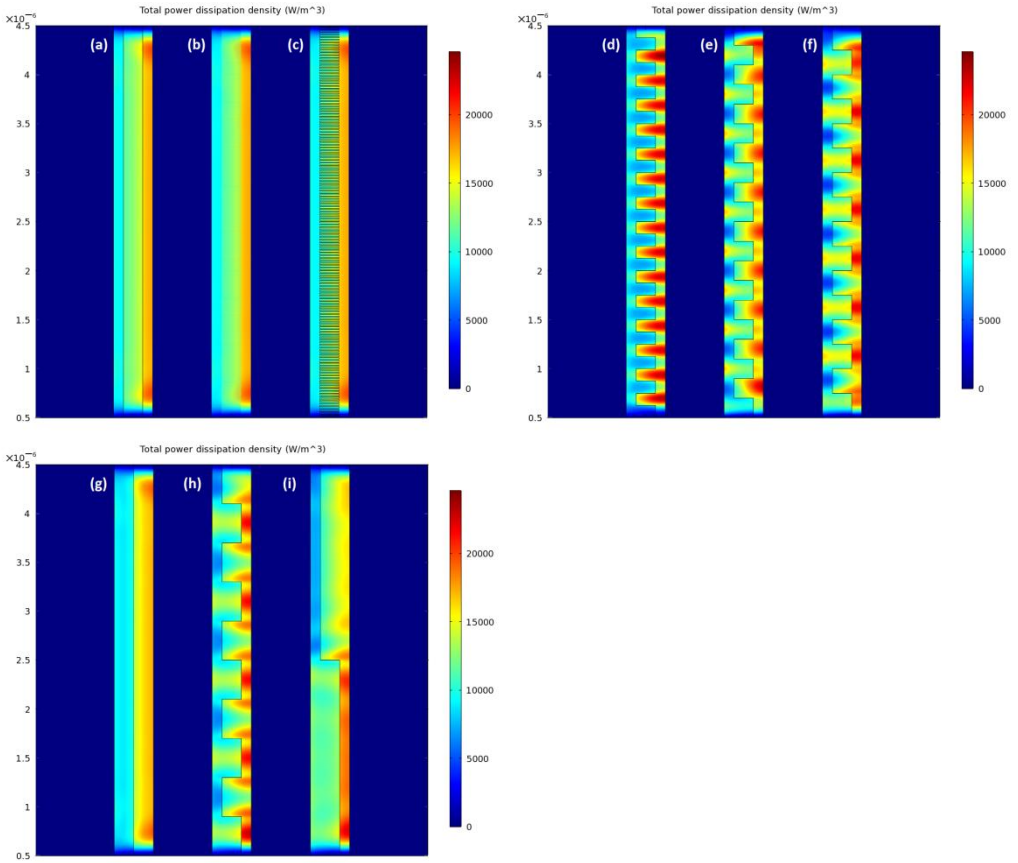

Figure 4.3 *Absorption maps for λ = 450 nm for the cell which nanostructured region is an effective medium (A), α = 1.25 nm (B), α = 12.5 nm (C), α = 125 nm (D), α = 200 nm (E), α = 250 nm (F), the planar bilayer reference cell (G), α = 400 nm (H) and α = 2000 nm (I) for a geometrical ratio of 1:2. Units are in W/m^3 for the power dissipation and in m for the geometry. For α = 1.25 nm the boundaries of the nanostructuring are not displayed for a better comparison with the effective medium reference cell.*

UNIVERSITAT ROVIRA I VIRGILI
DESIGN AND MODELLING OF INTERDIGITATED AND NANOSTRUCTURED POLYMER SOLAR CELLS
Pedro Granero Secilla
Dipòsit Legal: T 891-2015

The results for α between 20 and 100 nm are shown in Figure 4.2B. For increasing α, the behaviour of $Q(\lambda)/Q^{Ref}(\lambda)$ begins to differ from that of an effective medium. The absorption of the nanostructured cell for λ between 375 and 600 nm decreases with increasing α and it can even be lower than for the planar bilayer structure at certain wavelengths for the highest values of α. Instead, the trend is the opposite for wavelengths below 325 nm, with an especially important increase when α is 80 or 100 nm. This change in the behaviour can be explained by the fact that the nanostructured layer does not longer behave as an effective medium and effects related to the size of the nanostructuring begin to take place. Furthermore, these results are in agreement with previously reported experimental work. Kim *et al.* [Kim-2010] reported an enhancement in absorption in the range of 450–600 nm and a decrease for short wavelengths. Their cells had a 50 nm-width and 100 nm periodicity nanostructuring. However, Wiedemann *et al.* [Wiedemann-2010] did not find any significant differences between nanostructured (α = 40 nm) and bilayer films. Nevertheless, they did not report complete information concerning to light absorption.

The graph of Figure 4.2C shows the relative absorption of the P3HT layer for α = 125, 200 and 250 nm. For α = 125 nm the behaviour of the cell follows the same trend as with Figure 4.2B: $Q(\lambda)/Q^{Ref}(\lambda)$ decreases for long wavelengths and it increases for short ones if compared with smaller nanostructuring geometries. For α = 200 nm, we can observe a trend that differs from the previous ones. In this case the increase in light absorption for short wavelengths is less pronounced. However, the increase near 400 nm is close to 50%, the greatest obtained value. Another important difference for α = 200 nm is the decrease of $Q(\lambda)/Q^{Ref}(\lambda)$ at long wavelengths, which becomes lower than unity in the *λ* range from 500 to 600 nm. Finally, for α = 250 nm we can observe another behaviour. As for α = 200 nm, there is a maximum of absorption at λ = 400 nm but now is less pronounced, and the decrease from this maximum is slower with a

UNIVERSITAT ROVIRA I VIRGILI
DESIGN AND MODELLING OF INTERDIGITATED AND NANOSTRUCTURED POLYMER SOLAR CELLS
Pedro Granero Secilla
Dipòsit Legal: T 891-2015

plateau around 475 nm. For α = 250 nm a range with relative absorption below unity is also present although it is red-shifted with respect the case of α = 200 nm. The behaviour observed in this graph indicates that a nanostructuring with a period (2α) in the range of λ influences critically the light absorption properties. The nanostructured layer behaves like a subwavelength diffraction grating that contributes to trap the normally incident light in the plane of the structures. Depending on α and on the wavelength, the incident light can be concentrated in a proper region of the P3HT layer with this grating effect, leading to an increase in absorption. This can be seen in Figures 4.3E, e and F, where the absorption maps of the three structures for λ = 450 nm are shown. For α = 125 nm, the highest light absorption takes place in the thinner regions of the P3HT layer, while for the other two structures absorption is concentrated in the thicker parts. Thus, we can expect a higher amount of absorbed light for these two α values.

Finally, the results for α between 400 and 2000 nm are shown in Figure 4.2D. As in the case of the first group of values of α, the curves are very similar between them. Little differences can only be observed at the maximum of λ = 400 nm and at wavelengths close to 450 nm. The highest relative absorption is achieved for α = 2000 nm. For this group of sizes, it is also remarkable that the relative absorption is always above unity. The absorption maps for the reference cell (Figure 4.3G), α = 400 nm (Figure. 4.3H), and α = 2000 nm (Figure 4.3I) can help us to explain these results. The absorption in the P3HT structures is not uniform as it shows regions with higher absorption than the reference structure while others with lower absorption. These variations indicate that the device is acting as a diffraction grating, although not a subwavelength one. Thus, even though there exist some propagative modes that are transmitted, there are still modes that become coupled to the structure and absorbed efficiently.

Although these results are very promising, we should keep in mind that not all the absorbed light will be actually profitable. Figure 4.4 shows the $Q_{Total}/Q_{Total}^{Ref}$ of the total absorbed power as a function of α for the different geometrical ratios. All the curves follow the same trend but at different levels. It can be observed that the best total absorptions are achieved for high α values, with a local maximum at around α = 250 nm. Instead, for small α values the absorption is constant and begins to decrease for α above 10 nm, reaching a local minimum at around α = 100 nm. As it can be expected, for the shallower structures (ratio 1:1) the relative absorbed light is close to unity for all α. Then, as the structure height increases, there is an increase in the relative absorbed light up to the ratio 1:4. However, for a ratio of 1:8, there is an important decrease in $Q_{Total}/Q_{Total}^{Ref}$ for all the structures sizes instead.

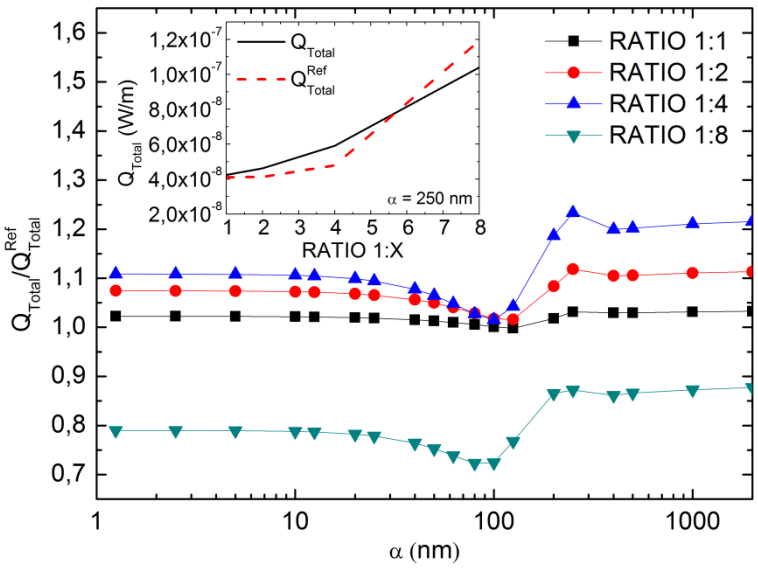

Figure 4.4 *Relative light absorption in the P3HT layer of the nanostructures, if compared with that of the reference planar bilayer device, as a function of α for the different geometrical ratios considering the complete P3HT layer. The inset shows the total absorbed light for the nanostructures (Q_{Total}) and for the equivalent planar bilayer reference (Q_{Total}^{Ref}) as a function of the geometrical ratio for α = 250 nm.*

UNIVERSITAT ROVIRA I VIRGILI
DESIGN AND MODELLING OF INTERDIGITATED AND NANOSTRUCTURED POLYMER SOLAR CELLS
Pedro Granero Secilla
Dipòsit Legal: T 891-2015

So, we have that if the structure height *T* is too short, the structure still behaves like the planar architecture and there is no significant increase in light absorption. On the other hand, if *T* is too high, the total absorbed light will be lower than the one of the planar equivalent reference. This can be explained by examining separately the total absorbed light for the ordered bulk heterojunction and for the equivalent planar bilayer reference, at a given α, as it is plotted in the inset of Figure 4.4 for α = 250 nm. In all cases, the total absorbed light increases with increasing amount of P3HT. However, the light trapping effect of the structured cells allows absorbing more light in the P3HT, provided its height does not exceed a given value corresponding to the intersection of the curves in the inset of Figure 4.4.

4.1.3.- EXCITON DIFFUSION AND MAXIMUM ATTAINABLE PHOTOGENERATED CURRENT DENSITY

Figure 4.5 depicts the maximum attainable photogenerated current density (J_{PHOTO}) of the nanostructured devices as a function of α for the different geometrical ratios. All the curves follow approximately the same trend: maximum currents are achieved for the smallest α, with a decrease with increasing α and a slight recover at α = 250 nm. However, as the geometrical ratio increases the relative J_{PHOTO} also increases, achieving a maximum for a structure height of 80 nm, despite having this value the lowest relative absorbed light. The dependence of J_{PHOTO} with the geometrical ratio is different for the smaller α than for the bigger. This is illustrated in the inset of Figure 4.5, where the J_{PHOTO} as a function of the geometrical ratio is presented. For small a J_{PHOTO} increases with increasing structure height, while this trend is inverted for big α. The graph includes also the J_{PHOTO} of the corresponding reference planar cells, which is in all cases smaller than for the nanostructured cells and decreases as the thickness increases.

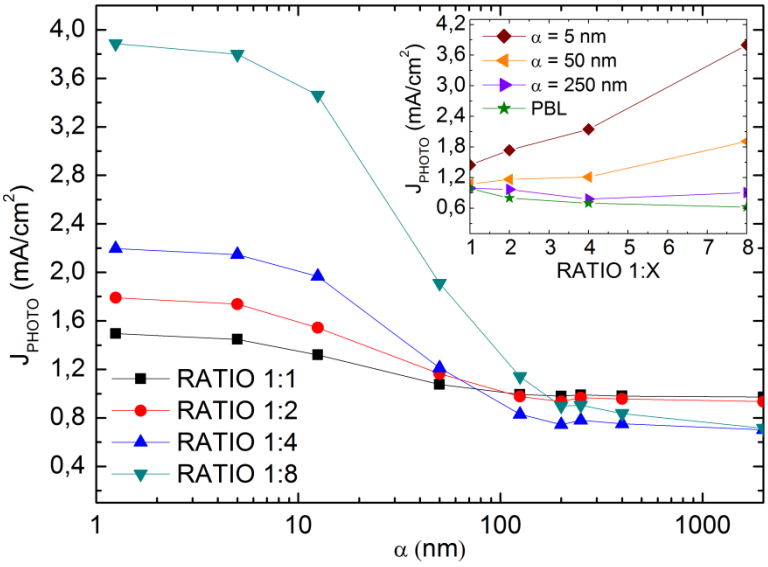

Figure 4.5 *Maximum attainable photogenerated current density (J_{PHOTO}) of the nanostructured devices as a function of* α *for the different geometrical ratios. The inset shows J_{PHOTO} for the nanostructures and for the equivalent planar bilayer reference (PBL) as a function of the geometrical ratio for several* α*.*

Thus, for devices with big values of α many of the extra absorbed light does not contribute to charge generation. On the other hand, although for small α values the increase in light absorption is more modest, nearly all the P3HT layer will be close enough to the dissociation interface and more of the generated excitons will produce free charge carriers. A higher geometrical ratio will also give better results in terms of relative J_{PHOTO} since the planar equivalent structures will be too thick for an efficient exciton dissociation. With an optimal geometry, this increment in the relative photocurrent can be more than a factor 6. The observed improvement in the behaviour of the devices with the nanostructuring of the interface can be attributed to two factors: i) the light trapping from the nanostructuring, and ii) the extended dissociation interface of nanostructured cells if compared with the planar bilayer

UNIVERSITAT ROVIRA I VIRGILI
DESIGN AND MODELLING OF INTERDIGITATED AND NANOSTRUCTURED POLYMER SOLAR CELLS
Pedro Granero Secilla
Dipòsit Legal: T 891-2015

device. From our results, it is clear that the second factor is much more determinant since light trapping only can be noticed in the relative maximum around α = 250 nm.

4.2.- STUDY OF THE INFLUENCE OF NANOSTRUCTURING IN THE EFFICIENCY OF INTERDIGITATED OSC

In this section we analyze the influence of the nanostructured dissociation interface geometry on the overall efficiency of interdigitated heterojunction full organic solar cells (OSC). A systematic analysis of light absorption, exciton diffusion, and carrier transport, all in the same numerical framework, is carried out to obtain their dependence on the interface geometrical parameters: pillar diameter and height, and nanostructure period. Cells are constituted of poly(3-hexylthiophene) (P3HT) and 1-(3-methoxycarbonyl)-propyl-1-phenyl-(6,6)C_{61} (PCBM) [Granero-2013]. Unlike in the previous section, which focused on the behaviour of only the organic semiconductors, in this case we aim at modelling the complete devices since the different layers and the electrodes directly affect the cells' efficiency. It is possible that this study results will reveal similar conclusions than in the previous one, since the short exciton diffusion length of organic materials is a strong limitation in this kind of cells. However, charge transport must be take into account to obtain accurate results that can be compared to experimental data.

4.2.1.- COMPUTATIONAL DOMAIN

Since in this section we are going to compute the overall efficiency of OSC, it is not enough to only consider the organic part of the devices as previously. Here, our model is a 2D simplification of a complete real 3D device. It consists of a structure of

ITO, poly(3,4-ethylenedioxythio-phene) poly(styrenesulfonate) (PEDOT:PSS), P3HT, PCBM, and a back contact of aluminium (Al) as it is shown in Figure 4.6. This simplification implies that the cell is nanostructured in the form of interpenetrating P3HT and PCBM grooves. The ITO, PEDOT:PSS, and Al thicknesses are fixed while the variables are the P3HT groove width α, (equivalent to the nanopillar diameter in a 3D nanostructure), the period β (equivalent in 3D to the interpillar distance), the ratio of the groove width to the period (γ = α/β), and the nanopillar height including the fix base layer (*T*). In our case, β ranges from 25 nm to 4000 nm, γ takes the values of 0.25, 0.50, and 0.75, and *T* is in the range from 30 to 250 nm in intervals of 10 nm with an additional value of 500 nm. The optical properties of the materials have been modelled by using the refractive index (*n*) and the extinction coefficient (*k*) of the complex index of refraction ($\tilde{n} = n + ik$), which have been obtained from the literature [Defranoux-2010; Synowicki-1998; Pettersson-2002; Rakic-1995]. As reference, the results are compared with an equivalent planar bilayer cell with the same amount of the different materials for each case.

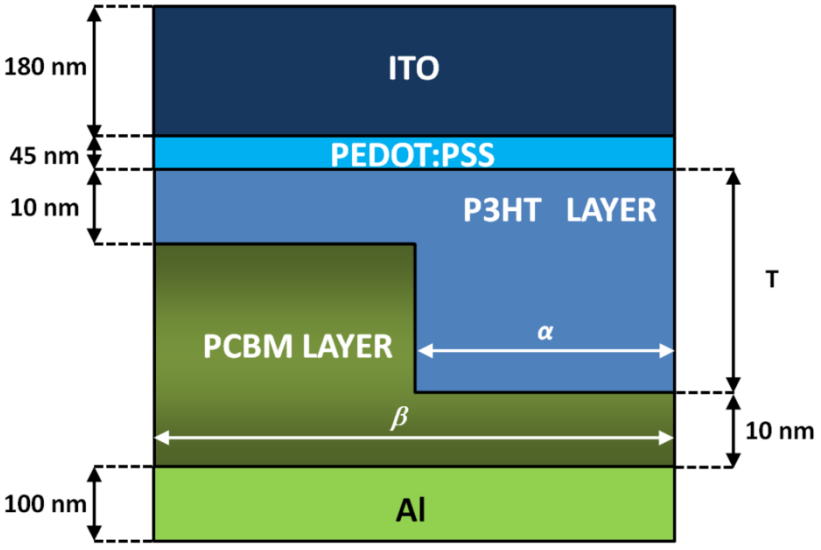

Figure 4.6 *Schematic unit cell model of the structure ITO/PEDOT:PSS/P3HT/PCBM/Al showing the fixed parameters and the variables under study.*

UNIVERSITAT ROVIRA I VIRGILI
DESIGN AND MODELLING OF INTERDIGITATED AND NANOSTRUCTURED POLYMER SOLAR CELLS
Pedro Granero Secilla
Dipòsit Legal: T 891-2015

The incident light is assumed to be normal to the surface of the devices and incident from the ITO side. It has been modelled as the superposition of a set of monochromatic linear polarized waves with a planar wavefront, and with a direction that is parallel to the nanopillars. The amplitudes of these plane waves follow the standard AM1.5 spectral distribution of the solar radiation. To obtain the complete spectrum, simulations have been carried out for wavelengths in the range from 280 to 650 nm in intervals of 10 nm. We have chosen this wavelength range because it corresponds to the absorption spectrum of P3HT, the material where most of the excitons will be generated.

4.2.2.- LIGHT ABSORPTION STUDY

Figure 4.7 shows the total absorbed light power (Q_{Total}) in the P3HT layer as a function of the period β for $\gamma = \alpha/\beta = 0.5$. All the curves show a similar behaviour with two local maxima for *T* around 80 nm and 230 nm. A local minimum for *T* close to 130 nm is also present in all cases. The maximum absorption is achieved for β = 25 and 4000 nm while the lower absorption is clear for β = 250 nm. Since it can be expected that a higher light absorption will lead to a higher photocurrent, at least for small periods (β), we focus the following electrical calculations on *T* = 80 nm and on *T* = 230 nm as it will be showed in the next section.

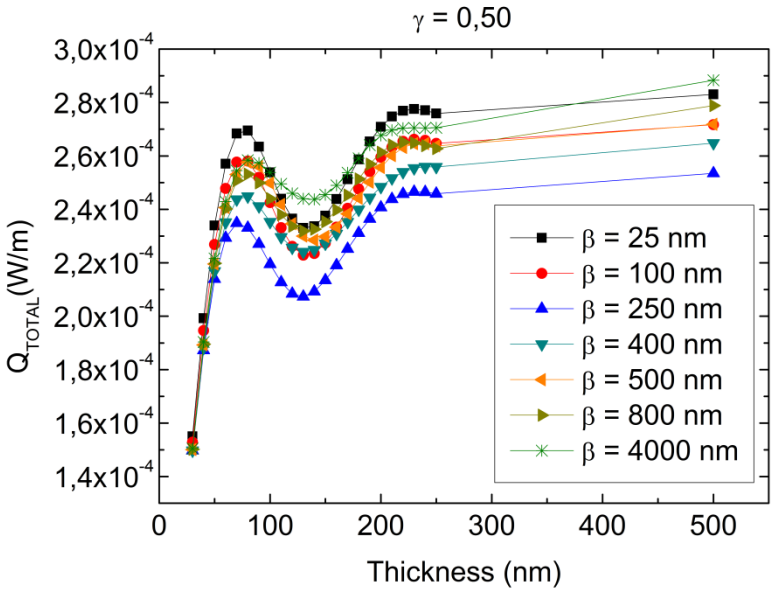

Figure 4.7 *Total absorbed light power (Q_{Total}) in the P3HT layer as a function of the period* β *for* $\gamma = \alpha/\beta = 0.5$.

4.2.3.- ELECTRICAL STUDY

Figure 4.8 shows the obtained J_{PHOTO} as a function of β, for the two considered thicknesses, for the interdigitated devices. The J_{PHOTO} for equivalent planar bilayer cells (planar BL, cells with the same amount of P3HT and PCBM than the interdigitated ones but in planar configuration) are indicated as horizontal lines for reference. For all the range of considered β, except for β = 25 nm, J_{PHOTO} for T = 80 nm is bigger than for T = 230 nm, even though T = 230 nm corresponds to the highest light absorption. We can also observe that as β increases the difference between J_{PHOTO} for T = 80 and for T = 230 nm also increases. This fact can be explained by the short exciton diffusion length of organic materials.

UNIVERSITAT ROVIRA I VIRGILI
DESIGN AND MODELLING OF INTERDIGITATED AND NANOSTRUCTURED POLYMER SOLAR CELLS
Pedro Granero Secilla
Dipòsit Legal: T 891-2015

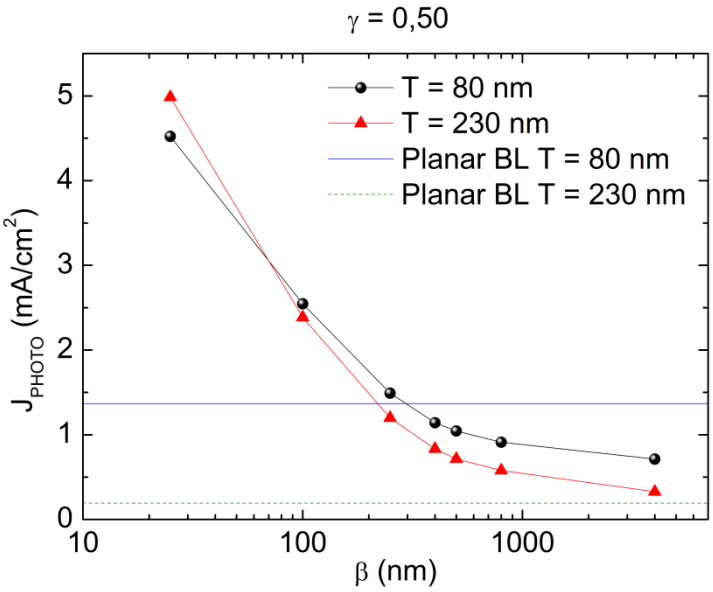

Figure 4.8 *Maximum attainable photogenerated current density (J_{PHOTO}) as a function of β for the two pillar heights at which the absorbed light is maximum, T = 80 nm and T = 230 nm, and for γ = 0.50. The horizontal lines correspond to the J_{PHOTO} of the equivalent planar bilayer cells.*

To this end, Figure 4.9 depicts the steady state exciton concentration map of an interdigitated cell for α = 250 nm, β = 500 nm, and *T* = 250 nm (A), and of its equivalent planar bilayer form (B). It can be seen that in the interdigitated cell excitons reach up to a certain depth in the P3HT, limited by the exciton diffusion length. In the planar equivalent cell, this limitation results in a low concentration gradient of excitons near the Donor–Acceptor interface, which leads to the low J_{PHOTO} observed. This argument supports the results that can be observed in Figure 4.8, where an improvement in J_{PHOTO} with respect to the bilayer cell can be observed only for β below 100 nm. Also it can be seen that the exciton concentration gradient is higher over the nanopillars lateral walls than over the remaining interfaces. This further examination of the concentration map in Figure 4.9A explains also why J_{PHOTO}

UNIVERSITAT ROVIRA I VIRGILI
DESIGN AND MODELLING OF INTERDIGITATED AND NANOSTRUCTURED POLYMER SOLAR CELLS
Pedro Granero Secilla
Dipòsit Legal: T 891-2015

decreases with increasing β: as the width of the pillar becomes bigger, less excitons are generated close to the lateral interface, where most of them dissociate.

Figure 4.10 shows the complete current density–voltage (*J*–*V*) curves for several β with γ = 0.5, and for the reference planar bilayer cell for the two thicknesses of interest (*T* = 80 and 230 nm). In this graph, we can see that the open circuit voltage (V_{oc}) of the different devices is in a range from 0.5 to 0.6V. Another important parameter of solar cells, the short circuit current density (J_{sc}), shows a higher variation between cells, ranging from 0.25 to more than 4.5mA/cm^2. These values of J_{sc} show a good correlation with the J_{PHOTO} displayed in Figure 4.8, especially for *T* = 80 nm. This indicates a high charge carrier collection efficiency and that this process is not strongly influenced by the geometrical characteristics of the interdigitated interface.

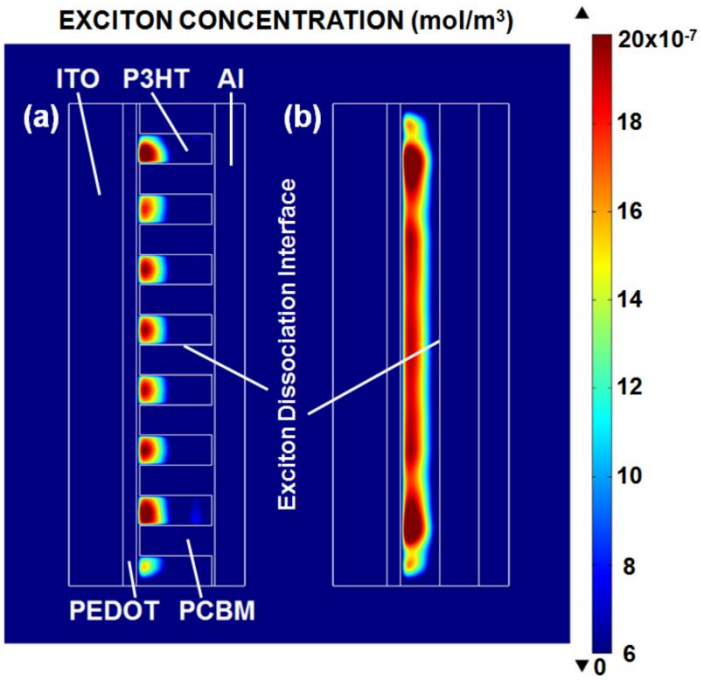

Figure 4.9 *Exciton concentration map of an interdigitated cell for* β *= 500 nm,* γ *= 0.50, and T = 250 nm (A), and of its equivalent bilayer form (B).*

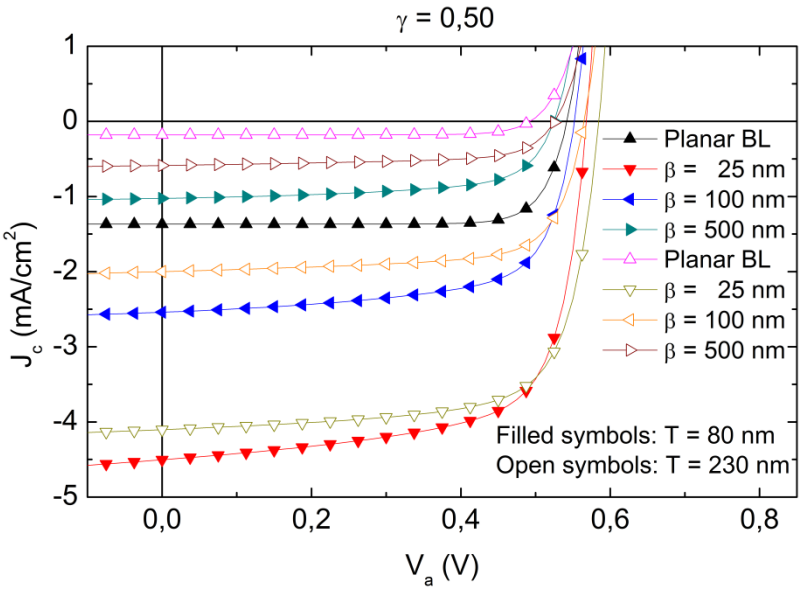

Figure 4.10 *Current density–voltage (J–V) curves for several* β *with a fix* γ *= 0.50. The J–V curves of the reference planar bilayer cells for the two thicknesses of interest (T = 80 and 230 nm) have also been included.*

Figure 4.11 shows the *J–V* characteristics for *T* = 80 nm for several β and for different γ = α/β. As in Figure 4.10, the V_{oc} for the different cells ranges from 0.5 to 0.6V while the J_{sc} values are distributed over a wider range and show a different trend for different β. For β = 25 nm, when γ increases J_{sc} increases in a similar proportion. However, for bigger β, the increase of J_{sc} with γ is less noticeable. A higher γ implies a higher ratio of P3HT, and therefore, more absorbed light. However, not in all cases, all this supplementary amount of absorbed light will be actually effective because of the short exciton diffusion length of P3HT.

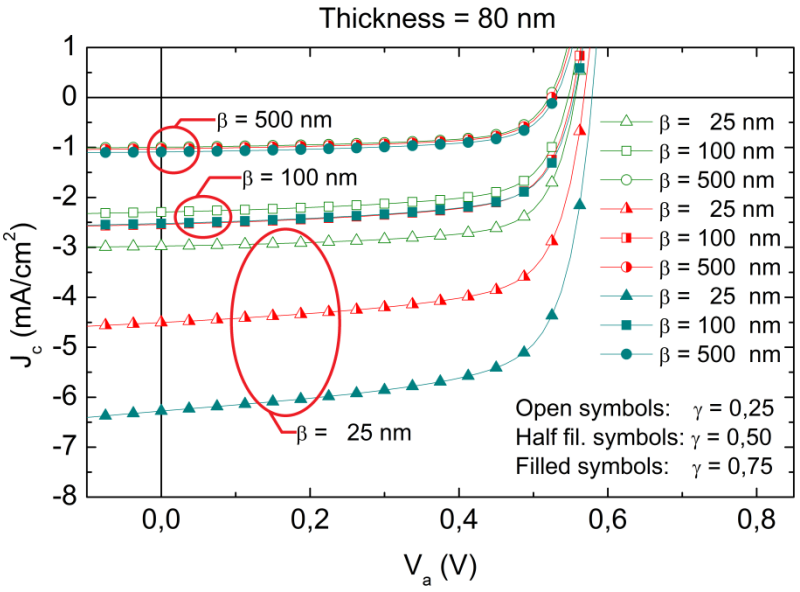

Figure 4.11 *J–V curves for T = 80 nm for several* β *and for different* γ = α/β.

From the *J–V* characteristics, we have also obtained the *Fill Factor* (*FF*), which is shown in Figure 4.12 as a function of γ = α/β for *T* = 80 nm and several β. We can see that while for β = 25 nm the *FF* decreases when γ increases, there are no significant changes for the rest of β when γ varies. If we compare the *FF* between the different β, we can observe that it decreases as the period of the nanostructures increases. This parameter is one of the most representing factors in the performance of a solar cell since it gives information on the charge transport and recombination mechanisms. The analysis of this parameter reveals that, in the case of study, the exciton diffusion is a more limiting factor than the charge transport, since when the exciton dissociation starts becoming a limitation (large β and γ) the *FF* decreases. These results are in good agreement with our previous interpretations from the analysis of the J_{PHOTO} as a function of the geometrical parameters.

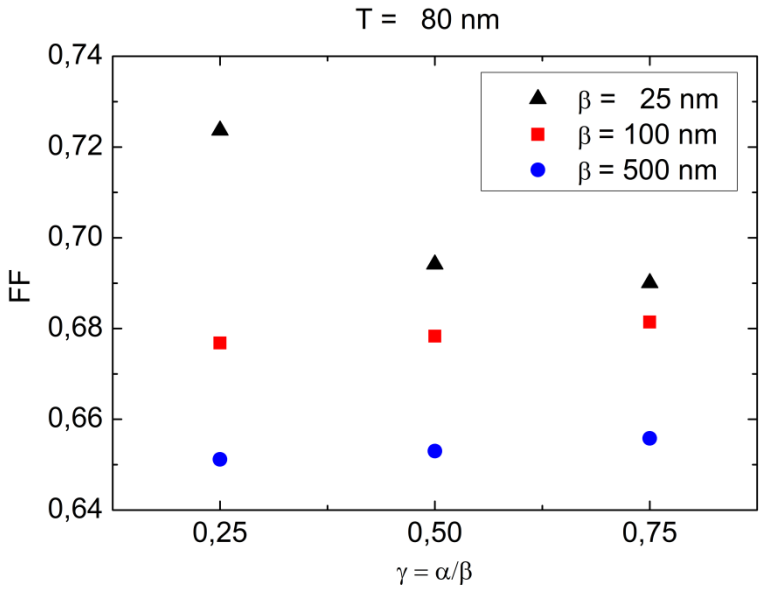

Figure 4.12 *Fill Factor (FF) as a function of* $\gamma = \alpha/\beta$ *for T = 80 nm and several* β.

Table 4.2 shows the efficiency (η) corresponding to the devices referred to in the previous figures. We can observe that a bigger quantity of donor polymer does not always mean better results. Efficiencies are higher for T = 80 than for T = 230 nm for the same γ, and a higher γ only represents a noticeable increase in the efficiency for β = 25 nm. The increase in β causes a decrease in the efficiency leading to for β as big as β = 500 nm, the interdigitated cell efficiencies are lower than that of the equivalent planar bilayer. The maximum efficiency is achieved for β = 25 nm, T = 80 nm, and γ = 0.75, with an efficiency 3.6 times higher than the best planar bilayer reference device. This optimal planar cell is the equivalent, in amount of each organic material, for an interdigitated cell of T = 60 nm and γ = 0.50 and presents an efficiency of 0.69%.

CELLS EFFICIENCY (%)				
	T = 80 nm, γ = 0.25	***T = 80 nm, γ = 0.50***	***T = 230 nm, γ = 0.50***	***T = 80 nm, γ = 0.75***
β = 25 nm	*1,18*	*1,76*	*1.72*	*2,49*
β = 100 nm	*0,85*	*0,95*	*0.81*	*0,95*
β = 500 nm	*0,34*	*0,35*	*0,21*	*0,38*
BEST PLANAR BILAYER REFERENCE CELL (T = 60 nm): *0,69*				

Table 4.2 *Efficiencies of representative cells obtained from the J–V curves from Figures 4.10 and 4.11. These values should be compared with the maximum efficiency that has been obtained with a planar bilayer reference cell, which is η = 0.69%.*

The results of our work show a good agreement with previous reported studies. Yang and Forrest [Yang-2008] reported that the absorption by the organic layers limits the optimal cell thicknesses to between 200 and 300 nm, a range that includes one of our optimized nanopillar height. They also achieved the highest external quantum efficiencies with an interdigitated network when the domain size was equal to or smaller than the exciton diffusion length. Meng *et al.* [Meng-2010] found that the optimal energy conversion efficiency can be achieved when the feature size is around 10 nm, a value close to its exciton diffusion length. In the study of Kim *et al.*, [Kim-2011] they state that for a sufficient light absorption the active layer thickness should be greater than the 50% of the photon mean free path, which is the inverse of the absorption coefficient (~100 nm for organic materials [Würfel-2009]). However, as in our results, extremely high pillars for a complete light absorption do not give the highest efficiencies.

UNIVERSITAT ROVIRA I VIRGILI
DESIGN AND MODELLING OF INTERDIGITATED AND NANOSTRUCTURED POLYMER SOLAR CELLS
Pedro Granero Secilla
Dipòsit Legal: T 891-2015

The results of our study are also in good agreement with reported experimental work of several authors. Kim *et al.* [Kim-2010] reported an increase of 6.6 times in the efficiency of P3HT-C60 interdigitated devices if compared with a planar bilayer reference cell. Although this improvement factor is bigger than the one we obtain, they do not report details about their reference device. He *et al.* [He-2011] increased the efficiency 2.4 times with cells of 25 x 25 nm of nanorod size, 80 nm of nanorod height, and 50 nm of structure period, also in good agreement with our results. Furthermore, these authors also consider a wide range of nanorod sizes and they find the same trend for the J_{sc} and the efficiency as we do. Other experimental reported works also show a good correlation with our study such as Zheng *et al.* [Zheng-2009] with two-fold efficiency increase in 20 nm diameter and 40 nm long nanopillars, and Wiedemann *et al.* [Wiedemann-2010] with an improvement of about 80% in 40 nm-width and 80 nm-periodicity structures.

4.3.- EXPERIMENTAL VALIDATION

Although the results reported in the previous sections are very promising and can help to optimize OSC and to increase their efficiency, they are still theoretical work that needs to be linked to real experimental data. The aim of this subsection is to validate the proposed simulation scheme by trying to reproduce experimentally measured characteristic values of interdigitated devices manufactured in our facilities. The Nano-Electronic and Photonic Systems (NePhoS) group of the Universitat Rovira i Virgili has developed a method to fabricate polymer nanopillars that can be applied to manufacture OSC [Santos-2010]. By using the template-assisted synthesis method with nanoporous anodic alumina templates (NAAT) we have obtained functional devices that can be compared with our models. Here we use cells

with a structure of ITO/PEDOT:PSS/P3HT/PCBM/Ag. To totally fit the model to the real devices some adaptations and parameter adjustments have been performed.

4.3.1.- STRUCTURE DEFINITION AND EXPERIMENTAL RESULTS

The structure of the analyzed interdigitated OSC is shown in Figure 4.13. The geometrical features of the manufactured devices, such as the thickness of each layer and the nanopillar dimensions, are depicted in Table 4.3. To be consistent with the previous nomenclature we have that the nanopillar diameter (groove width) is $\alpha = 60$ nm, the interpillar distance (period) is $\beta = 100$ nm, the ratio of the groove width to the period ($\gamma = \alpha/\beta$) is $\gamma = 0.6$ nm, and the nanopillar height (excluding the support base layer) is $T = 80$ nm. If this device is compared with the previous modelled ones, we can find some differences. In this case the P3HT nanopillars support base layer is considerably thicker that the previous one (45 nm instead of 10 nm). Also we have now a back silver (Ag) electrode instead of an aluminium (Al) one as in the previous cases. With these differences, the model will need little a priori modifications.

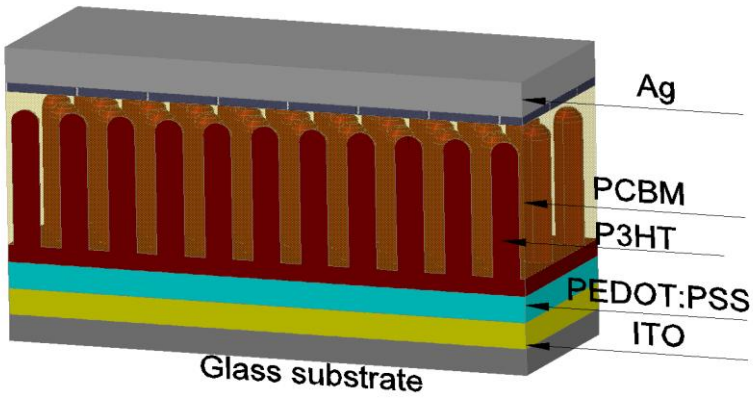

Figure 4.13 *Schematic model of the interdigitated OSC analyzed in this subsection with the structure ITO/PEDOT:PSS/P3HT/PCBM/Ag. Reproduced from [Balderrama-2014].*

UNIVERSITAT ROVIRA I VIRGILI
DESIGN AND MODELLING OF INTERDIGITATED AND NANOSTRUCTURED POLYMER SOLAR CELLS
Pedro Granero Secilla
Dipòsit Legal: T 891-2015

LAYER	***THICKNESS (nm)***	***NANOPILLARS FEATURES***	***Value (nm)***
ITO	*120*	***P3HT SUPPORT LAYER***	*45*
PEDOT:PSS	*40*	***HEIGHT (T)***	*80*
PCBM	*35*	***DIAMETER (α)***	*60*
Ag	*100*	***INTERPILLAR DISTANCE (β)***	*100*

Table 4.3 *Geometrical features of the analysed device showing the thickness of each layer and the nanopillars dimensions. In this case the parameter T does not include the support base thickness.*

Several complete devices were manufactured in our facilities in the same fabrication process. This allows, in principle, obtaining cells with the same constituent materials. However, we always can find differences between the cells regarding their behaviour due to small variations of temperature, pressure or material properties during the fabrication process. In our case we obtained eleven working devices with a similar behaviour but with a little deviation in the results. Figure 4.14 depicts an average *J–V* curve of the analyzed experimental interdigitated OSC. The inset table shows the average characteristic parameters of this device.

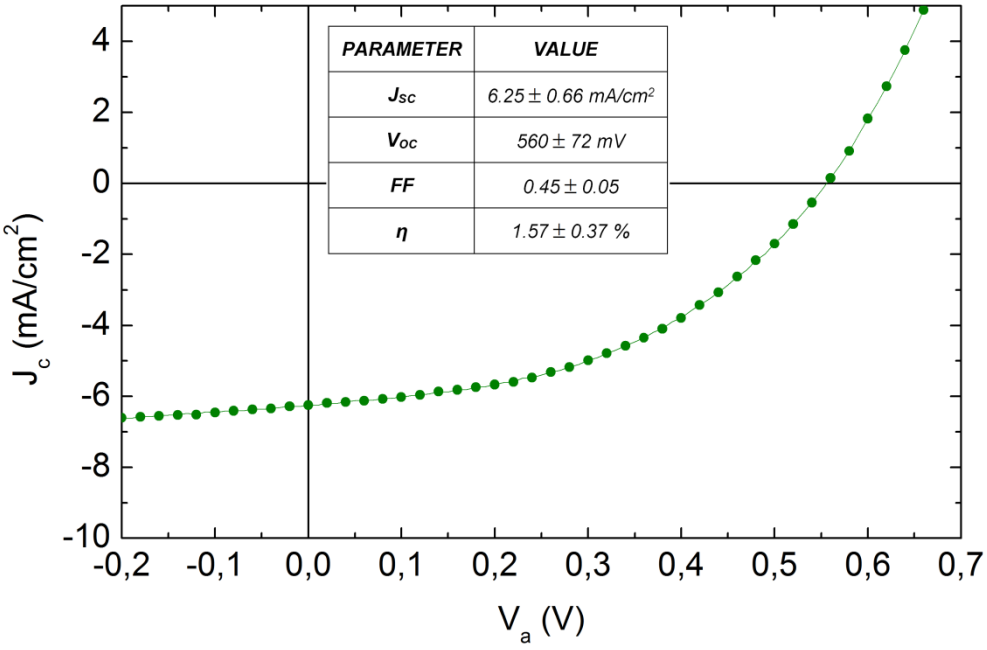

Figure 4.14 *Average J–V curve of the analyzed experimental interdigitated OSC. The inset table shows the average characteristic parameters of this device.*

4.3.2.- MODEL APPLICATION TO INTERDIGITATED OSC

4.3.2.1.- FIRST APPROXIMATION

The first step to reproduce the experimental results has been to apply directly our theoretical simulation model and to check the obtained results in each stage. So first, the device structure has been defined with the geometrical features previously seen. Then, by applying the optical simulation method, taking into account that now the back metal contact is silver, we have obtained the exciton generation rate as a function of the position. After it, the *exciton diffusion equation* was solved to obtain

UNIVERSITAT ROVIRA I VIRGILI
DESIGN AND MODELLING OF INTERDIGITATED AND NANOSTRUCTURED POLYMER SOLAR CELLS
Pedro Granero Secilla
Dipòsit Legal: T 891-2015

the maximum attainable photogenerated current density (J_{PHOTO}) and we have compared this value with the average J_{sc} from the real device:

- $J_{PHOTO-SIMULATION}$ = 1.61 mA/cm^2
- $J_{sc-EXPERIMENTAL}$ = 6.25 mA/cm^2

As it can be seen, the obtained J_{PHOTO} is much lower (close to four times) than the experimental value. Considering that J_{PHOTO} is a maximum ideal current, the final current given by the cell will be lower than this value, we have that in our model the exciton generation rate is lower than it should be or that exciton losses are very high. So the model needs to be checked to solve this issue.

4.3.2.2.- MODEL ADAPTION AND PARAMETER FITTING

The exciton generation rate in an OSC depends on the amount of light that it can absorb, specifically in the active region (P3HT layer). Hence, to increase this rate it is mandatory to increase somehow light absorption there.

The first thing done was to check the layers that are above the P3HT one, since they are the first ones to receive the incident light. From here we got that the PEDOT:PSS layer was absorbing too much light. One of the characteristics of this polymer is that is nearly transparent so it can be used in photovoltaics. However, as it can be seen in Figure 4.15B, we choose non-optimal optical constants for it. The used PEDOT:PSS has a high extinction coefficient for wavelengths were P3HT is more absorbent, with peaks around 350nm and 550 nm. So we had to change the optical constants for PEDOT:PSS [Hoppe-2002].

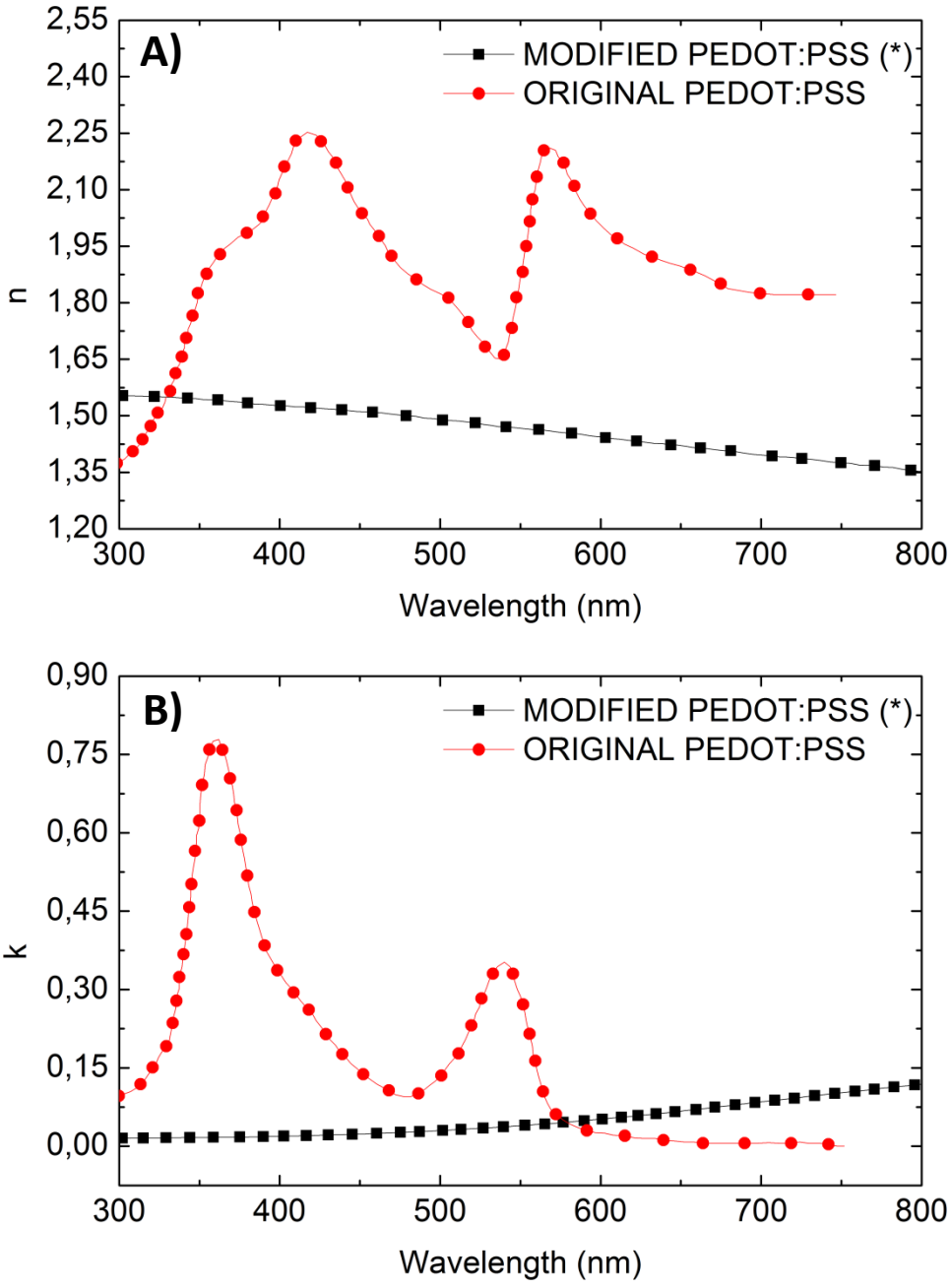

Figure 4.15 *Original and modified values of the refractive index (n) (A) and extinction coefficient (k) (B) of the complex index of refraction (ñ = n + ik) of the PEDOT:PSS considered in the simulations. *Modified values taken from literature [Hoppe-2002].*

UNIVERSITAT ROVIRA I VIRGILI
DESIGN AND MODELLING OF INTERDIGITATED AND NANOSTRUCTURED POLYMER SOLAR CELLS
Pedro Granero Secilla
Dipòsit Legal: T 891-2015

Our previous optical computations were restricted to a wavelength range of 280 – 650 nm, since it is the usual considered absorption range of P3HT. However, some works [Nolasco-2010] report that P3HT can show a bandgap of up to 1.7 eV. That means that this material can exploit photons from a light source with a wavelength up to 730 nm. For the range of wavelengths of 650 – 730 nm P3HT is slightly absorbent. If such additional absorption range is considered, the total amount of absorbed power predicted by the model would increase.

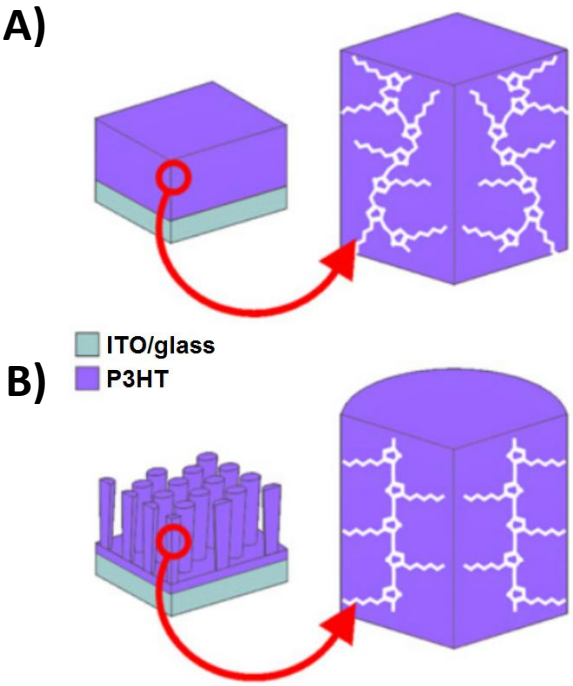

Figure 4.16 *Scheme showing how the P3HT chains are randomly arranged inside a film type layer (A) and scheme showing the arrangement of the P3HT chains inside the nanopillars after the NAATs infiltration (B). Reproduced from [Santos-2010].*

UNIVERSITAT ROVIRA I VIRGILI
DESIGN AND MODELLING OF INTERDIGITATED AND NANOSTRUCTURED POLYMER SOLAR CELLS
Pedro Granero Secilla
Dipòsit Legal: T 891-2015

Regarding exciton losses, we have that one of the most limiting keys in organic photovoltaics is the small exciton diffusion length (L_D) of the organic materials. A higher L_D will increase significantly the photogenerated current density of a device. In our previous simulation analysis, we have used a L_D of 11 nm, hence, by increasing this length it can be possible to get closer to the experimental current densities values. However we cannot increase this parameter in an arbitrary way.

In previous works, the Nano-Electronic and Photonic Systems (NePhoS) group of the Universitat Rovira i Virgili has shown that high-density arrays of P3HT nanopillars have a higher conductivity than thin films of the same polymer [Santos-2010]. By means of μ-X-ray diffraction, it has been demonstrated that there is nanoconfinement of polymer chains into the pores during the template-assisted process. This implies a high alignment of such chains into the nanopillars bulk (Figure 4.16) and, thus, an increase of conductivity. It is possible that this chain alignment can also favour exciton diffusion, hence P3HT L_D can be larger than expected. So to use a higher value for L_D in our simulation is justified.

By applying the modifications explained above (the adapted optical constants of the PEDOT:PSS, the extended incident light wavelength range, and the variation of the exciton diffusion length of P3HT) we have been able to achieve current densities as high as the experimental values as it can be seen in the Table 4.4. With this issue solved, it is possible to proceed to obtain the complete *J–V* characteristics.

UNIVERSITAT ROVIRA I VIRGILI
DESIGN AND MODELLING OF INTERDIGITATED AND NANOSTRUCTURED POLYMER SOLAR CELLS
Pedro Granero Secilla
Dipòsit Legal: T 891-2015

J_{sc} EXPERIMENTAL	J_{PHOTO} SIMULATION	EXCITON DIFFUSION LENGTH (L_D)
6.25 mA/cm^2	6.25 mA/cm^2	15.34 nm

Table 4.4 *Experimental short-circuit current density (J_{sc}), maximum attainable photogenerated current density (J_{PHOTO}) obtained from the simulations, and the exciton diffusion length (L_D) needed to achieved this current.*

Finally, by varying the free charge mobilities, it is possible to modify the form of the *J–V* curve, specially the knee. This allows adapting the curve to match the *FF* and the shunt and series resistances to the experimental data. The hole mobility in P3HT can range from 10^{-5} to 10^{-2} cm^2/(V·s), with a typical value of $2\cdot10^{-4}$ cm^2/(V·s), and the electron mobility in PCBM can range from $2\cdot10^{-3}$ to $2\cdot10^{-2}$ cm^2/(V·s), with a typical value of $3\cdot10^{-3}$ cm^2/(V·s) [Monestier-2007]. The final used values were:

- **Hole mobility in P3HT** = $2\cdot10^{-4}$ cm^2/(V·s)
- **Electron mobility in PCBM** = $3\cdot10^{-3}$ cm^2/(V·s)

Figure 4.17 shows the average *J–V* curve of the analyzed experimental interdigitated OSC (green circles) and the final simulation reproduction (black triangles). It can be seen that both curves are quite similar. However they do not totally match, having the biggest discrepancies between V_a = 0.2 V and 0.4 V where the simulation curve achieves lower values than the experimental one. The inset table shows the average characteristic parameters of the experimental device and the ones obtained via simulation. Despite the obtained values from the simulation differs from the experimental ones, the experimental data were average values and the differences are within the standard deviation range.

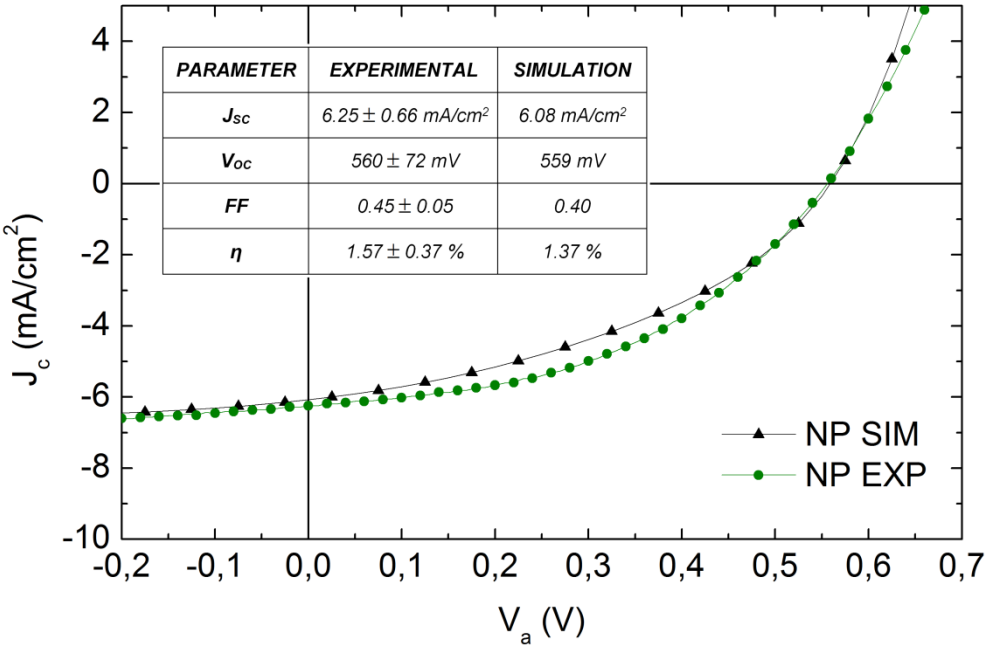

Figure 4.17 *Average J–V curve of the analyzed experimental interdigitated OSC (green circles) and the simulation reproduction (black triangles). The inset table shows the average characteristic parameters of the experimental device and the ones obtained via simulation.*

4.4.- SUMMARY AND CONCLUSIONS

In this chapter we have presented two studies about the analysis and the optimization of interdigitated OSC, one simulating only the active region and another considering the complete device. In the first one, we have analyzed the influence of the nanostructured dissociation interface on the light absorption properties and on the charge carrier generation of interdigitated nanostructures. We have considered a wide range of nanostructuring periods, from very small values as compared with the

UNIVERSITAT ROVIRA I VIRGILI
DESIGN AND MODELLING OF INTERDIGITATED AND NANOSTRUCTURED POLYMER SOLAR CELLS
Pedro Granero Secilla
Dipòsit Legal: T 891-2015

incident solar light wavelengths (λ) to much bigger values, and several geometrical ratios between the fix 10 nm-thick support planar layer and the structure height. We have restricted the study to P3HT and PCBM as constituents of the OSC and we have considered light absorption only in the active region of the structures (P3HT layer) and for its absorption spectrum range. The study has been carried out on the basis of finite-element simulations with the COMSOL software, hence magnitudes are all as a function of the position. This is an important consideration, since nearly all the similar studies always consider uniform approximations of several magnitudes, such as light absorption or exciton generation rate, inside the materials.

Regarding light absorption, results can be divided into four groups, depending on the magnitude of the nanostructuring characteristic size (α). For sizes smaller than 12.5 nm we have observed that the nanostructures behave as an effective medium. This is especially remarkable since although the optical performance of the layer is the same as that of an effective medium material, the two components of the structure are actually separated. This means that the nanostructured P3HT is absorbing more light as the electric field is enhanced by the close proximity of the PCBM, which has a higher refractive index. The second group corresponds to sizes in between those of the first group and sizes of the order of magnitude of λ/2. The absorption properties for these sizes show a transition in the behaviour between these two groups, with a decrease in the total absorption with increasing nanostructuring sizes. When α is of the order of magnitude of λ/2, the nanostructure acts as a subwavelength diffraction grating which couples light into the nanostructured layer resulting in an increased light absorption due to light trapping. The absorption spectra exhibit a wavelength dependence clearly different from that of the P3HT. This dependence varies critically with the nanostructuring size showing maxima at different wavelengths depending on α. For structuring sizes bigger than λ/2, we have observed that the structured

UNIVERSITAT ROVIRA I VIRGILI
DESIGN AND MODELLING OF INTERDIGITATED AND NANOSTRUCTURED POLYMER SOLAR CELLS
Pedro Granero Secilla
Dipòsit Legal: T 891-2015

interface also acts as a diffraction grating giving rise to some amount of light trapping. Although for this case the spectra are not influenced by the structuring features.

We have also estimated the amount of absorbed light that actually contributes to charge generation. By solving the exciton diffusion equation, using the previously calculated absorption maps as inputs, we have obtained the exciton flux at the dissociation interface and, from there, the maximum attainable photogenerated current density of the complete OSC. In this case, the smallest nanostructuring sizes give rise to the biggest J_{PHOTO} with respect to the planar bilayer reference structures. That means that even though the amount of absorbed light is not the maximum, a higher amount of it is contributing to photocurrent. The reason of this behaviour can be attributed to the poor transport properties of the organic semiconductors and to their short exciton diffusion length. For the smallest nanostructuring periods, nearly all the excitons are generated close enough to the dissociation interface and they are able to dissociate. This not happens for the bigger sizes, so we have higher losses due to exciton recombination. The decreasing trend of the J_{PHOTO} is only changed for nanostructuring sizes of the order of magnitude of $\lambda/2$, where the effect of light trapping is noticeable.

The height of the nanostructures is also an important factor in the performance of the structures. As the geometrical ratio between the support planar layer and the structure height increases the J_{PHOTO} also increases despite having the higher structures (big values of T) a lower relative total absorbed light. This fact can also be attributed to the short exciton diffusion length of the involved materials. A thick planar bilayer structure will absorb a higher amount of light, however most of the generated excitons will recombine before reaching the Donor–Acceptor interface and dissociate. On the contrary, in high nanostructured interfaces excitons will still find a dissociation interface before recombination, provided the period is small enough.

UNIVERSITAT ROVIRA I VIRGILI
DESIGN AND MODELLING OF INTERDIGITATED AND NANOSTRUCTURED POLYMER SOLAR CELLS
Pedro Granero Secilla
Dipòsit Legal: T 891-2015

The most remarkable conclusion of this study is that for all nanostructuring sizes an improvement with respect to the reference planar devices is observed. We have obtained that for an optimal structure thickness and period the increment in the photocurrent can be more than a factor 6. Hence, the nanostructured dissociation interface of interdigitated OSC can be considered a source of both optical and electrical behaviour enhancement. The conclusions of this study, in addition with future analysis, can be helpful to improve and to optimize the design of interdigitated devices.

In the second study, we analyzed the influence of the nanostructured dissociation interface on the overall efficiency of interdigitated heterojunction full organic solar cells. Also by means of finite-element numerical modeling, we performed a systematic and complete analysis of light absorption, exciton diffusion and carrier transport, all in the same numerical framework, and for a 2D model of such cells. With this, we obtain their dependence on the cell geometrical parameters: pillar diameter and height, and nanostructure period. The donor and the acceptor materials of our cells are also P3HT and PCBM, respectively. The aim of this study is to develop a more accurate model than the one of the previous study for this kind of cells, which can be used for their optimal design.

From the point of view of light absorption, results show that the maximum amount of light is absorbed only for two specific values of the nanopillar height, T = 80 nm and T = 230 nm, independently of the nanopillar diameter. This suggests that it is due to light interference effects. For these nanopillar heights, the maximum absorption is achieved by nanostructures with a period of β = 25 nm. Due to the presence of additional layers, these results are a little different in magnitude from the ones of the first study. However, the trend seems to be similar, light absorption increases when

UNIVERSITAT ROVIRA I VIRGILI
DESIGN AND MODELLING OF INTERDIGITATED AND NANOSTRUCTURED POLYMER SOLAR CELLS
Pedro Granero Secilla
Dipòsit Legal: T 891-2015

nanopillar height increases until a certain point. Nevertheless, in the first case we did not consider nanopillar heights as big as in this case.

By simulating the exciton diffusion process the maximum attainable photocurrent density (J_{PHOTO}) can be determined. Results show that to obtain a higher J_{PHOTO} than that of the better planar bilayer structure, small nanostructure periods, up to 100 nm, should be used. This result is in good agreement with the one of the previous study, where we obtained higher J_{PHOTO} with small geometries. However, in that case in all the interdigitated models we get higher currents than in the planar bilayer equivalent one. By examining the exciton diffusion maps, we can conclude that small nanopillars favor the excitons to reach the Donor–Acceptor interface and that the upper limit of the nanopillar height is directly related to the limited exciton diffusion length.

Finally, from the *J–V* characteristics, we obtain the overall efficiency of the cells. We observe that there is a direct correlation between the J_{PHOTO} and the cell efficiency, which indicates that the charge transport has a lower influence on the overall charge collection efficiency. Thus, in order to increase the efficiency, the exciton diffusion process is the key limiting factor and this process is better for the smaller nanopillar diameters, as we also have conclude from the first study. For β = 25 nm, the efficiency depends strongly on the ratio of the nanopillar diameter to the nanopillar period (γ) being bigger for higher values of it. Instead, if β values above 100 nm are considered, then the efficiency is essentially independent of the γ since the increase in light absorption is almost compensated by the exciton recombination losses. Best results have been achieved for β = 25 nm, T = 80 nm, and γ = 0.75, with an efficiency that is 3.6 times higher than the best planar bilayer reference device.

An optimal interdigitated structure should find a compromise between a high proportion of electron donor to increase light absorption and a small pillar diameter

UNIVERSITAT ROVIRA I VIRGILI
DESIGN AND MODELLING OF INTERDIGITATED AND NANOSTRUCTURED POLYMER SOLAR CELLS
Pedro Granero Secilla
Dipòsit Legal: T 891-2015

to ensure an extended D–A interface for exciton dissociation. Due to the short exciton diffusion length of organic materials, big nanopillars diameters will result in cells with an efficiency even lower than the one of planar bilayer equivalents. The method developed in this work can be useful to design optimal full organic solar cells, taking into account technological parameters and constraints.

After these theoretical studies, a validation of the simulation method with experimental results, manufactured in our facilities, has been presented. By using the template-assisted synthesis method with nanoporous anodic alumina templates (NAAT) we have obtained functional devices that can be compared with our models. These devices have the structure of ITO/PEDOT:PSS/P3HT/PCBM/Ag. To totally fit the model to the real devices, some adaptations and parameter adjustments have been performed. The adaptations have included the use of modified optical constants for the PEDOT:PSS layer, an extended solar spectrum range, a modified exciton diffusion length for P3HT, and free charge mobilities adjustments. After these adaptations, the simulated results were in good agreement with the experimental data.

UNIVERSITAT ROVIRA I VIRGILI
DESIGN AND MODELLING OF INTERDIGITATED AND NANOSTRUCTURED POLYMER SOLAR CELLS
Pedro Granero Secilla
Dipòsit Legal: T 891-2015

UNIVERSITAT ROVIRA I VIRGILI
DESIGN AND MODELLING OF INTERDIGITATED AND NANOSTRUCTURED POLYMER SOLAR CELLS
Pedro Granero Secilla
Dipòsit Legal: T 891-2015

CHAPTER 5

ANALYSIS AND COMPARISON OF DIFFERENT NANOSTRUCTURES IN ORGANIC SOLAR CELLS

This chapter is devoted to the application of the improved numerical simulation procedure to organic solar cells with the same structure but with different nanostructured D–A junctions. By varying the D–A interface geometry, we have modelled planar bilayer (PBL), nanopillars (NP), nanowells (NW) and nanopyramids (NPYR) D–A junctions. The purpose of this chapter is to compare these kinds of nanostructured junctions in OSC for the two existing configurations, the conventional and the inverted one. A light absorption and an exciton diffusion study are carried out to check which configuration is better in terms of efficiency for each case. In this study, the exciton diffusion length (L_D) is used as a parameter since, as we have seen in the previous chapter, can vary due to the nanoconfinement of polymer chains.

5.1.- DEFINITION OF THE STUDIED JUNCTION MORPHOLOGIES AND CELL ARCHITECTURES.

5.1.1.- DONOR–ACCEPTOR JUNCTION

The different Donor–Acceptor (D–A) junction morphologies that have been modelled are shown in Figure 5.1, where it can be seen the used D–A nanostructured junctions: planar bilayer (PBL) (Figure 5.1A), nanopillars (NP) (Figure 5.1B), nanowells (NW) (Figure 5.1C), and nanopyramids (NPYR). The only difference between the NW and the NPYR junctions is which form acquires the P3HT layer. If this layer is formed by wells and the PCBM one by pyramids (like in Figure 5.1C) we have a NW junction. If it is the opposite way (pyramids in the P3HT layer and wells in the PCBM one) we have a NPYR junction. For all cases, the structure of the devices follows the layers distribution ITO/PEDOT:PSS/P3HT/PCBM/Ag.

In Table 5.1 and in Figure 5.2 it can be seen the values of the dimensions for the different nanostructured D–A features. These values have not been chosen arbitrarily, but have been taken from experimental devices manufactured by the NePhoS group of the Universitat Rovira i Virgili. The NP junction has been obtained by using the template-assisted synthesis method with nanoporous anodic alumina templates (NAAT) explained in Chapter 2. The NW and the NPYR junctions have been obtained by using the nanoimprint lithography (NIL) method. In this method, a predefined pattern is replicated into a deformable material coated on a surface. The predefined pattern is usually created on a rigid material (master stamp) that can be used directly, or serve as template from which elastomeric stamps (soft stamps) are molded [Avnon-2011].

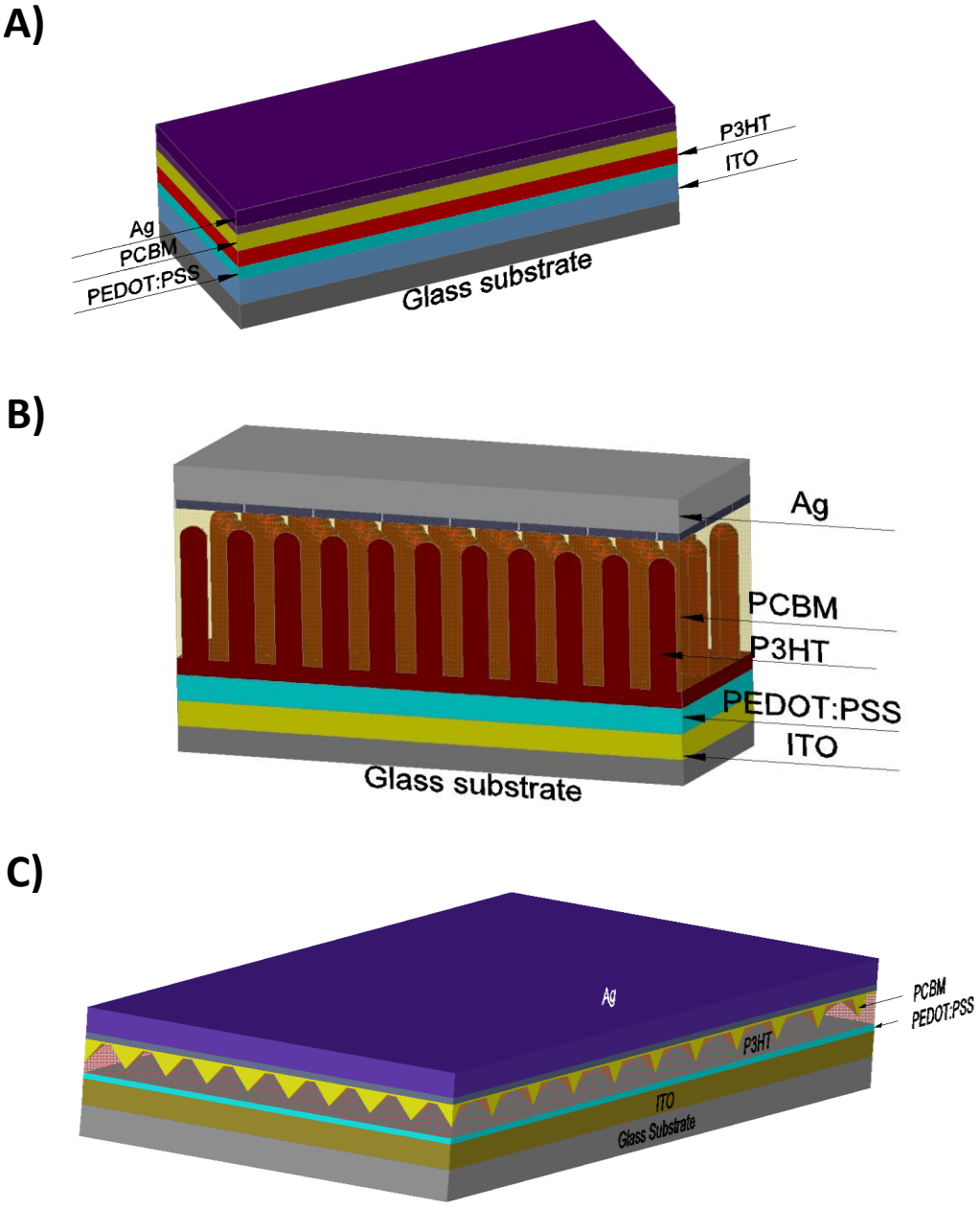

Figure 5.1 *Scheme of the simulated devices (A) planar bilayer (PBL), (B) nanopillars (NP), and (C) nanowells (NW). The only difference between the NW and the NPYR junctions is which form acquires the P3HT layer.*

Parameter (nm)	***Planar Bilayer (PBL)***	***Nanopillars (NP)***	***Nanowells (NW)***	***Nanopyramids (NPYR)***
ITO layer*	*120*	*120*	*120*	*120*
PEDOT:PSS layer*	*40*	*40*	*40*	*40*
P3HT layer*	*130*	*45*	*45*	*45*
PCBM layer*	*40*	*35*	*50*	*50*
Ag layer*	*100*	*100*	*100*	*100*
PILLAR/WELL/PYR height	*-*	*80***	*100****	*100****
PILLAR/WELL/PYR width	*-*	*60***	*130****	*130****
PILLAR/WELL/PYR period	*-*	*100***	*230****	*230****

Table 5.1 *Dimensions for the different nanostructured D–A features. *Layer total thickness, ** Figure 5.2A, ***Figure 5.2B.*

UNIVERSITAT ROVIRA I VIRGILI
DESIGN AND MODELLING OF INTERDIGITATED AND NANOSTRUCTURED POLYMER SOLAR CELLS
Pedro Granero Secilla
Dipòsit Legal: T 891-2015

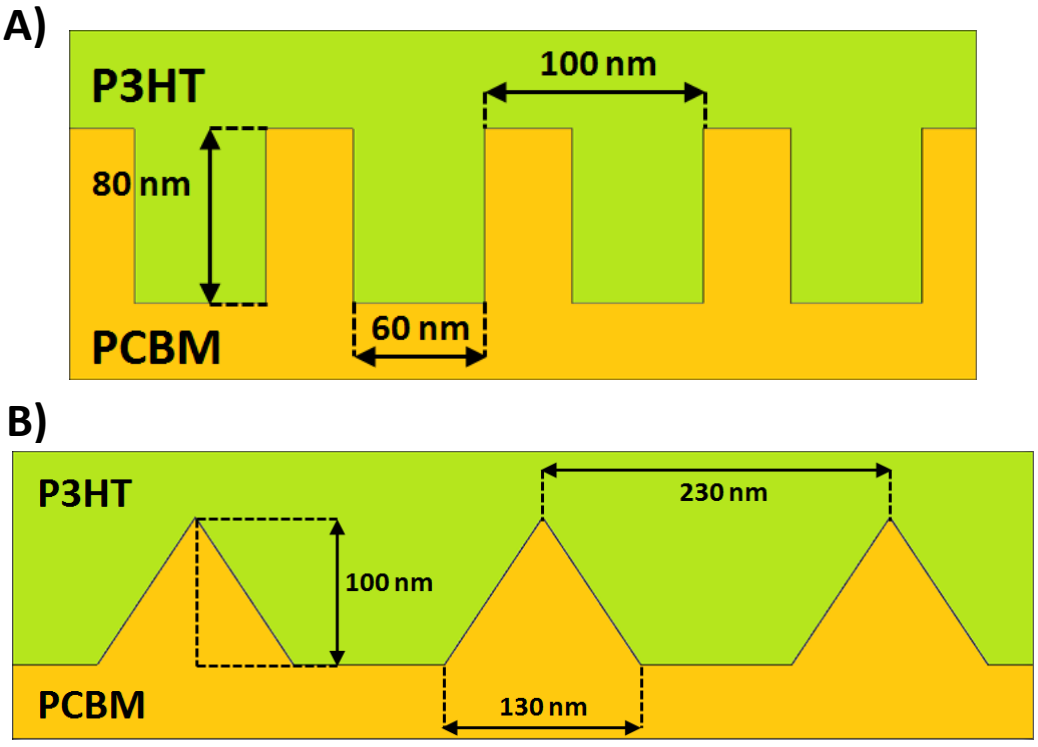

Figure 5.2 *Scheme of the features for the nanopillar (NP) structure (A), and for the nanowells (NW) one (B). For the NPYR case the P3HT and the PCBM layers geometry are swapped.*

5.1.2.- CONVENTIONAL AND INVERTED CONFIGURATIONS

In most conventional OSC, a PEDOT:PSS hole transport layer and a low work function metal electrode, such as aluminium or calcium, are generally used. However, the strong acidic property of the PEDOT:PSS layer is detrimental to the ITO electrode, and the low-work-function metal can be easily oxidized in air, both degrading the device performance easily in air and leading to a poor stability of the cell [de Jong-2000; Greczynski-2001; Pacios-2006; Kyaw-2008; Lin-2013]. A promising solution to improve the air stability of OSC is to use the inverted configuration [Hau-2008; Chen-2009; Xu-

2009; Hau-2010] (Figure 5.3), where an n-type metal oxide film is used as the electron transport layer on a ITO substrate (cathode) and a high work function metal, such as silver or gold, is used as the top anode. In the inverted configuration, both the low-work-function metal and the ITO/PEDOT:PSS interface can be avoided so it is possible to enhance the device air stability, i.e., to increase the cell durability.

To obtain an efficient device for the inverted configuration, it is crucial to choose a proper electron transport layer: it should work as a high conductive path for efficient electron extraction while exhibiting good hole blocking capability. Among others, titanium dioxide (TiO_2) has shown good results due to its superior air stability as compared to other semiconductor oxides [Lin-2013]. In our simulation study we model a thin film of TiO_2 (10 nm) as the electron transport layer for the inverted configuration for each type of D–A interface nanostructuring.

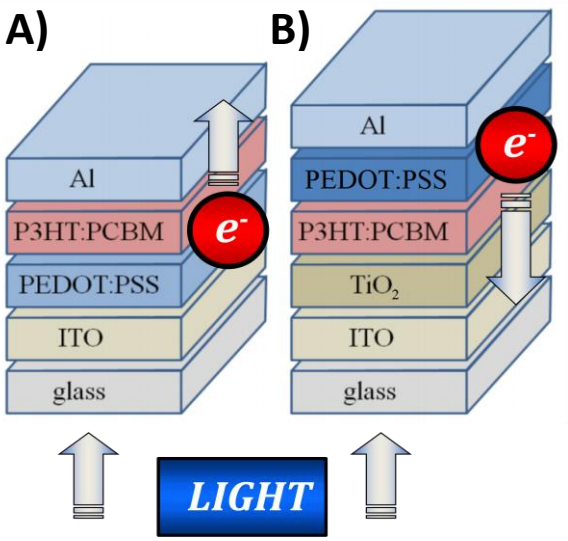

Figure 5.3 *Structure schemes of the conventional (A) and the inverted (B) configurations in OSC. For the conventional configuration, the ITO/PEDOT:PSS layers act as the anode and the Al one acts as the cathode. For the inverted case, the ITO/TiO_2 layers act as cathode and the Al one acts as the anode instead.*

UNIVERSITAT ROVIRA I VIRGILI
DESIGN AND MODELLING OF INTERDIGITATED AND NANOSTRUCTURED POLYMER SOLAR CELLS
Pedro Granero Secilla
Dipòsit Legal: T 891-2015

5.2.- INFLUENCE OF THE JUNCTION MORPHOLOGY IN LIGHT ABSORPTION

Figures 5.4 and 5.5 shows the amount of absorbed light in W/m (*Total power dissipation density*) in the P3HT layer as a function of the wavelength for all the considered structures. These results are grouped in four graphs, one for each type of D–A nanostructuring. For both the conventional and the inverted configurations and for all nanostructure kinds the curves follow a similar trend: most of the light is absorbed in the wavelength range between 350 nm and 650 nm, which corresponds to the absorption band of the P3HT. It can be also observed that for all nanostructure kinds, the conventional cells absorb a higher amount of light up to a cut-off wavelength, at which the inverted configuration absorption overcomes the conventional one. The cut-off wavelength is only slightly dependent on the kind of nanostructure: for the PBL and the NP structures is 575 nm while for NW and NPYR is 625 nm. Above this cut-off, the absorption for the inverted PBL and NP structures becomes again smaller than the conventional above 800 nm.

The reduction of absorption in the low wavelength range for the inverted configuration is undoubtedly caused by the absorption in the PCBM acceptor layer, which is highly absorbent below 550 nm. Nevertheless, this reduction is compensated up to a certain amount by the increase above the cut-off. In summary, the reduction of absorbed energy in all the spectral range in the inverted configurations is 23.90 % for PBL, 14.37% for NP, 37.55 % for NW and up to 39.72% for NPYR. It is also worth to note that the graphs in Figures 5.4 and 5.5 are in the same scale and that the plots have similar heights and widths. This means that the total absorbed energy is similar for the conventional structures on one side, or the inverted structures on the other, and that the different nanostructuring of the acceptor/donor interface has a little impact in the absorption of light.

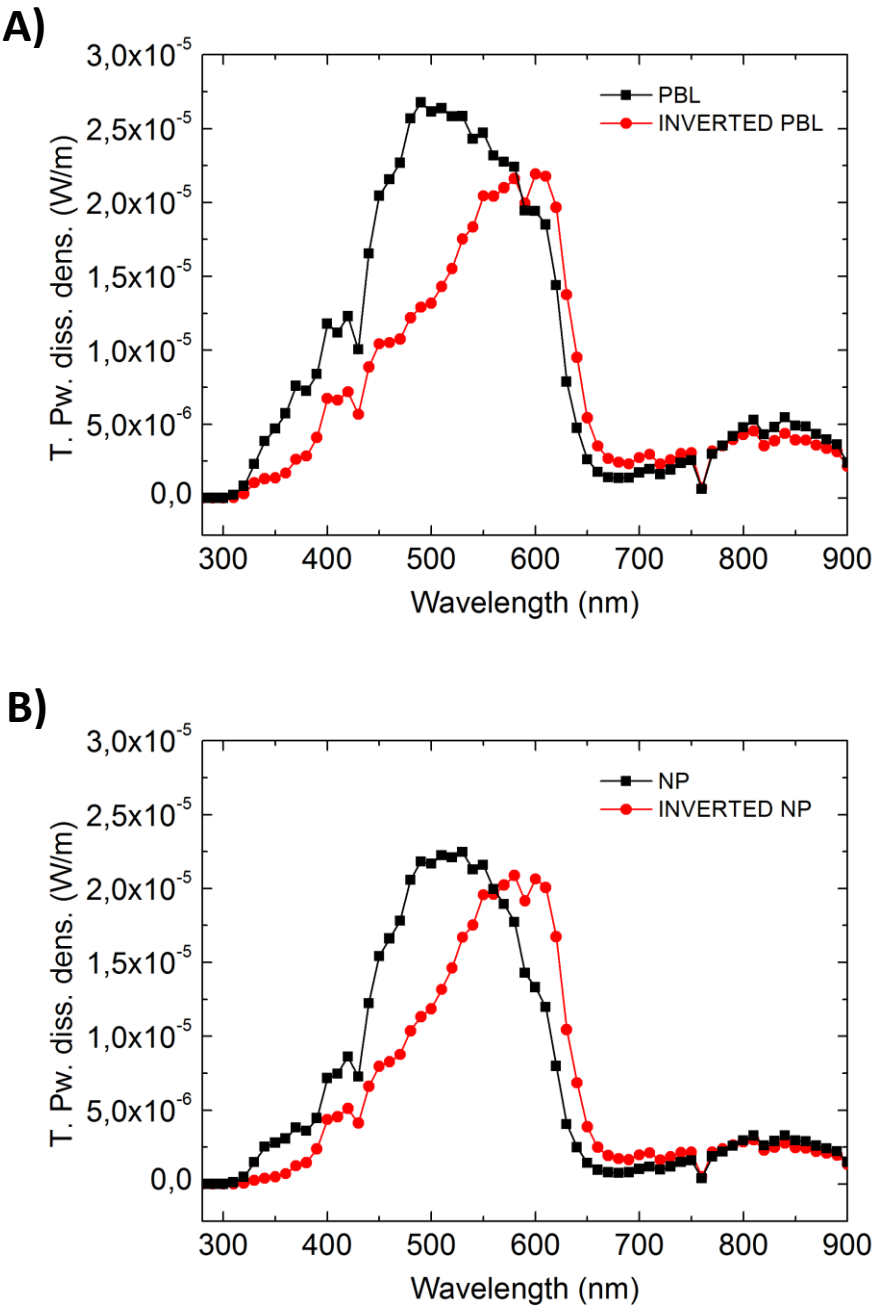

Figure 5.4 *Amount of absorbed light in W/m (Total power dissipation density) in the P3HT layer as a function of the wavelength for PBL (A) and NP (B).*

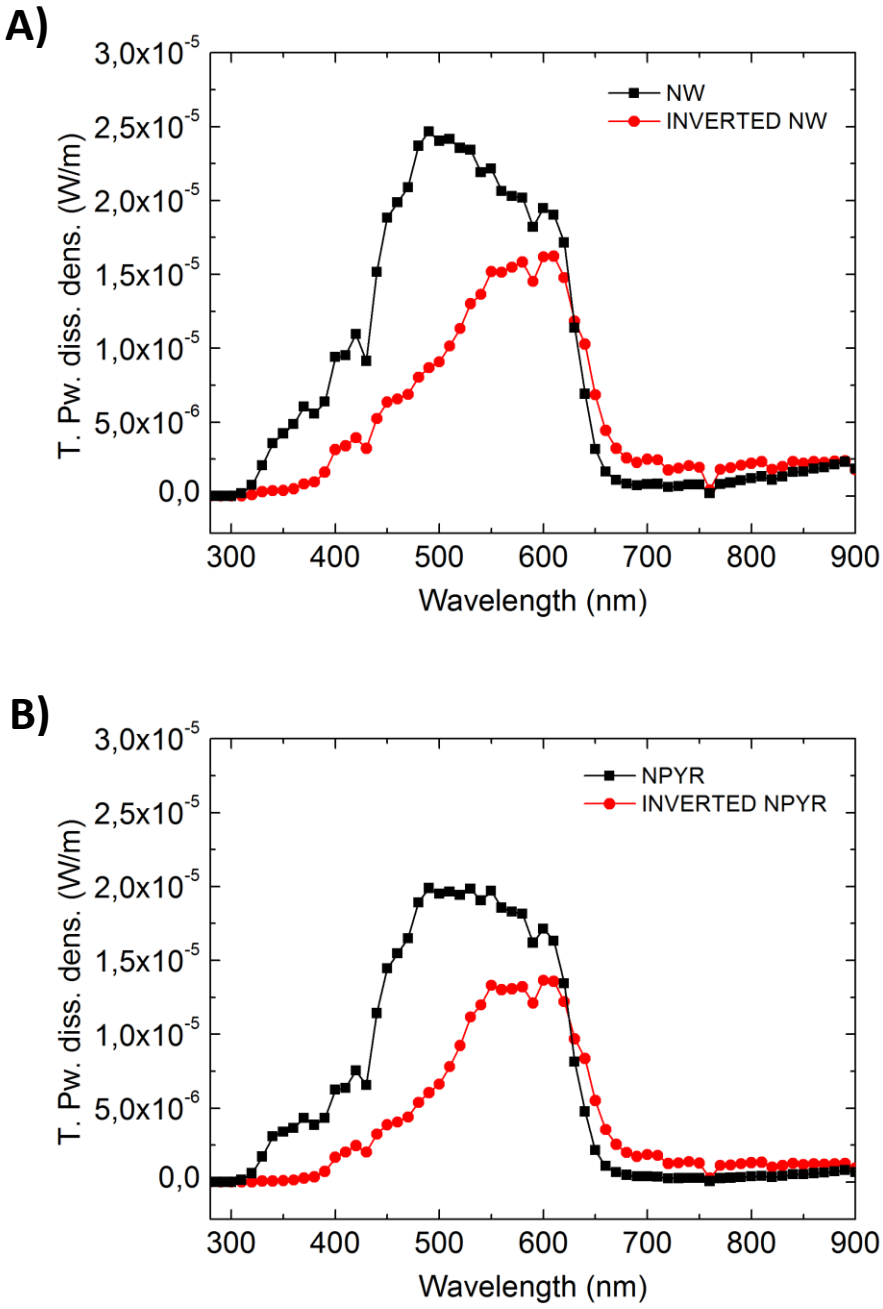

Figure 5.5 *Amount of absorbed light in W/m (Total power dissipation density) in the P3HT layer as a function of the wavelength for NW (A) and NPYR (B).*

UNIVERSITAT ROVIRA I VIRGILI
DESIGN AND MODELLING OF INTERDIGITATED AND NANOSTRUCTURED POLYMER SOLAR CELLS
Pedro Granero Secilla
Dipòsit Legal: T 891-2015

5.3.- INFLUENCE OF THE JUNCTION MORPHOLOGY IN EXCITON DIFFUSION

Figure 5.6 depicts the maximum obtainable photogenerated current density (J_{PHOTO}) as a result of the diffusion of the photogenerated excitons. The results correspond to the different kinds of nanostructured D–A interfaces, in conventional and inverted configuration, and for a L_D = 17.5 nm. For the case of PBL, NP and NW it can be observed that higher currents densities for the inverted configuration are obtained, while NPYR the result is the opposite. The higher difference in current density between conventional and inverted configurations occurs for the PBL while the highest absolute current densities are obtained for the NP. These results demonstrate that the use of inverted configurations is justified by a much better efficiency in the collection of excitons, which compensates and overcomes the reduction in light absorption. This better efficiency is caused by the fact that excitons are created closer to the Donor–Acceptor interface. The simulations also show that the nanopillar structure it the most efficient in the collection of the photogenerated excitons, almost doubling that of the planar bilayer, while the NW and NPYR structures show a smaller improvement. It is also interesting to note, that not all kinds of nanostructures are able to perform this compensation as it happens for the NPYR structures. All these findings should be taken into account in the design of nanostructured interfaces.

UNIVERSITAT ROVIRA I VIRGILI
DESIGN AND MODELLING OF INTERDIGITATED AND NANOSTRUCTURED POLYMER SOLAR CELLS
Pedro Granero Secilla
Dipòsit Legal: T 891-2015

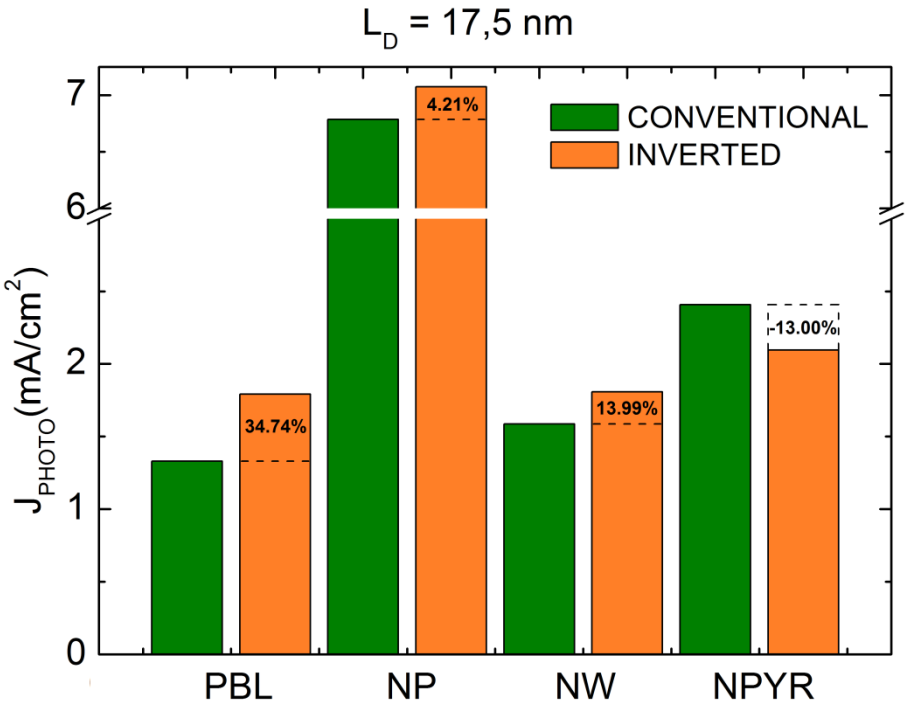

Figure 5.6 *Maximum obtainable photogenerated current density (J_{PHOTO}) as a result of the diffusion of the photogenerated excitons. The results correspond to the different kinds of nanostructures, in conventional and inverted configuration, and for a L_D = 17.5 nm.*

In order to examine the exciton collection efficiency of the different nanostructuring we show in Figures 5.7 and 5.8 the maximum obtainable photogenerated current density (J_{PHOTO}) as a function of the exciton diffusion length (L_D) for all the considered structures. Figures 5.7A, 5.7B, 5.8A and 5.8B show this magnitude for the PBL, the NP, the NW and the NPYR cases respectively. Each graph displays curves for each of the conventional and inverted configurations and includes the maximum possible current density (J_{MAX}) that would be attained in the absence of exciton recombination. The ratio between the value in the curve to this value at a given L_D is an indication of the exciton collection efficiency of the nanostructured interface.

UNIVERSITAT ROVIRA I VIRGILI
DESIGN AND MODELLING OF INTERDIGITATED AND NANOSTRUCTURED POLYMER SOLAR CELLS
Pedro Granero Secilla
Dipòsit Legal: T 891-2015

For the PBL structure, the increase of the J_{PHOTO} with L_D is linear, with a higher value of the inverted structure, and with the two curves converging at the highest L_D. If comparing with the J_{MAX}, it is clear that the inverted structure has much higher exciton collection efficiency at these exciton diffusion lengths. As the inverted configuration J_{MAX} is lower than for the conventional, at some point (probably slightly above L_D = 60nm) the two curves intersect and the inverted PBL structure becomes less efficient in the whole process of light absorption and exciton collection. Instead, for the nanopillars, the increase has a convex shape with a steeper slope at small L_D, which then stabilizes. The inverted structure shows better J_{PHOTO} in the range of investigated L_D, and in this case, as J_{MAX} is nearly the same for both configurations, J_{PHOTO} is also virtually the same above L_D = 60 nm. This means that this structure is optimized both for light absorption and exciton collection.

For the nanowell D–A interface structure (Figure 5.8A) the cross point of the J_{PHOTO} curves appears at a lower L_D = 30nm while for the nanopyramid D–A interface structure (Figure 5.8B) the intersection is even inexistent and the J_{PHOTO} of the inverted configuration is smaller irrespectively of L_D. By comparing the curves with the corresponding J_{MAX} values, it can be seen that even though the nanopyramid has the smaller J_{PHOTO} of the nanostructured interfaces, it has better exciton collection efficiency than the nanowell structure.

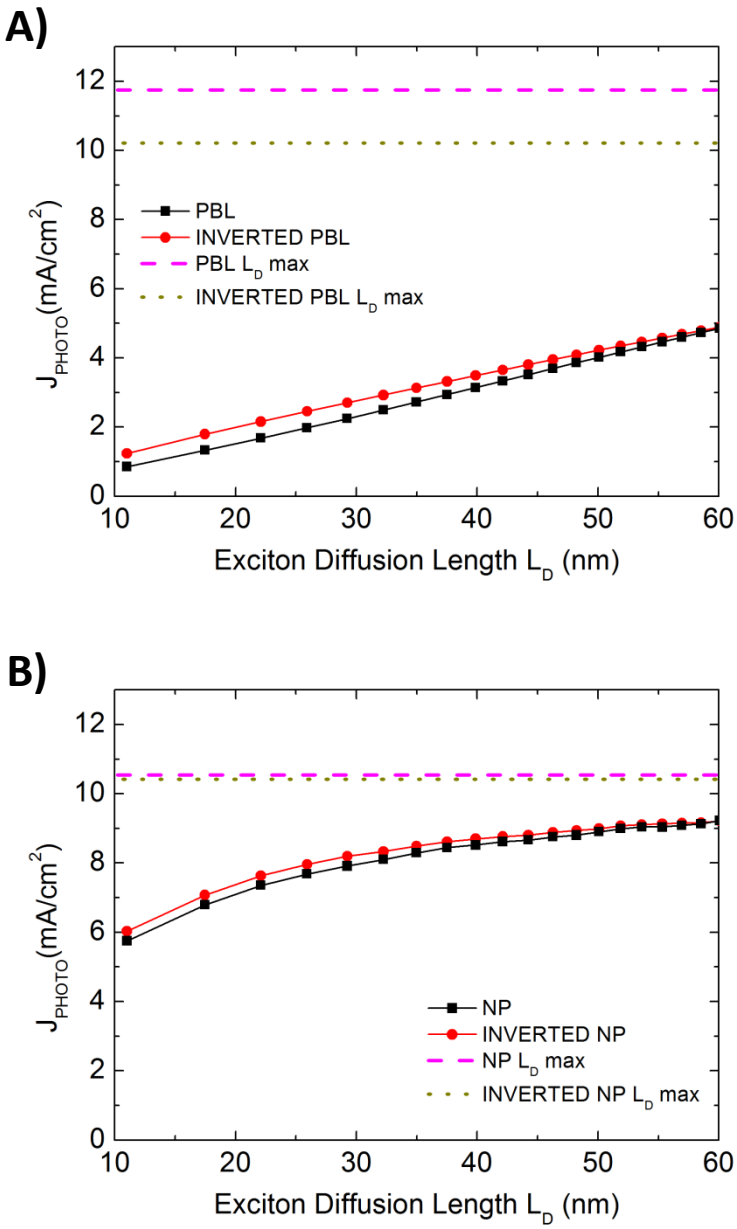

Figure 5.7 *Maximum obtainable photogenerated current density (J_{PHOTO}) as a function of the exciton diffusion length (L_D) for the PBL (A) and the NP (B) cases. Each graph displays also the maximum possible current density (J_{MAX}) that would be attained in the absence of exciton recombination.*

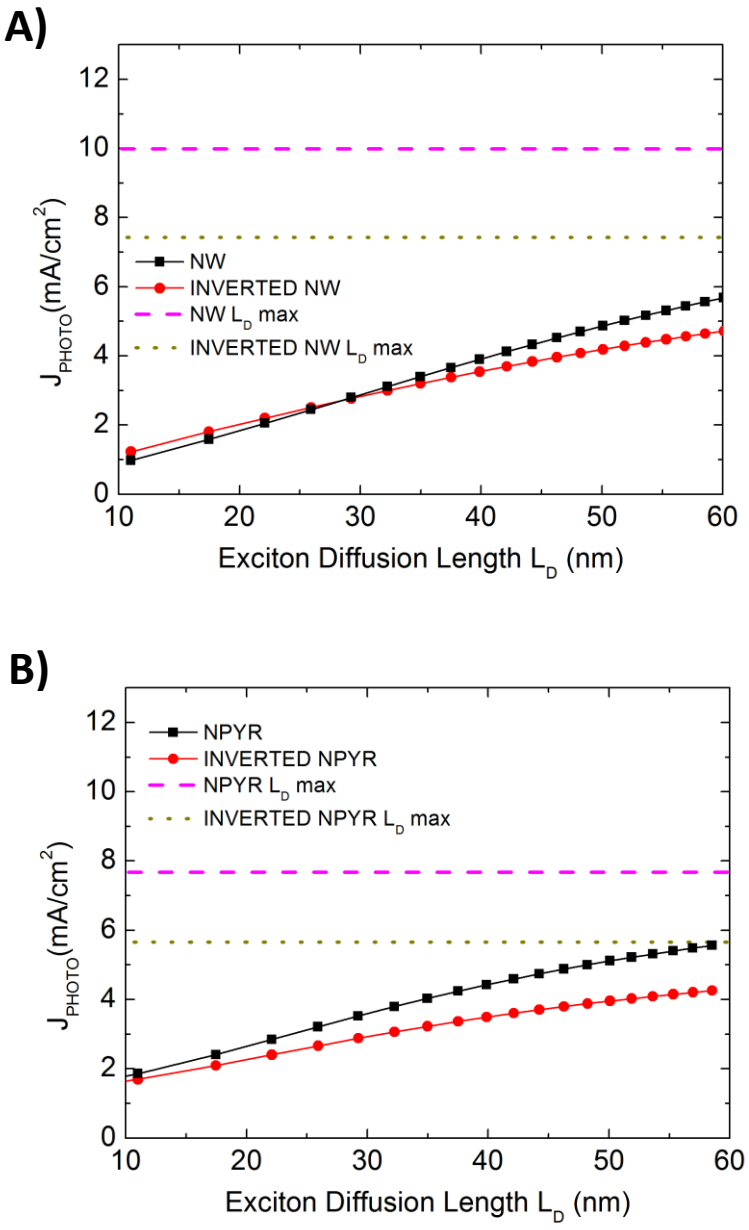

Figure 5.8 *Maximum obtainable photogenerated current density (J_{PHOTO}) as a function of the exciton diffusion length (L_D) for the NW (A) and the NPYR (B) cases. Each graph displays also the maximum possible current density (J_{MAX}) that would be attained in the absence of exciton recombination.*

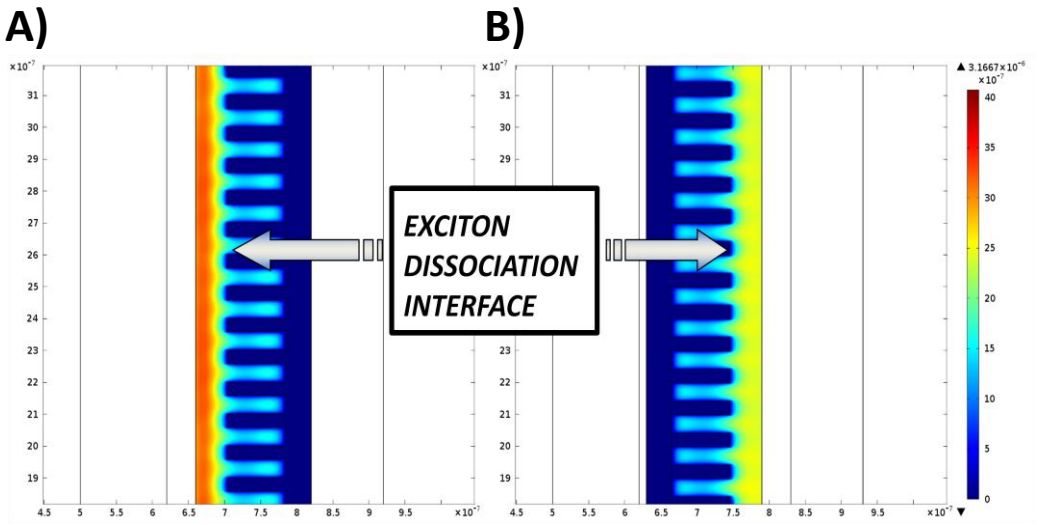

Figure 5.9 *Exciton concentration maps (mol/m^3) for the case of NP for the conventional (A) and the inverted (B) configurations for L_D = 11.02 nm.*

To help to explain the fact that, in most cases, the inverted configuration gives higher photocurrents despite absorbing lower amounts of light, we show in Figure 5.9 the exciton concentration maps. In this figure there is depicted the NP case for the conventional (Figure 5.9A) and the inverted (Figure 5.9B) configurations. It can be seen that the conventional configuration has higher exciton concentrations (warmer colours) due to the higher amount of absorbed light. However, most of these excitons are quite far from the D–A interface, where excitons will dissociate, so the losses due to exciton recombination will be high. Meanwhile, the inverted configuration has lower exciton concentrations, but the exciton concentration close to the dissociation interface is comparable to the conventional case. Hence, the inverted configuration makes better use of the excitons and can generate similar or even higher photocurrents than its conventional equivalent.

5.4.- SUMMARY AND CONCLUSIONS

In this chapter, OSC with different nanostructured Donor–Acceptor junctions have been modelled by applying the developed numerical simulation procedure. By varying the D–A interface geometry, we have performed simulations for planar bilayer (PBL), nanopillars (NP), nanowells (NW) and nanopyramids (NPYR) D–A junctions. Two configurations, the conventional and the inverted one, have been used in this study. A light absorption and exciton diffusion study has been carried out, with the exciton diffusion length (L_D) used as a parameter, to analyze the influence of the D–A junction geometry and the configuration type (conventional or inverted) in the behaviour of the devices.

Results have shown that there is an important reduction of the amount of absorbed light by the active region (P3HT layer) in the inverted configuration if compared with the amount absorbed by the conventional one. This fact can be attributed to the different layer stacking of each configuration. For the conventional case, light arrives to the P3HT layer by only crossing through the ITO and the PEDOT:PSS layers, which are nearly transparent. For the inverted configuration, light have to cross the PCBM layer instead. This material absorbs in a similar range than the P3HT. So the amount of light that arrives to the active region will be lower.

However, the exciton diffusion study have shown that despite absorbing less light, and as a consequence having a lower exciton generation rate, the inverted configuration can generate higher photocurrents in all cases except for the NPYR D–A interface. The exciton concentration maps have shown that for the inverted configuration excitons are distributed in a proper way, i.e close to the D–A interface to dissociated, so losses due to exciton recombination are reduced. This is an interesting fact since the inverted configuration has the advantage of having a higher

UNIVERSITAT ROVIRA I VIRGILI
DESIGN AND MODELLING OF INTERDIGITATED AND NANOSTRUCTURED POLYMER SOLAR CELLS
Pedro Granero Secilla
Dipòsit Legal: T 891-2015

stability and durability when exposed to the oxygen and to the water of the atmosphere without degrading than the conventional one. Hence, this configuration can be a promising solution to increase the efficiency and the lifetime of OSC.

UNIVERSITAT ROVIRA I VIRGILI
DESIGN AND MODELLING OF INTERDIGITATED AND NANOSTRUCTURED POLYMER SOLAR CELLS
Pedro Granero Secilla
Dipòsit Legal: T 891-2015

CHAPTER 6

STUDY OF NANOSTRUCTURED TiO_2 ORGANIC SOLAR CELLS AND PLASMONIC GOLD PYRAMID ARRAYS

The motivation of this chapter is to apply and to adapt the developed numerical simulation method to other devices and structures to demonstrate and to show that it can work correctly not only for the full organic solar cells that we have previously seen. The simulation model is applied to two situations: hybrid solar cells and gold nanosphere pyramids.

UNIVERSITAT ROVIRA I VIRGILI
DESIGN AND MODELLING OF INTERDIGITATED AND NANOSTRUCTURED POLYMER SOLAR CELLS
Pedro Granero Secilla
Dipòsit Legal: T 891-2015

For case of the hybrid solar cell, we have that the active region is a blend of the different organic semiconductors instead of separated materials and has a nanostructured titanium dioxide (TiO_2) electrode. Several modifications of the method presented in Chapter 3 are explained here to adapt the model to this different technology, also with the problems that have appeared and how they have been solved. Simulation results are also compared with experimental data provided from the group of Dr. Monica Lira-Cantu (from the Laboratory of Nanostructured Materials for Photovoltaic Energy, CIN2, Barcelona) for nanostructured and flat TiO_2 layers. A parameter adjust it is also depicted to fully fit the simulation results with the experimental data to complete this adapted simulation model. Finally, we also try to help to understand why one kind of configuration offers a better efficiency and which mechanisms are involved by varying several geometrical parameters of the nanostructured TiO_2 and the P3HT:PCBM layers.

Regarding the gold nanosphere pyramids, we present a work about the simulation of the plasmonic effect in pyramids formed by layers of gold nanospheres. This kind of structures is intended to provide cheap ultrasensitive and ultrafast sensors with surface-enhanced Raman scattering (SERS) spectroscopy as the transducer, in our case, to develop a handheld reversible SERS sensor for the live monitoring of carbon monoxide in the atmosphere. The aim of this study is to demonstrate that the optical part of the simulation procedure introduced in Chapter 3 can be used to model different effects in geometries in the range of the nm so it is not only restricted to solar cells. The basics of this study can also be useful to future work related with the use of metallic nanoparticles in solar cells to enhance its efficiency.

UNIVERSITAT ROVIRA I VIRGILI
DESIGN AND MODELLING OF INTERDIGITATED AND NANOSTRUCTURED POLYMER SOLAR CELLS
Pedro Granero Secilla
Dipòsit Legal: T 891-2015

6.1.- NUMERICAL SIMULATION OF NANOSTRUCTURED TiO_2 ORGANIC SOLAR CELLS

6.1.1.- NANOSTRUCTURED TiO_2 ORGANIC SOLAR CELLS

The hybrid solar cell studied in this section is depicted in Figure 6.1A, where it can be seen that it has the structure ITO/TiO_2/P3HT:PCBM/PEDOT:PSS/Ag. It is therefore an inverted configuration where the ITO/TiO_2 layers act as cathode and the Ag one acts as the anode, similar to the devices studied in Chapter 5. However, there are now two important differences between the cells of this section and the previous analyzed ones: the active region is a blend of the different organic semiconductors instead of separated materials (bulk heterojunction architecture) and the TiO_2 electron collecting layer is nanostructured. The motivation of this nanostructured electrode is to try to increase the device efficiency, if compared with cells with flat TiO_2 layers, by increasing light absorption and improving charge collection.

Several authors have obtained promising results. For instance, Baek *et al.* [Baek2-2009] reported P3HT:PCBM devices with highly ordered nanoporous TiO_2 layers to improve the performance of the cells. The nanostructured devices showed a higher power conversion efficiency if compared with reference ones with flat TiO_2 layers, 1.49% instead of 1.18%. In their conclusions they state that this increase in the efficiency comes from an enhanced charge separation and collection due to the increasing of the interface area between the TiO_2 and the active layer. Their results also showed that light absorption in the nanoporous TiO_2 devices was slightly higher than that on flat ones, especially for wavelengths between 500 and 600 nm.

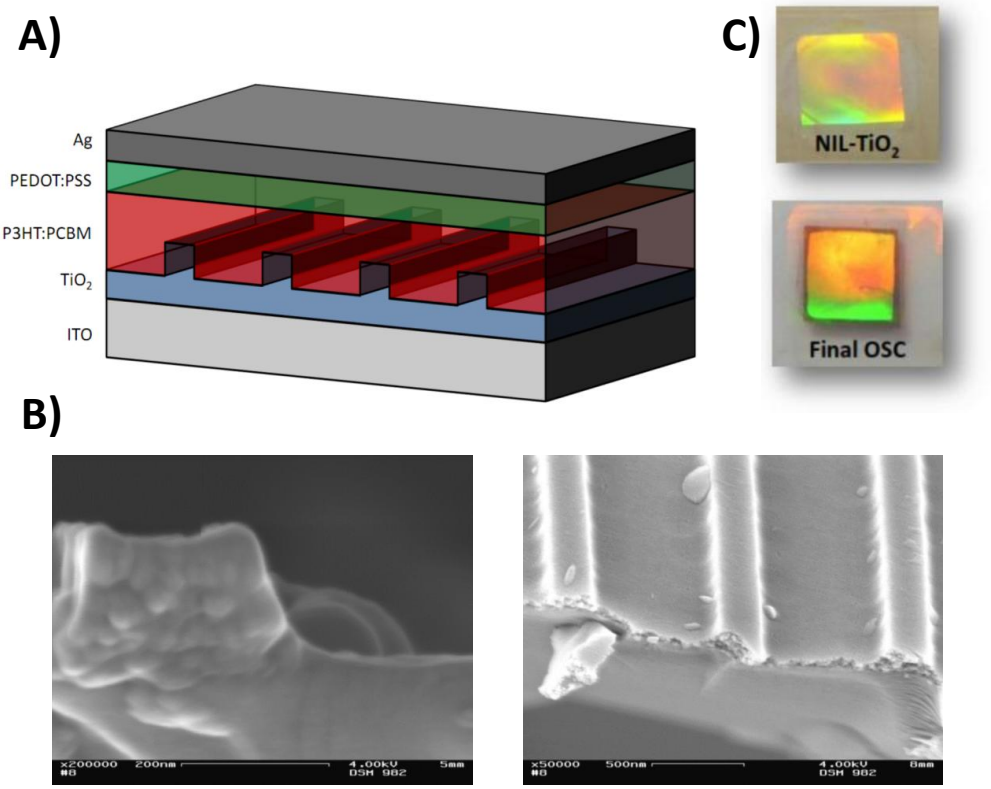

Figure 6.1 *Inverted hybrid nanostructured TiO_2 solar cell studied in this section. Structure scheme (A), scanning electron microscope (SEM) images of the nanoimprint lithography (NIL) TiO_2 layer, and naked eye images of the NIL TiO_2 layer and of a finished cell (C). Courtesy of Dr. Monica Lira-Cantu from the Laboratory of Nanostructured Materials for Photovoltaic Energy, CIN2, Barcelona.*

The research group of Kim *et al.* presented a highly uniform and predesigned zinc oxide (ZnO) nanostructure used as the electron transport layer for inverted bulk heterojunction devices [Kim-2013]. Together with TiO_2, ZnO has shown good results for inverted OSC [Liao-2008]. In Kim *et al.* study, the device configuration was ITO/ZnO/active layer/PEDOT:PSS/Ag, where the ZnO layer followed a groove

UNIVERSITAT ROVIRA I VIRGILI
DESIGN AND MODELLING OF INTERDIGITATED AND NANOSTRUCTURED POLYMER SOLAR CELLS
Pedro Granero Secilla
Dipòsit Legal: T 891-2015

nanopattern. The groove width and height of this layer were 125 nm and 135 nm, respectively, and the period was 800 nm (approximate values). Their results showed that the devices with the nanostructured ZnO layer had always a positive effect on the OSC performance compared with the reference cell with a planar ZnO thin film, including a significant improvement of the J_{sc} and *FF*. However, the V_{oc} remained similar to that of the reference device. Kim *et al.* state that the nanopatterned ZnO layer worked as an improved electron carrier transport path to the ITO electrode by shortening the electron diffusion distance from the active layer, and thus the electron collection efficiency was enhanced.

In our case of study, to manufacture the inverted cell the nanoimprint lithography (NIL) method has been used. In this method, a predefined pattern is replicated into a deformable material coated on a surface. The predefined pattern is usually created on a rigid material (master stamp) that can be used directly, or serve as template from which elastomeric stamps (soft stamps) are molded [Avnon-2011]. In our case, the master stamp is the nanostructured TiO_2 layer (Figure 6.1B), which is not removed since it is a constituent of the device, and the deformable material is the P3HT:PCBM blend. In Figure 6.1C it is shown a naked eye images of the NIL TiO_2 layer and of a finished cell manufactured by the research group of Dr. Monica Lira-Cantu from the CIN2, Barcelona.

Figure 6.2 shows the average current density–voltage (*J*–*V*) curves, from 5 samples, for the flat and the NIL-TiO_2 devices obtained by the research group of Dr. Monica Lira-Cantu from the CIN2 (Barcelona). By comparing the two architectures, it can be seen that the NIL-TiO_2 provides higher currents. However, it seems that there are not significant differences between the two devices for the other parameters, such as the V_{oc} or the *FF*. In Table 6.1 it is depicted the characteristic parameters for the two architectures obtained from the *J*–*V* curves from Figure 6.2. It is also shown the

difference in percentage between the two architectures for each parameter. Indeed, it can be seen that the NIL-TiO_2 devices produce higher currents, while the other parameters only vary slightly. This increase in the J_{sc} leads to higher efficiencies in the nanostructured devices, which achieve an improvement of more than 36% if compared with the flat reference cells.

These results are in good agreement with Kim *et al.* ones [Kim-2013], where the ZnO nanostructured devices achieved higher J_{sc} if compared with the reference planar cell. In both cases, the nanostructured electron transport layer seems to improve the electron carrier transport to the ITO electrode since the increased area shortens the electron diffusion distance from the active layer. So, as a result, higher currents can be achieved. However, an optical enhancement could also be possible in this kind of devices due to light scattering effects. This effect will be analyzed in the following sections.

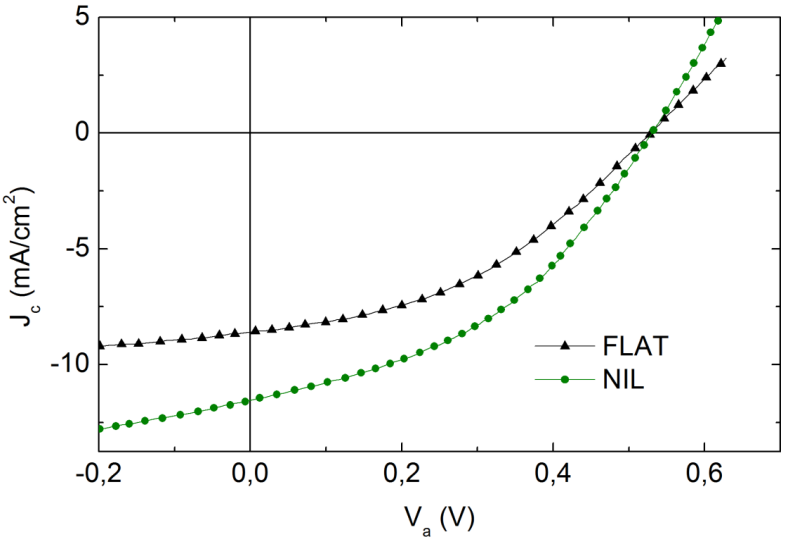

Figure 6.2 *Average current density–voltage (J–V) curves for the flat and the NIL-TiO_2 devices obtained from 5 samples. Courtesy of Dr. Monica Lira-Cantu from the Laboratory of Nanostructured Materials for Photovoltaic Energy, CIN2, Barcelona.*

UNIVERSITAT ROVIRA I VIRGILI
DESIGN AND MODELLING OF INTERDIGITATED AND NANOSTRUCTURED POLYMER SOLAR CELLS
Pedro Granero Secilla
Dipòsit Legal: T 891-2015

PARAMETER	FLAT-TiO_2	NIL-TiO_2	DIFFERENCE (%)
J_{sc} (mA/cm^2)	8.60	11.54	34.17
V_{oc} (V)	0.5278	0.5285	0.13
FF	40.95	41.53	1.44
PCE (%)	1.86	2.53	36.28

Table 6.1 *Characteristic parameters for the flat and the NIL-TiO_2 devices obtained from the J–V curves from Figure 6.2. It is also shown the difference in percentage between the two architectures for each parameter.*

6.1.2.- SIMULATION CONDITIONS AND COMPUTATIONAL DOMAIN

In order to reproduce the experimental results for nanostructured and flat TiO_2 devices and analyze them, the numerical simulation model exposed in Chapter 3 has been used. This procedure has been thought to model OSC where the electron donor and the acceptor materials are actually in two separated regions [Granero-2013]. However in the devices studied in this chapter the active region is a blend of the two organic semiconductors, so some modifications need to be done.

To turn the P3HT/PCBM bilayer into a monolayer blend of P3HT:PCM we have replaced these two layers with only one that will act as the blend. The optical constants of this new layer, the refractive index (n) and the extinction coefficient (k) of the complex index of refraction ($\tilde{n} = n + ik$), have been obtained from the literature [Monestier-2007]. This blend layer will act as a hypothetical semiconductor with the LUMO level of the acceptor (PCBM) and the HOMO level of the donor (P3HT), with the difference between the two energy levels being the bandgap of this

UNIVERSITAT ROVIRA I VIRGILI
DESIGN AND MODELLING OF INTERDIGITATED AND NANOSTRUCTURED POLYMER SOLAR CELLS
Pedro Granero Secilla
Dipòsit Legal: T 891-2015

semiconductor [Koster-2005]. The electrical parameters of the blend, such as the hole and the electron mobilities, have also been taken from published articles [Nakamura-2005; Mihailetchi-2006; Monestier-2007]. As it has been done in Chapter 4 with the experimental validation of interdigitated OSC, these parameters will varied and used to adapt the *J–V* curves to match the *FF* and the shunt and series resistances to the experimental data.

Other modifications of the numerical simulation model refer to the different behaviour that the blend layer has if compared with the bilayer D–A case. In the bulk heterojunction architecture, the donor and the acceptor materials are blended together in an interpenetrating mixture. This fact affects mainly three steps of the solar energy conversion process: the exciton generation, the exciton recombination and the free charge transport.

The total exciton generation rate is obtained at every point of interest of the devices from the amount of absorbed light (*total power dissipation density Q)*. Due to the mixture of the donor and the acceptor materials, in a bulk heterojunction architecture this amount of absorbed light needs to be considered in the entire blend. So, at any position $\vec{r}$ in the structure, such magnitude $Q(\vec{r};\lambda)$, in W/m^3, for a monochromatic wave of wavelength λ is defined as follows:

$$Q(\lambda) = \int_{BLEND} Q(\vec{r};\lambda) dV \,. \tag{6.1}$$

Then, by summing it for all the considered wavelengths, we obtain the total light absorption of a device for the incident light source:

UNIVERSITAT ROVIRA I VIRGILI
DESIGN AND MODELLING OF INTERDIGITATED AND NANOSTRUCTURED POLYMER SOLAR CELLS
Pedro Granero Secilla
Dipòsit Legal: T 891-2015

$$Q_{Total} = \sum_i Q(\lambda_i). \tag{6.2}$$

Ideally, in a bulk heterojunction cell all the generated excitons will be able to dissociate by finding the D–A interface before recombine since distances are lower that the main exciton diffusion lengths of the materials. To model this effect the *exciton diffusion equation* can be modified by removing the recombination term. Hence the exciton density as a function of time at a position $\vec{r}$ will be set now as follows:

$$\frac{\partial exc}{\partial t} = D_{exc} \frac{\partial exc^2}{\partial \vec{r}^2} + \sum_i \left(\frac{Q(\vec{r}; \lambda_i)}{hc / \lambda_i} \right) \tag{6.3}$$

Finally, for the case of the bulk heterojunction approach, free charges can travel through the entire active region since the blend acts as a semiconductor with good hole and electron mobilities. This did not happen in the previous case, where each kind of semiconductor had a good hole or a good electron mobility but not both.

Regarding the computational domain, Figure 6.3 shows a scheme of the two models, with the structure ITO/TiO_2/P3HT:PCBM/PEDOT:PSS/Ag, used in the simulations: the NIL-TiO_2 and the FLAT-TiO_2. Our model is a 2D simplification of a real 3D device. Since the NIL TiO_2 layer is nanostructured in the form of interpenetrating grooves, this simplification will be accurate enough. The values of the geometrical parameters, the size of the nanostructured TiO_2 region and the layers thicknesses, have been estimated from scanning electron microscope (*SEM*) pictures provided by Dr. Monica Lira-Cantu from the CIN2 (Barcelona). T_{FLAT}, T_{NIL}, W_{NIL}, B_{TiO2} and P_{TiO2} are defined as variables that will take different ranges of values in the simulation analysis of the

following sections. The initial values for these geometrical parameters to reproduce the experimental results of the NIL and the flat devices are shown in Table 6.2.

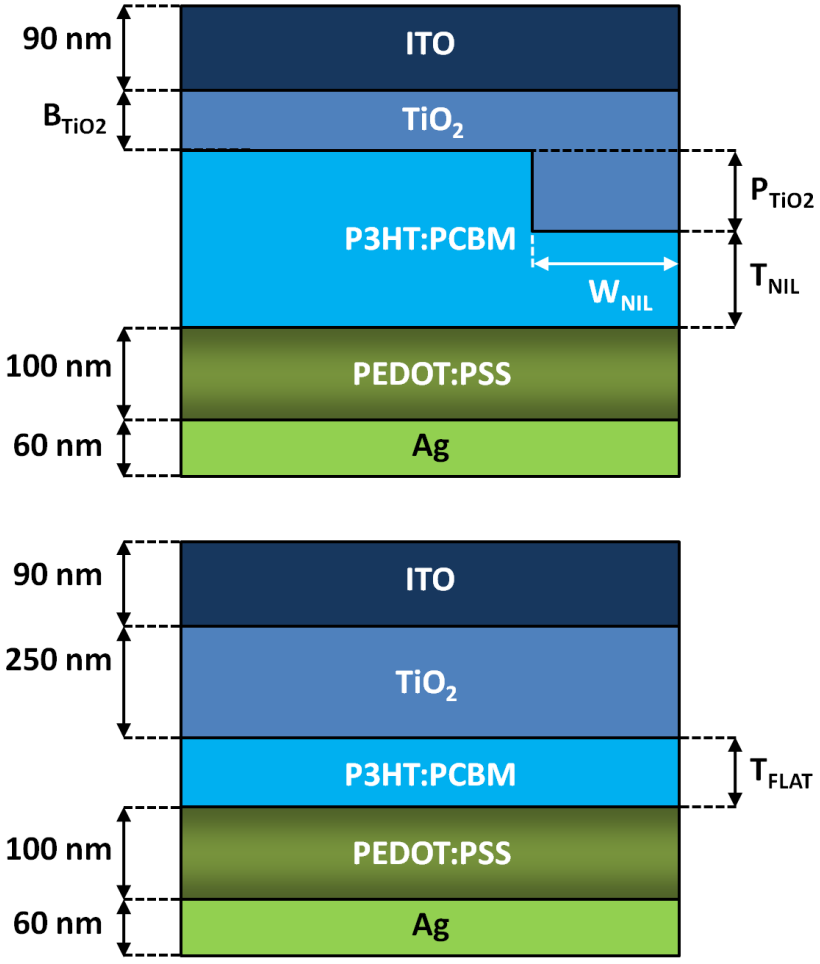

Figure 6.3 *Schematic drawing of the models used in the simulations. The values of the geometrical parameters have been estimated from scanning electron microscope (SEM) pictures provided by Dr. Monica Lira-Cantu from the CIN2 (Barcelona).* T_{FLAT}, T_{NIL}, W_{NIL}, B_{TiO2} *and* P_{TiO2} *are defined as variables that will take different ranges of values in next section. The period of the nanostructured* TiO_2 *is 1 µm.*

UNIVERSITAT ROVIRA I VIRGILI
DESIGN AND MODELLING OF INTERDIGITATED AND NANOSTRUCTURED POLYMER SOLAR CELLS
Pedro Granero Secilla
Dipòsit Legal: T 891-2015

PARAMETER	*SIZE (nm)*
B_{TiO2}	*50 nm*
P_{TiO2}	*200 nm*
W_{NIL}	*200 nm*
T_{NIL}	*200 nm*
T_{FLAT}	*200 nm*

Table 6.2 *Initial values for the geometrical parameters of the P3HT:PCMB and the TiO_2 layers to reproduce the experimental results of the NIL and the flat devices.*

6.1.3.- SIMULATION RESULTS OF FLAT AND NANOSTRUCTURED TiO_2 OSC

The simulation analysis of the flat and the NIL-TiO_2 OSC is divided into two parts. The first one consists in to reproduce the experimental results and, by adjusting several parameters, to adapt the *J–V* curves to match the simulation results with the experimental data. In the second part, several geometrical parameters of the nanostructured TiO_2 and the P3HT:PCBM layers are varied in order examine their influence on the device properties.

6.1.3.1.- EXPERIMENTAL RESULTS REPRODUCTION

As it has been done in Chapter 4 with the experimental validation of interdigitated OSC, the free charge mobilities had been used to adapt the *J–V* curves to match the simulation results with the experimental data. By varying these electrical parameters,

UNIVERSITAT ROVIRA I VIRGILI
DESIGN AND MODELLING OF INTERDIGITATED AND NANOSTRUCTURED POLYMER SOLAR CELLS
Pedro Granero Secilla
Dipòsit Legal: T 891-2015

it is possible to modify the form of the *J–V* curve, specially the knee, and the amount of current density that can be extracted from the device. This allows adapting the curve to match the *FF* and the J_{sc} to the experimental data.

The hole mobility in P3HT can range from 10^{-5} to 10^{-2} $cm^2/(V \cdot s)$, with a typical value of $2 \cdot 10^{-4}$ $cm^2/(V \cdot s)$, and the electron mobility in PCBM can range from $2 \cdot 10^{-3}$ to $2 \cdot 10^{-2}$ $cm^2/(V \cdot s)$, with a typical value of $3 \cdot 10^{-3}$ $cm^2/(V \cdot s)$ [Monestier-2007]. After the fitting process, the final used values were:

- **Hole mobility in P3HT:PCBM** = $6 \cdot 10^{-5}$ $cm^2/(V \cdot s)$
- **Electron mobility in P3HT:PCBM** = $6 \cdot 10^{-4}$ $cm^2/(V \cdot s)$

As it can be observed, the obtained values for each mobility are an order of magnitude lower than the obtained for the case of the interdigitated devices (hole mobility in P3HT = $2 \cdot 10^{-4}$ $cm^2/(V \cdot s)$ and electron mobility in PCBM = $3 \cdot 10^{-3}$ $cm^2/(V \cdot s)$). However, the hole and the electron mobilities of the materials in blend form are expected to be lower than in pure materials [Nakamura-2005], so these values are in concordance.

Finally, Figures 6.4 and 6.5 show the average current density–voltage (*J–V*) curves of the analyzed experimental (green circles) and the resulting simulated (black triangles) FLAT-TiO_2 and NIL-TiO_2 OSC devices, respectively.

UNIVERSITAT ROVIRA I VIRGILI
DESIGN AND MODELLING OF INTERDIGITATED AND NANOSTRUCTURED POLYMER SOLAR CELLS
Pedro Granero Secilla
Dipòsit Legal: T 891-2015

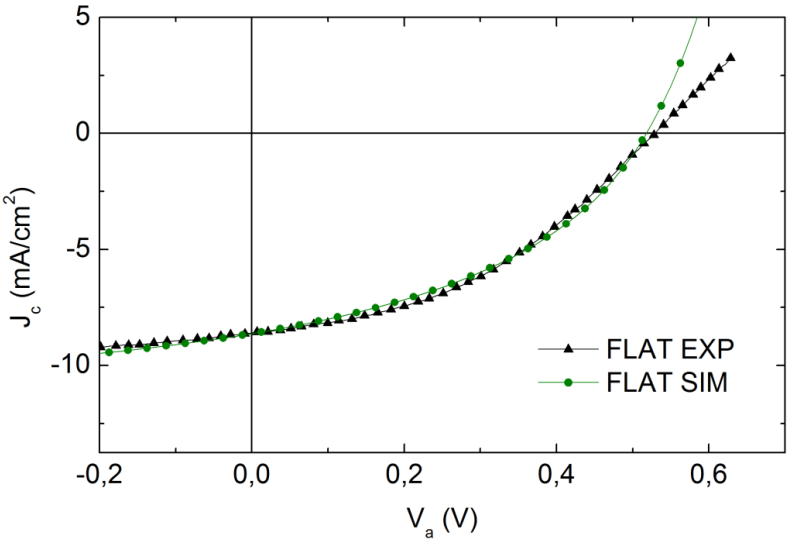

Figure 6.4 *Average current density–voltage (J–V) curve of the analyzed experimental FLAT-TiO_2 OSC (green circles) (Courtesy of Dr. Monica Lira-Cantu from the CIN2, Barcelona), and the simulation reproduction (black triangles).*

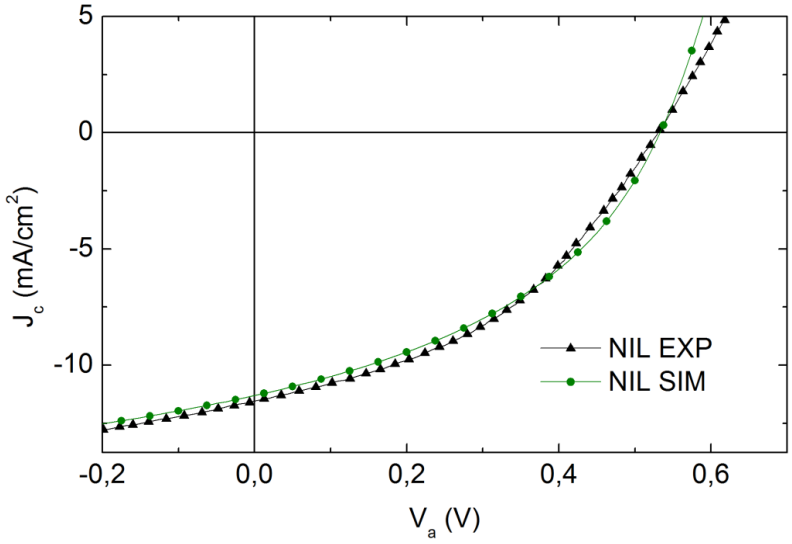

Figure 6.5 *Average current density–voltage (J–V) curve of the analyzed experimental NIL-TiO_2 OSC (green circles) (Courtesy of Dr. Monica Lira-Cantu from the CIN2, Barcelona), and the simulation reproduction (black triangles).*

PARAMETER	FLAT-TiO_2 EXP	FLAT-TiO_2 SIM	NIL-TiO_2 EXP	NIL-TiO_2 SIM
J_{sc} (mA/cm^2)	8.60	8.63	11.54	11.37
V_{oc} (V)	0.5278	0.5130	0.5285	0.5250
FF	40.95	41.27	41.53	41.20
PCE (%)	1.86	1.82	2.53	2.46

Table 6.3 *Average characteristic parameters of the experimental FLAT-TiO2 and NIL-TiO2 devices and the ones obtained via simulation.*

By observing these two figures, it can be seen that for both configurations the fitting of the simulation results with the experimental data is quite good. Current densities match for most of the considered applied voltages (V_a). However the fitting for $V_a > V_{oc}$ is less accurate, having little differences between curves, especially in the case of the FLAT-TiO_2. Nevertheless, the global fitting seems to be accurate enough. In Table 6.3 it can be seen the average characteristic parameters of the experimental FLAT-TiO_2 and NIL-TiO_2 devices and the ones obtained via simulation. Due to the good *J–V* curve fitting, none of the parameters from the simulations have a relative error (Equation 6.4) above the 3% if compared with the experimental ones.

$$Relative\ error = \frac{simulated - experimental}{experimental} \cdot 100 \tag{6.4}$$

6.1.3.2.- OPTICAL AND ELECTRICAL ANALYSIS

In this section, several geometrical parameters of the nanostructured TiO_2 and the P3HT:PCBM layers are varied in order examine their influence on the device

properties and response. The parameters of interest are T_{FLAT}, T_{NIL}, W_{NIL}, B_{TiO2}, and P_{TiO2}, which have been defined as variables when the devices structure was defined in the computational domain (see Figure 6.3). The simulation study includes light absorption, exciton diffusion, and electrical simulations of several FLAT-TiO_2 and NIL-TiO_2 devices.

The ranges of values for the geometrical parameters have been chosen on the basis of *SEM* estimates from actual devices provided by Dr. Monica Lira-Cantu from the CIN2 (Barcelona). For two of the geometrical parameters, i) the thickness of the P3HT:PCBM layer in FLAT-TiO_2 devices (T_{FLAT}) and ii) the thickness of the base P3HT:PCBM layer in NIL-TiO_2 devices (T_{NIL}), the simulations have been carried out for a range of values. The chosen range for T_{FLAT} has been from 135 nm to 155 nm, while for T_{NIL} the range was from 145 nm to 170 nm. Besides, simulations for two different values of the width of the P3HT:PCBM grooves have been considered, W_{NIL} = 270 nm and W_{NIL} = 280 nm. For each of these values, corresponding dimensions for the thicknesses B_{TiO2} and P_{TiO2} have been used, as indicated in Table 6.4.

The incident light is assumed to be normal to the device surface and incident from the ITO side. It has been modelled as the superposition of a set of monochromatic linear polarized waves with a planar wavefront. The amplitudes of these plane waves follow the standard AM1.5 spectral distribution of the solar radiation. To obtain the complete spectrum, simulations have been carried out for wavelengths in the range from 280 to 700 nm in intervals of 10 nm. This wavelength range corresponds to the absorption spectrum of P3HT, which is the material where most of the excitons are generated [Burkhard-2009].

PARAMETER	W_{NIL} = 270 nm	W_{NIL} = 280 nm
B_{TiO2}	75 nm	100 nm
P_{TiO2}	75 nm	50 nm
T_{NIL}	145 nm – 170 nm	145 nm – 170 nm

Table 6.4 *Values of the nanostructured TiO_2 thicknesses for the two considered groove widths. The period of the nanostructured TiO_2 is 1080 nm.*

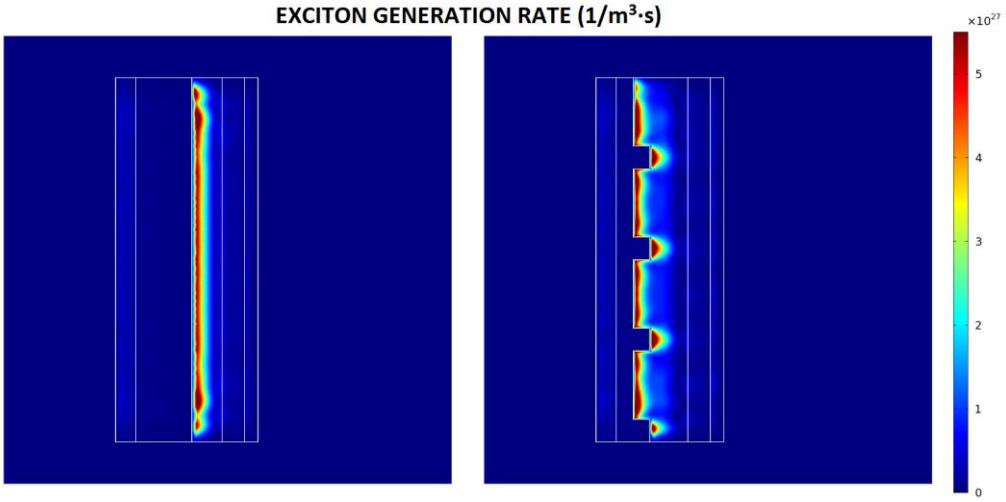

Figure 6.6 *Exciton generation rate for two of the considered structures, one flat (left) and one NIL (right). The nanostructured interface permits more excitons, and carriers, to be generated near it.*

The first step to analyze the behaviour of the devices is to obtain the amount of absorbed light as a function of the position. With this, the exciton generation rate can be calculated, since both magnitudes are directly related. The exciton generation rate obtained with the finite-element method for two of the simulated structures, one flat (T_{FLAT} = 135 nm) and one NIL (T_{NIL} = 170 nm, W_{NIL} = 270 nm, B_{TiO2} = 75 nm, and P_{TiO2} = 75 nm), is depicted in Figure 6.6. In the structures, light is incident from the left on the

UNIVERSITAT ROVIRA I VIRGILI
DESIGN AND MODELLING OF INTERDIGITATED AND NANOSTRUCTURED POLYMER SOLAR CELLS
Pedro Granero Secilla
Dipòsit Legal: T 891-2015

ITO layer. In both cases, it is shown that the carriers are mainly generated near the TiO_2-blend interface. This is due to the strong absorption of the blend that attenuates light away from such interface. Because of the nanostructured geometry of the TiO_2, the interface area is increased and consequently a greater amount of carriers is generated near the interface. It also can be seen that the NIL-TiO_2 cell achieves a higher exciton generation rate than the FLAT-TiO_2 near the TiO_2-blend interface (warmer colours), which comes from a higher light absorption.

By solving the *exciton diffusion equation*, the maximum attainable photogenerated current density (J_{PHOTO}) can be obtained. Figure 6.7 shows J_{PHOTO} as a function of the geometrical parameters for the different cells. As it can be seen, as the thickness of the P3HT:PCBM layer increases, the J_{PHOTO} slightly improves for both the flat and the NIL cells. This result can be explained by the fact that this magnitude takes only into account the generation of carriers, directly related to the absorption of light. Thus, a bigger thickness, T_{FLAT} or T_{NIL}, is translated in a bigger amount of absorbed photons. However, the influence of the thicknesses T_{FLAT} or T_{NIL} on the J_{PHOTO} is small, especially for the NIL structures. It has to be noted that the two horizontal axes (top and bottom) are in the same scale. For all the considered cases, the NIL structures show a better J_{PHOTO}. This demonstrates that the nanostructuring of the ITO and of the blend layer helps increasing the amount of absorbed photons. The difference in J_{PHOTO} between the two structures, for the considered parameter ranges, is up to 23.34%.

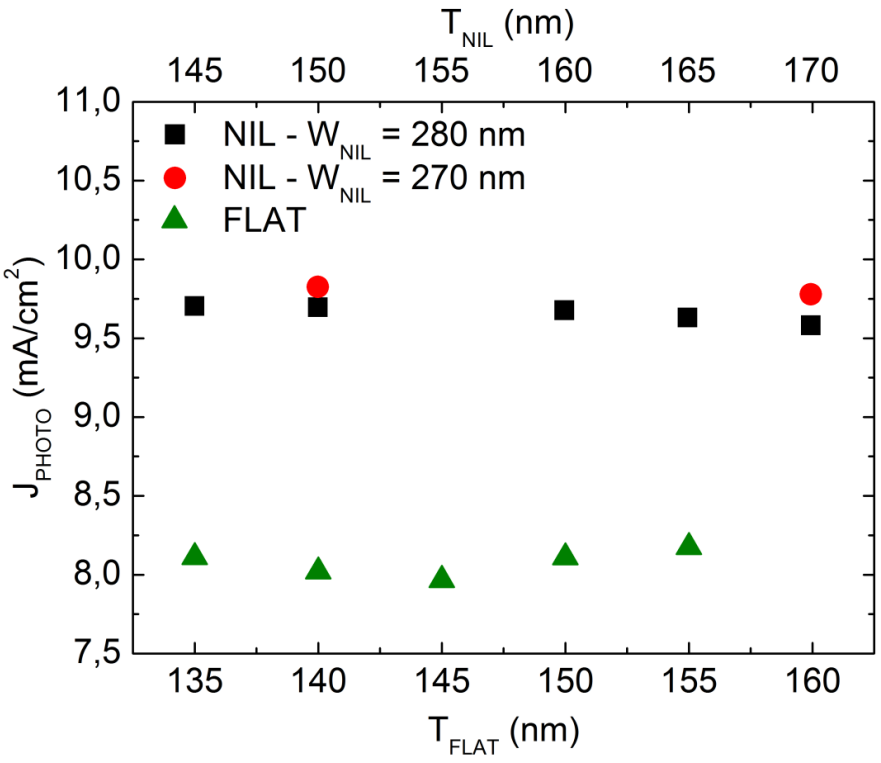

Figure 6.7 *Maximum attainable photogenerated current density (J_{PHOTO}) as a function of the blend thickness for the flat and the NIL structures.*

Finally, to obtain the complete current density–voltage (*J–V*) characteristics, the drift-diffusion model is applied. Figure 6.8 shows the *J–V* curves of two cells, one flat (T_{FLAT} = 150 nm) and one NIL (T_{NIL} = 150 nm, W_{NIL} = 270 nm, B_{TiO2} = 75 nm, and P_{TiO2} = 75 nm). The two curves have a similar *Fill Factor* (45.69 for the flat cell and 43.02 for the NIL one), thus indicating that this factor is not substantially affected by the nanostructuring of the TiO_2. However, there is an increase in the short-circuit current (J_{SC}), and equivalently in efficiency, of 33.13%. This increase can be attributed to two effects of the nanostructured interface: the increase in the number of absorbed photons discussed above, and also the increase of interface area that improve carriers collection.

UNIVERSITAT ROVIRA I VIRGILI
DESIGN AND MODELLING OF INTERDIGITATED AND NANOSTRUCTURED POLYMER SOLAR CELLS
Pedro Granero Secilla
Dipòsit Legal: T 891-2015

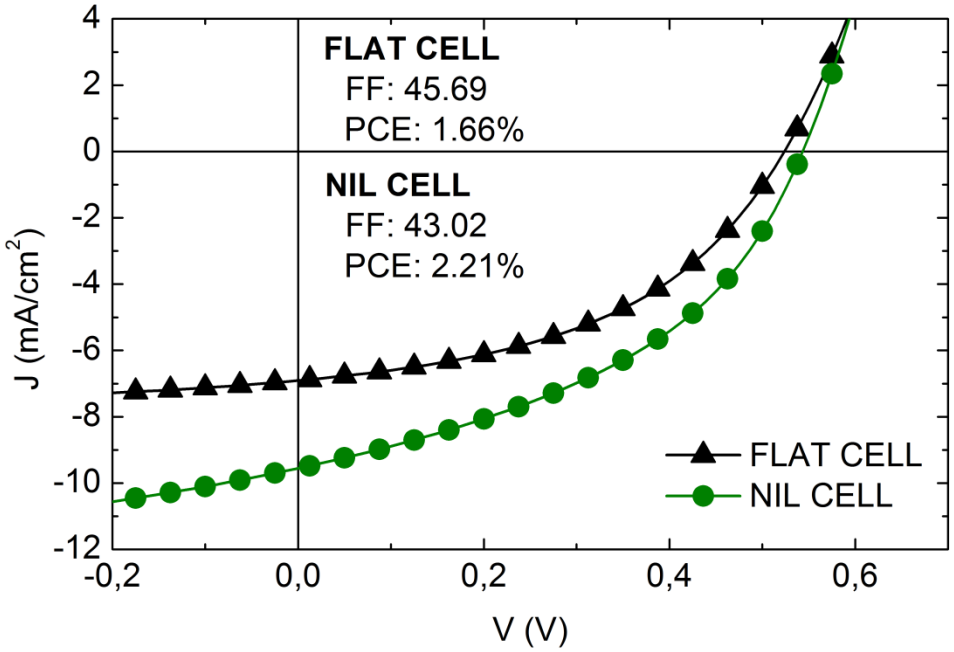

Figure 6.8 *J–V curves of two cells, one flat (T_{FLAT} = 150 nm) and one NIL (T_{NIL} = 150 nm, W_{NIL} = 270 nm, B_{TiO2} = 75 nm, and P_{TiO2} = 75 nm).*

In order to confirm this point, Figure 6.9 shows the calculated J_{SC} for the different cells. In contrast with the J_{PHOTO}, this magnitude shows a decrease with increasing T_{FLAT} or T_{NIL}, with a bigger decrease rate for the flat structure. The decrease is explained by the fact that, even though there is an increase in generated carriers, these carriers are generated further from the TiO_2-blend interface causing a decrease in their collection efficiency. This result demonstrates that the nanostructuring of the TiO_2 helps improving the charge collection efficiency. This improvement can be quantified by the ratio J_{SC}/J_{PHOTO}, represented in the inset of Figure 6.9. In the graph it is clear that, for all the considered geometries, the collection efficiency of the NIL-TiO_2 devices is better than in the FLAT-TiO_2 configurations.

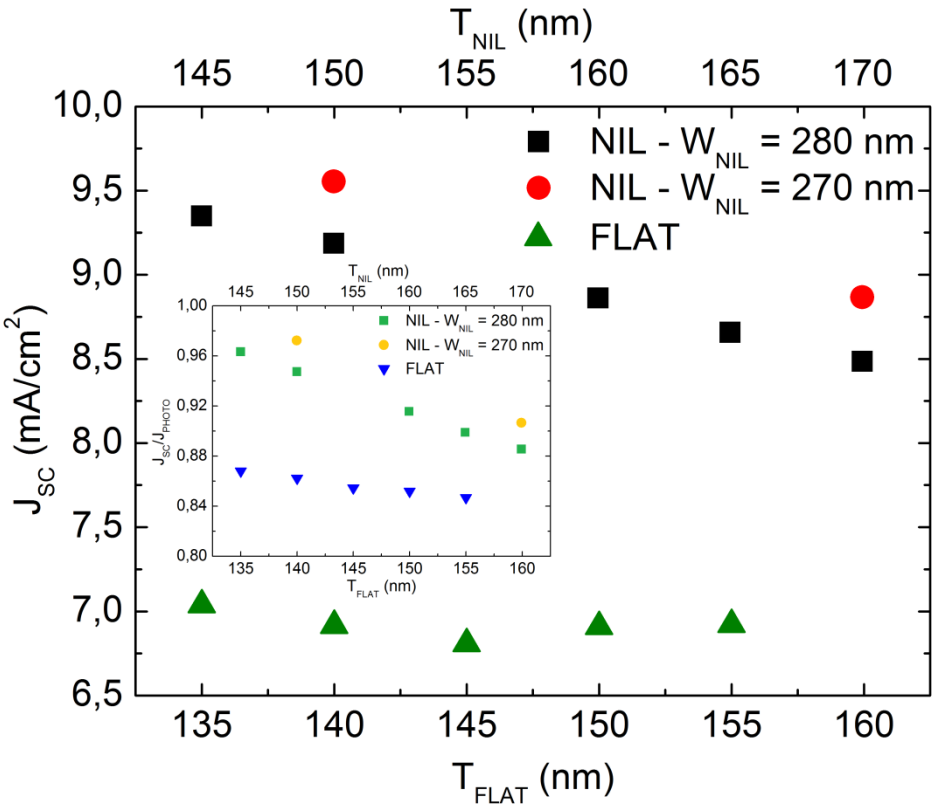

Figure 6.9 *Short-circuit current density (J_{SC}) as a function of the blend thickness for the flat and the NIL devices. The inset shows the ratio J_{SC}/J_{PHOTO} for the same considered devices.*

6.2.- NUMERICAL SIMULATION OF PLASMONIC GOLD PYRAMID ARRAYS

6.2.1.- PLASMONIC GOLD PYRAMID ARRAYS

The surface plasmon resonance (SPR) is an optical phenomenon which occurs when the collective coherent oscillations of free electrons in the conduction band of a metal are excited by the interactive electromagnetic field at a metal/dielectric interface. The

UNIVERSITAT ROVIRA I VIRGILI
DESIGN AND MODELLING OF INTERDIGITATED AND NANOSTRUCTURED POLYMER SOLAR CELLS
Pedro Granero Secilla
Dipòsit Legal: T 891-2015

resonance condition is established when the frequency and momentum of light photons matches the natural frequency and momentum of surface electrons oscillating against the restoring force of positive nuclei. The created charge density oscillations, called surface plasmon polaritons (SPPs), will then form an electric field that exponentially decays into its surrounding medium with a penetration depth in hundreds of nanometers range. As a result, this evanescent field is highly sensitive towards the refractive index change of the surrounding medium. Thus, when the refractive index of the sensing medium changes the SPR excitation occurs for slightly different characteristics of the incident beam, such as the angle, the wavelength, or the phase [Maier-2007; Zeng-2014].

SPR is the basis of many standard tools for measuring adsorption of material onto planar metal (typically gold and silver) surfaces or onto the surface of metal nanoparticles (localized SPR, LSPR). It is the fundamental principle behind many colour-based biosensor applications and different lab-on-a-chip sensors. SPR sensors are the most commonly used optical sensors due to their unique ability for real-time monitoring the molecular binding events [Hoa-2007; Shalabney-2011; Bedford-2012]. However, their sensitivities are insufficient to detect trace amounts of small molecular weight molecules such as cancer biomarkers, hormones, antibiotics, insecticides, and explosive or dangerous materials which are important for early-stage disease diagnosis, food quality control, environmental monitoring, and homeland security protection [Zeng-2014]. To overcome this issue of the SPR sensors, many sensitivity enhancement methods have been proposed [Zeng-2014]. Among others, the surface-enhanced Raman scattering (SERS) spectroscopy has proved to be orders of magnitude more sensitive than normal Raman spectroscopy. The enhancement factor can be as high as 10^9-10^{10}, which means that with this technique it is possible to detect single molecules [Stiles-2008].

The fundamental requirement for SERS is a substrate that supports a surface plasmon resonance. However, not all the possible substrates are acceptable. The ability to control the shape and orientation of nanoparticles on a surface has reduced many of the complex variables related to SERS and has greatly enhanced both the understanding and the application of this phenomenon. So now it is known that it is necessary a highly organized photonic structure, that provides a high electromagnetic field enhancement in a reproducible geometry, to obtain a maximum signal enhancement [Stiles-2008; Alvarez-Puebla-2011]. Many surfaces have being reported during the past few years [Félidj-2004; Aroca-2005; Baker-2005; Kneipp-2006]. Other examples of the fabrication of organized particles have also been reported, such as the use of preformed colloids to create large crystalline organized entities known as supercrystals [Alvarez-Puebla-2011; Henzie-2012; Pazos-Perez-2012].

The latter approach provides optical platforms with unprecedented plasmonic properties that can be exploited for the design of cheap ultrasensitive and ultrafast sensors with SERS spectroscopy as the transducer. In our case of study, a template-assisted method based on the stamping of colloidal particles for the large-area fabrication of organized pyramidal supercrystal periodical arrays is used. This plasmonic platform is then exploited for the development of a handheld reversible SERS sensor for the live monitoring of carbon monoxide (CO) in the atmosphere [Alba-2013]. The method used for the preparation of the nanostructured pyramidal arrays is illustrated in the Figure 6.10.

UNIVERSITAT ROVIRA I VIRGILI
DESIGN AND MODELLING OF INTERDIGITATED AND NANOSTRUCTURED POLYMER SOLAR CELLS
Pedro Granero Secilla
Dipòsit Legal: T 891-2015

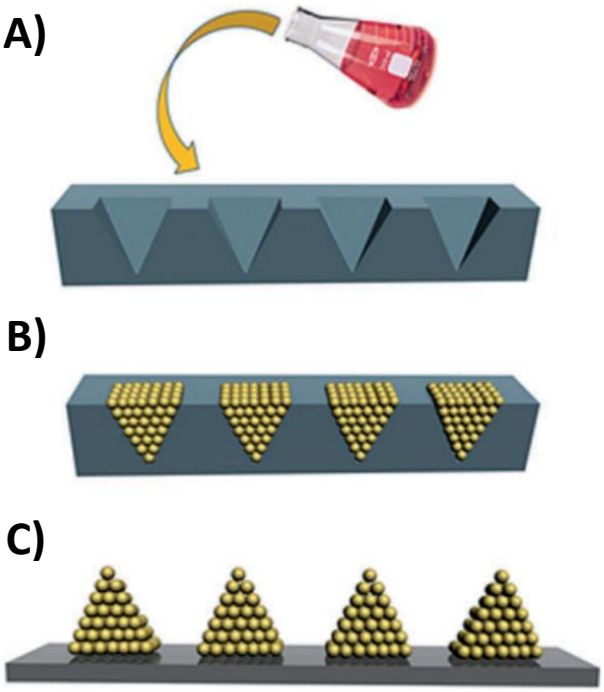

Figure 6.10 *Schematic representation of the fabrication of the macroscale nanostructured pyramidal arrays. Reproduced from [Alba-2013].*

First, inverted pyramidal templates are prepared by direct laser writing lithography on oxidized p-type silicon wafers, followed by a chemical etching process. This method produces periodically patterned surfaces with homogenous inverted pyramids with geometrical features that can be tuned from 1 to 10 µm as a function of the etching time. In this study, pyramids with sides of 4.5 µm and a height of 3.3 µm have been generated with a periodicity of 8 µm. Before the deposition of the nanoparticles (NPs), the surfaces are cleaned with oxygen plasma. A concentrated solution of gold NPs is then cast on the template and allowed to dry. Finally, the NPs are transferred to the surface of poly(dimethylsiloxane) films to yield a periodic array of square pyramids derived from the compact packing of plasmonic particles. Final results show

UNIVERSITAT ROVIRA I VIRGILI
DESIGN AND MODELLING OF INTERDIGITATED AND NANOSTRUCTURED POLYMER SOLAR CELLS
Pedro Granero Secilla
Dipòsit Legal: T 891-2015

nanoparticles pyramids, with high homogeneity in all directions, with side lengths of 4.4 µm and a height of 3.0 µm, as it can be seen in Figure 6.11.

The aim of this section is to reproduce, through numerical simulations, qualitatively the plasmonic effect in the pyramids formed by layers of gold nanospheres that has been demonstrated experimentally. With this, it could be tested if the optical part of the simulation procedure explained in Chapter 3 can be used to model different effects in geometries in the range of the nm so it is not only restricted to solar cells.

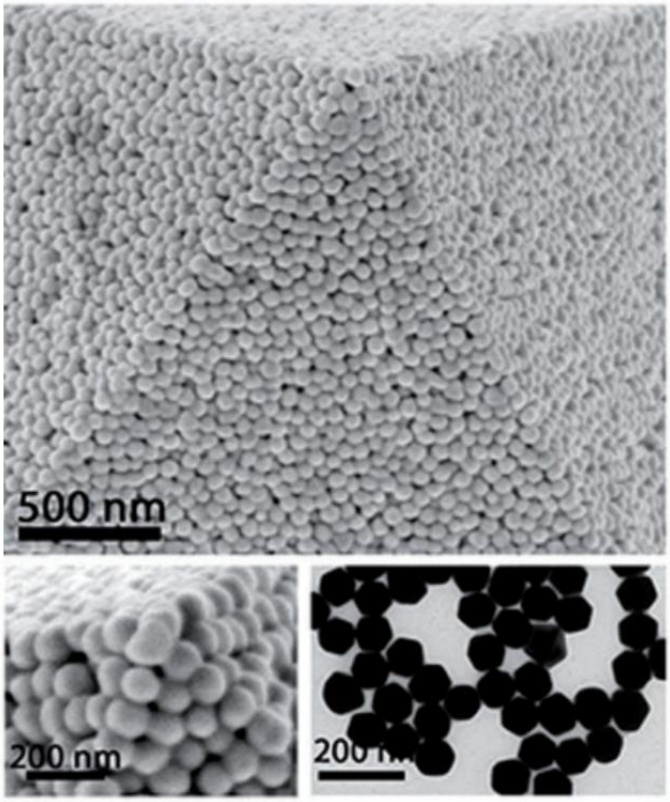

Figure 6.11 *High-resolution scanning electron microscope (SEM) images of the gold nanosphere pyramids, and transmission electron microscopy (TEM) image of the gold nanoparticles building blocks. Reproduced from [Alba-2013].*

UNIVERSITAT ROVIRA I VIRGILI
DESIGN AND MODELLING OF INTERDIGITATED AND NANOSTRUCTURED POLYMER SOLAR CELLS
Pedro Granero Secilla
Dipòsit Legal: T 891-2015

6.2.2.- SIMULATION CONDITIONS AND COMPUTATIONAL DOMAIN

Our optical study has been carried out on the basis of finite-element simulations with the COMSOL Multiphysics® software presented in Chapter 3. Previous studies have demonstrated that the finite-element method allows computing plasmonic effects in nanoparticles with a good accuracy [McMahon-2009; Repän-2014]. The COMSOL RF module [COMSOL RF-2010] has been used to solve the complete Maxwell equations by considering the optical constants of the involved materials as a function of the wavelength and by using the scattered field formulation [Repän-2014]. In our case we have modelled the optical features of the gold nanoparticles by using the refractive index (n) and the extinction coefficient (k) of the complex index of refraction ($\tilde{n} = n + ik$) obtained from literature [Palik-1985]. The surrounding medium has been considered to be air with a constant $n = 1$.

The simulated structure of this section reproduces the top part of one gold nanosphere pyramid, that is the higher layers of nanospheres. We chose to model the last four ones. To follow the shape of the pyramids used experimentally [Alba-2013], the peak of the pyramid has to form an angle of 54.74°. With this constrain, related pyramid heights and side lengths can be fixed. In this study, two kinds of nanospheres distributions have been analyzed: a contacting and a non-contacting one (Figure 6.12). In the contacting distribution, the gold nanospheres are touching each other. On the other hand, in the non-contacting distribution there is a distance between nanospheres of 30 nm (x and y direction). Taking into account the angle that the pyramid peak have to form, the pyramid height and side length of four layers of nanospheres have to be 220.4 nm and 280 nm, respectively, for the contacting distribution. For the non-contacting distribution case the pyramid height and side length are 280 nm and 370 nm, respectively. In both distributions the spheres diameter has been set to 70 nm. An additional simulation structure has been

described, to check the validity of the simulations, for the simple case of the plasmonic effect in only one sphere of 50 nm.

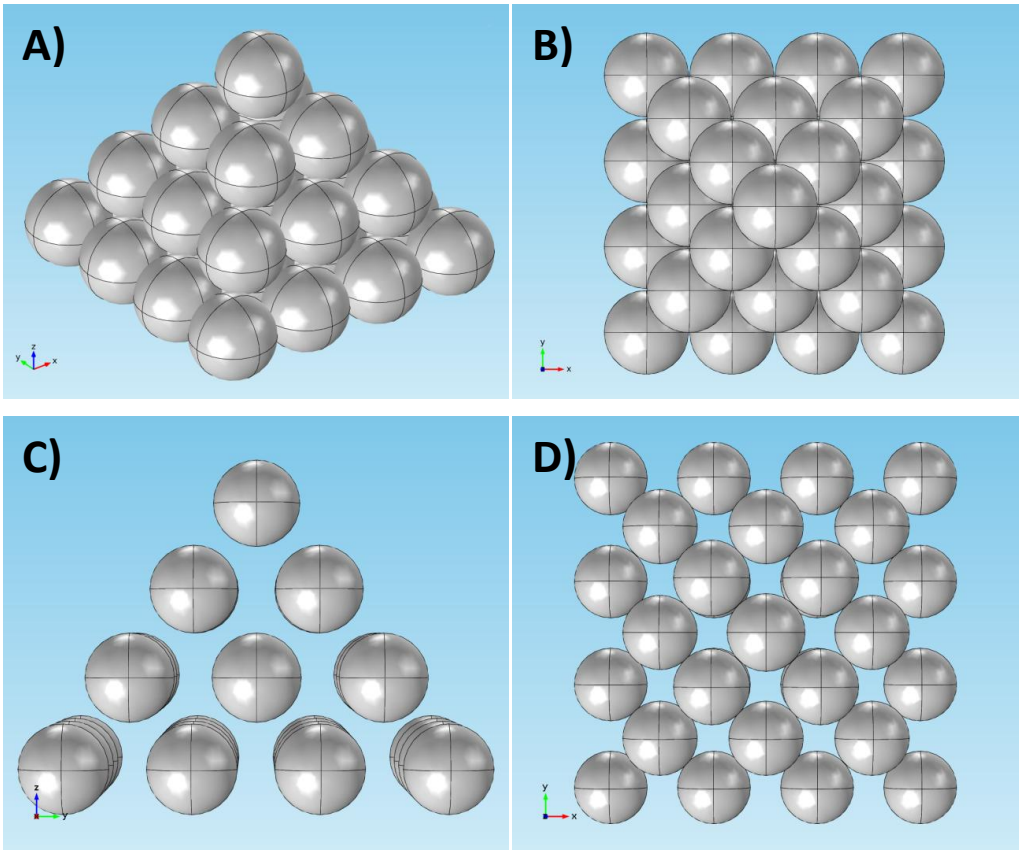

Figure 6.12 *Computational domain showing the four top layers of the gold nanosphere pyramids for the side face (A) and the top view (B) of the contacting distribution, and for the side face (C) and the top view (D) of the non-contacting distribution.*

The incident light in the experimental study is a laser line excitation (λ_{exc}) with wavelengths of 633 nm and 785 nm. In the simulations, this light source has been

modelled with linear monochromatic polarized waves with a planar wavefront parallel to the z axis with a different wavelength for each case. In all cases the light comes from above, reaching first the top of the pyramid.

6.2.3.- SIMULATION RESULTS OF SINGLE NANOSPHERE PYRAMIDS

6.2.3.1.- METHOD VALIDATION: SINGLE SPHERE CASE

Light incident on small metal nanoparticles can excite collective excitations of electrons, which is the localised surface plasmon resonance (LSPR) mentioned above. Typically, these excitations consist on dipolar oscillations, as it can be seen in Figure 6.13 [Maier-2007]. Figure 6.14 shows the simulation results for one isolated gold nanosphere with a diameter of 50 nm for an incident light with a wavelength of 575 nm. In these maps of the amplitude of the electric field, $|E|$, it can be appreciated the expected theoretical dipole due to the plasmonic effect. It also can be seen that the results for the cross (Figure 6.14A) and the top sections (Figure 6.14B) are very similar. This effect can be attributed to the spherical symmetry of the gold nanoparticle. From these results it can be concluded that the applied numerical simulation method is able to reproduce, at least in a qualitatively way, the plasmonic effect in a metal nanoparticle. Hence, it can be expected that the following simulations of gold nanosphere pyramids will be correct.

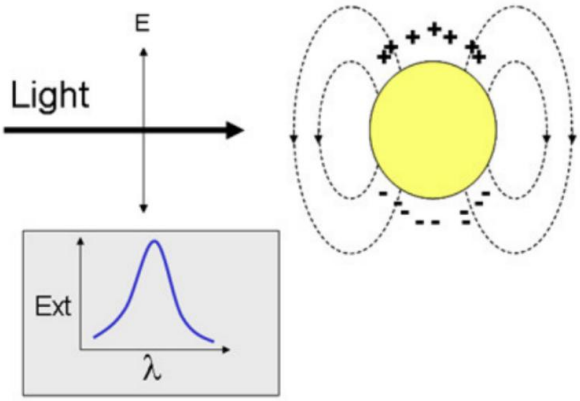

Figure 6.13 *Scheme of the localized surface plasmon resonance effect in a metallic nanoparticle.*

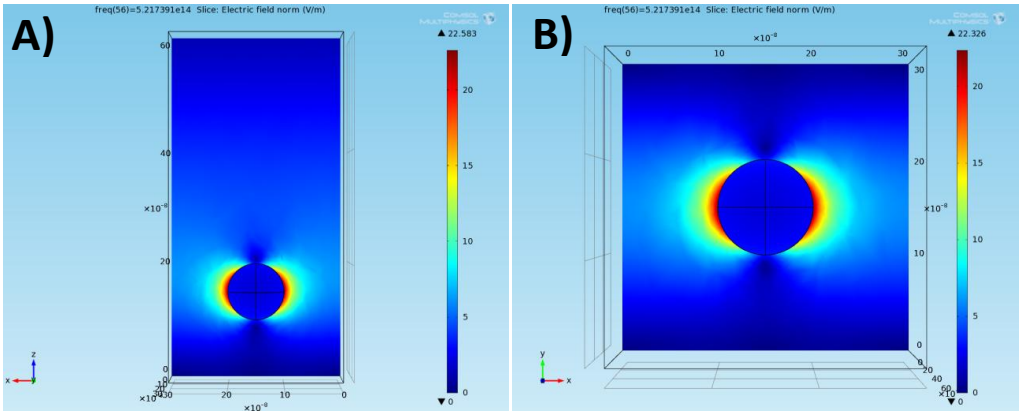

Figure 6.14 *Maps of the amplitude of the electric field, |E|, in V/m for one isolated gold nanosphere with a diameter of 50 nm for an incident light with a wavelength of 575 nm. Cross (A) and top sections (B).*

6.2.3.2.- NUMERICAL RESULTS: EXCITATION OF 633 nm and 785 nm

Figures 6.15 and 6.16 show the amplitude of the electric field, $|E|$, maps in V/m for a gold nanosphere pyramid for the contacting and the non-contacting distributions for

UNIVERSITAT ROVIRA I VIRGILI
DESIGN AND MODELLING OF INTERDIGITATED AND NANOSTRUCTURED POLYMER SOLAR CELLS
Pedro Granero Secilla
Dipòsit Legal: T 891-2015

a laser line excitation of 633 nm. In Figure 6.15 it can be seen that in the top of the pyramid there is an important concentration of the electric field. This field reaches its highest value in the contact point of the top nanosphere with the ones of the second layer (Figure 6.15D indication). There are also other important field concentrations in the rest of contact points between nanospheres. For the case of the non-contacting distribution (Figure 6.16) it is clear that the electric field is concentrated in the top of the pyramid, specifically around the equator of the top nanosphere, while in the rest of the nanostructure this field is weak.

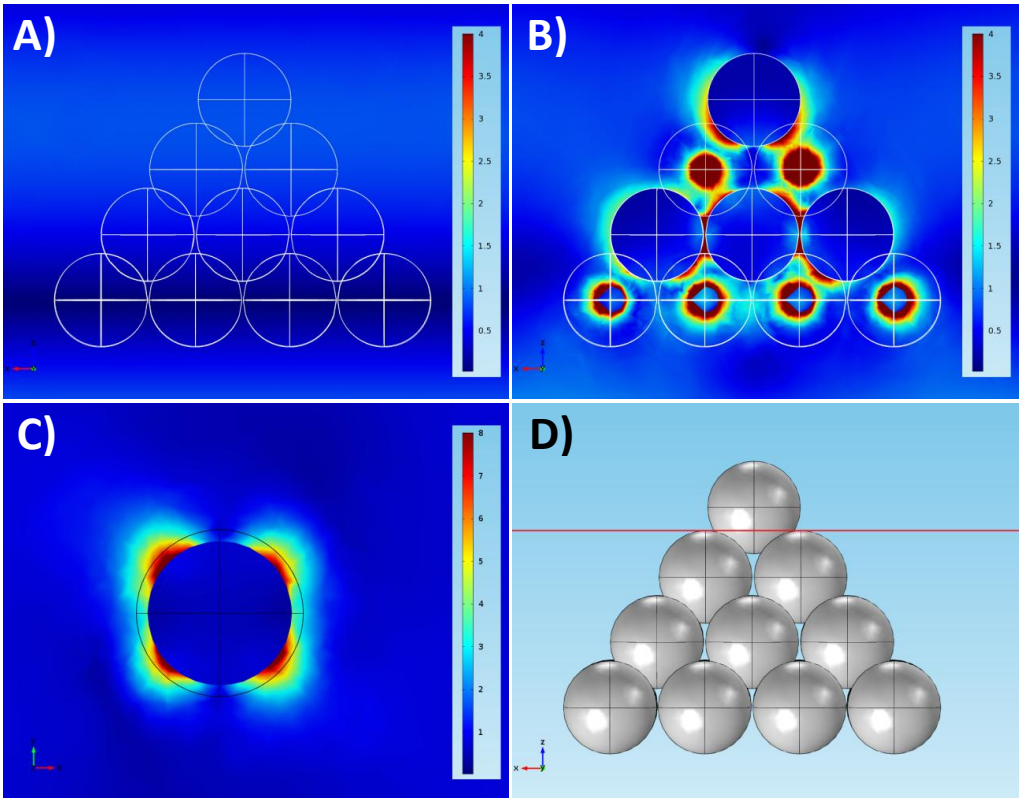

Figure 6.15 *Maps of the amplitude of the electric field, |E|, in V/m for a gold nanosphere pyramid for the contacting distribution for a laser line excitation of 633 nm. Side face without gold nanospheres (A), side face with gold nanospheres (B), and top sections (C). It is also displayed the crossing plane of the top section (red line) (D).*

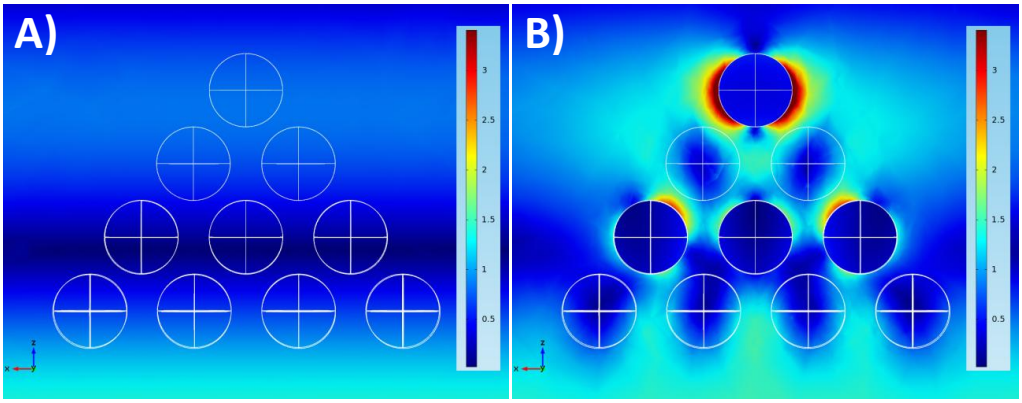

Figure 6.16 *Maps of the amplitude of the electric field, |E|, in V/m for a gold nanosphere pyramid for the non-contacting distribution for a laser line excitation of 633 nm. Side face without gold nanospheres (A), and side face with gold nanospheres (B).*

Figures 6.17 and 6.18 show the amplitude of the electric field, $|E|$, maps in V/m for a gold nanosphere pyramid for the contacting and the non-contacting distributions for a laser line excitation of 785 nm. As for the previous laser line excitation, it can be observed important electric field concentrations in the contact points between nanospheres. However, now we have the highest concentrations close to the third nanospheres layer. For the case of the non-contacting distribution (Figure 6.18) it can be seen again that there is an important electric field concentration in the top of the pyramid, specifically around the equator of the top nanosphere. However, now there is also another important field concentration in the third nanospheres layer. The global field concentration is also higher than for the laser line excitation of 633 nm.

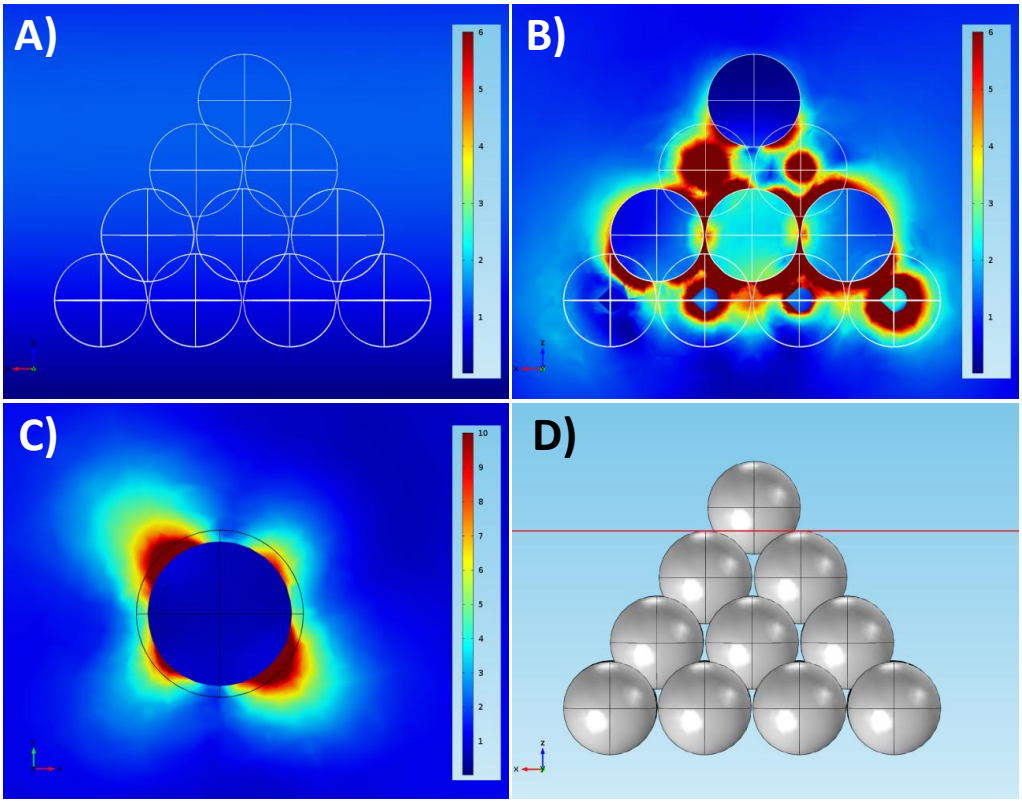

Figure 6.17 *Maps of the amplitude of the electric field, |E|, in V/m for a gold nanosphere pyramid for the contacting distribution for a laser line excitation of 785 nm. Side face without gold nanospheres (A), side face with gold nanospheres (B), and top sections (C). It is also displayed the crossing plane of the top section (red line) (D).*

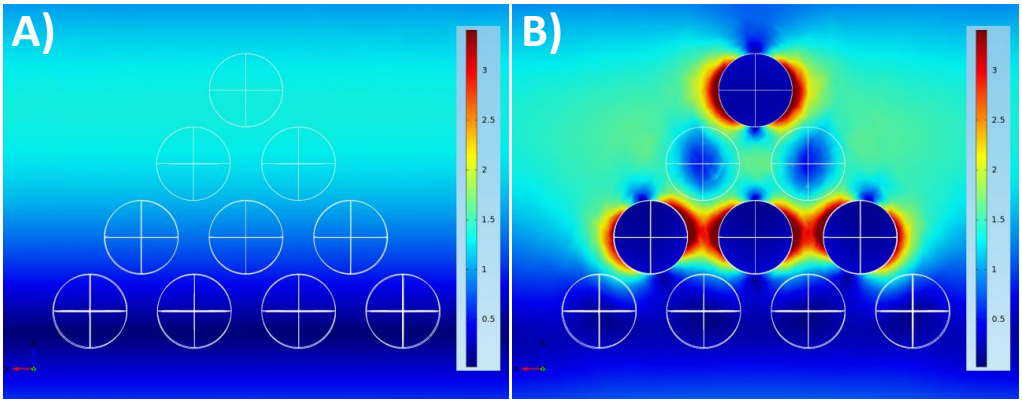

Figure 6.18 *Maps of the amplitude of the electric field, |E|, in V/m for a gold nanosphere pyramid for the non-contacting distribution for a laser line excitation of 785 nm. Side face without gold nanospheres (A), and side face with gold nanospheres (B).*

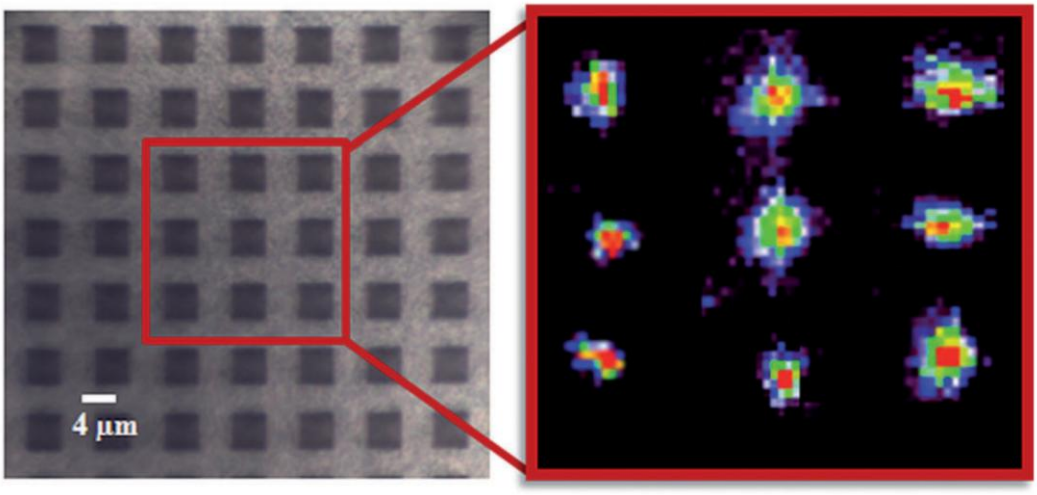

Figure 6.19 *Optical image and SERS imaging of several gold nanosphere pyramids. The SERS image shows enhancement mapping with higher signals concentrated around the center of the pyramids. Reproduced from [Alba-2013].*

UNIVERSITAT ROVIRA I VIRGILI
DESIGN AND MODELLING OF INTERDIGITATED AND NANOSTRUCTURED POLYMER SOLAR CELLS
Pedro Granero Secilla
Dipòsit Legal: T 891-2015

In Figure 6.19 it can be seen the optical image and SERS imaging of several experimental gold nanosphere pyramids. The SERS image shows enhancement mapping with higher signals concentrated around the center of the pyramids. If we compare these results with the simulation ones, the first conclusion that it can be extracted is that the non-contacting spheres distribution reproduces better the experimental data, since with this distribution the electric filed is concentrated clearly in the top of the pyramid. However, although with the contacting distribution the electric field is concentrated in a lower position, the highest field concentrations are still close to the pyramid top.

6.3.- SUMMARY AND CONCLUSIONS

In this chapter, the developed numerical simulation method exposed in Chapter 3 has been applied and adapted to other devices and structures to demonstrate that it can work correctly not only for the full organic solar cells that we have previously seen. The numerical model has been used to simulate two different cases: hybrid solar cells and gold nanosphere pyramids.

The hybrid solar cell studied in this chapter has the structure ITO/TiO_2/P3HT:PCBM/PEDOT:PSS/Ag, having therefore an inverted configuration where the ITO/TiO_2 layers act as the cathode and the Ag one acts as the anode. Unlike the previous studied devices, in this cell the active region is a blend of the different organic semiconductors instead of separated materials (bulk heterojunction architecture) and the TiO_2 electron collecting layer is nanostructured. The motivation of this nanostructured electrode is to try to increase the device efficiency, if compared with cells with flat TiO_2 layers, by increasing light absorption and improving charge collection.

UNIVERSITAT ROVIRA I VIRGILI
DESIGN AND MODELLING OF INTERDIGITATED AND NANOSTRUCTURED POLYMER SOLAR CELLS
Pedro Granero Secilla
Dipòsit Legal: T 891-2015

Several modifications of the method presented in Chapter 3 have been done to adapt the model to this different technology. To turn the P3HT/PCBM bilayer into a monolayer blend of P3HT:PCM we have replaced these two layers with only one that will act as the blend. The optical constants of this new layer, the refractive index (*n*) and the extinction coefficient (*k*) of the complex index of refraction ($\tilde{n} = n + ik$), have been obtained from the literature. The electrical parameters of the blend, such as the hole and the electron mobilities, have also been taken from published articles. Following the approach exposed in Chapter 4, we have been able to reproduce experimental results with a relative error in the characteristic parameters below the 3%. The experimental data have been provided by the group of Dr. Monica Lira-Cantu (from the Laboratory of Nanostructured Materials for Photovoltaic Energy, CIN2, Barcelona).

Finally, several geometrical parameters of the nanostructured TiO_2 and the P3HT:PCBM layers have been varied in order examine their influence on the device properties and response. The simulation study has included optical, exciton diffusion, and electrical simulations of several FLAT-TiO_2 and NIL-TiO_2 devices. The ranges of values for the geometrical parameters have been chosen on the basis of *SEM* estimates from actual devices.

From the obtained exciton generation rate maps, it can be concluded that the carriers are mainly generated near the TiO_2-blend interface due to the strong absorption of the blend. It also have been demonstrated that the NIL-TiO_2 cells achieve higher exciton generation rates than the FLAT-TiO_2 near the TiO_2-blend interface, which comes from a higher light absorption since this magnitude and the exciton generation rate are directly related. From the exciton diffusion analysis, it has been shown that for all the considered cases the NIL structures showed higher J_{PHOTO}. This demonstrates that the nanostructuring of the TiO_2 and of the blend layer helps

UNIVERSITAT ROVIRA I VIRGILI
DESIGN AND MODELLING OF INTERDIGITATED AND NANOSTRUCTURED POLYMER SOLAR CELLS
Pedro Granero Secilla
Dipòsit Legal: T 891-2015

increasing the amount of absorbed photons. The difference in J_{PHOTO} between the two structures, for the considered parameter ranges, is up to 23.34%. Finally, the electrical analysis has demonstrated that the increase in the efficiency of the NIL-TiO_2 devices with respect the flat ones comes basically from an increase in the short-circuit current (J_{SC}). This increase can be attributed to two effects of the nanostructured interface: the increase in the number of absorbed photons discussed above, and also the increase of interface area that improve carriers collection efficiency.

Regarding the gold nanosphere pyramids, we have presented a work about the simulation of the plasmonic effect in pyramids formed by layers of gold nanospheres. This kind of structures is intended to provide cheap ultrasensitive and ultrafast sensors with surface-enhanced Raman scattering (SERS) spectroscopy as the transducer, in our case, to develop a handheld reversible SERS sensor for the live monitoring of carbon monoxide in the atmosphere. The aim of this study has been to demonstrate that the optical part of the simulation procedure can be used to model different effects in geometries in the range of the nm so it is not only restricted to solar cells.

Our optical study has been carried out on the basis of finite-element simulations with the COMSOL Multiphysics® software exposed in Chapter 3. By solving the complete Maxwell equations considering the optical constants of the involved materials as a function of the wavelength and by using the scattered field formulation, the plasmonic effects in nanoparticles have been modelled. The simulated structure of this section reproduces the top part of one gold nanosphere pyramid, that is the four higher layers of nanospheres.

Before modelling the gold nanosphere pyramids, a single gold nanosphere has been simulated to check the validity of the procedure. From these results, we have

UNIVERSITAT ROVIRA I VIRGILI
DESIGN AND MODELLING OF INTERDIGITATED AND NANOSTRUCTURED POLYMER SOLAR CELLS
Pedro Granero Secilla
Dipòsit Legal: T 891-2015

concluded that the applied numerical simulation method is able to reproduce, at least in a qualitatively way, the plasmonic effect in a metal nanoparticle. Hence, it can be expected that the simulations of gold nanosphere pyramids will be correct.

Results have shown that in the distribution where the gold nanospheres are non-contacting between them, the electric field is concentrated more in the top of the pyramid, like in the experimental case. However, despite the electric field is concentrated in a lower position in the case where there is not space between nanospheres, it can be considered that this lower position it is still the top of the pyramid. Hence, the optical activity of these pyramidal supercrystals has been demonstrated both experimentally and theoretically, with the results matching in a qualitatively way.

A further development of this simulation approach can lead to a proper modelling of metallic nanoparticles as constituents of solar cells to enhance its efficiency.

UNIVERSITAT ROVIRA I VIRGILI
DESIGN AND MODELLING OF INTERDIGITATED AND NANOSTRUCTURED POLYMER SOLAR CELLS
Pedro Granero Secilla
Dipòsit Legal: T 891-2015

CHAPTER 7

SUMMARY AND CONCLUSIONS

7.1.- SUMMARY AND CONCLUSIONS

In many fields, numerical simulation models have helped to develop many technologies and understand their mechanisms. They are able to predict results without the need to fabricate real devices. This fact allows reducing development times, since simulations are usually faster than a device fabrication, and costs, since we can reduce material waste by avoiding the fabrication of non-optimal devices. Since many years ago, several accurate models exist for the case of inorganic cells, however the behaviour of organic solar cells (OSC) is still not perfectly known. Additionally, it is difficult to know a priori if the existing models for OSC will be

UNIVERSITAT ROVIRA I VIRGILI
DESIGN AND MODELLING OF INTERDIGITATED AND NANOSTRUCTURED POLYMER SOLAR CELLS
Pedro Granero Secilla
Dipòsit Legal: T 891-2015

suitable and accurate enough for the small geometries of the interdigitated organic devices. So, there is still work to do to obtain a precise numerical simulation model for OSC.

The main objectives of this thesis have been:

- Develop a complete model to simulate the different steps of the photovoltaic conversion process in interdigitated organic solar cells. The model has been based on the finite-element method (FEM), which can give us information of every magnitude as a function of the position. Most of the existing models consider the active region of the devices a uniform material from the point of view of light interaction. This simplification is not important when we have an interpenetrating blend, but it may affect the final results in the case of interdigitated cells.
- Show that this model can be used to make a systematic study of interdigitated OSC that will help to predict which geometrical characteristic will be better to optimize this kind of devices and how to increase their efficiency.
- Validate the model with experimental results of real devices obtained in our facilities and, if necessary, improve, adjust or correct the model.
- To demonstrate that the developed method can simulate correctly different devices and structures, by making some adaptations, and not only interdigitated full organic solar cells.

The numerical simulation procedure exposed in this Ph. D. thesis has been developed by using the finite-element method (FEM) in COMSOL MULTIPHYSICS® software. This method allows computing the different magnitudes related to the photovoltaic

UNIVERSITAT ROVIRA I VIRGILI
DESIGN AND MODELLING OF INTERDIGITATED AND NANOSTRUCTURED POLYMER SOLAR CELLS
Pedro Granero Secilla
Dipòsit Legal: T 891-2015

conversion process as a function of the position. The complete Maxwell equations, the *exciton diffusion equation* and the drift-diffusion model are solved within the same numerical framework. The model can be divided into two main parts: the optical and the electrical behaviour. The optical part includes light absorption and exciton generation, while the electrical one includes exciton diffusion, and free charge generation, transport and collection. The results of each step of the photovoltaic conversion process are used as an input of the subsequent step, in all cases as function of the position.

In the systematic theoretical study of interdigitated OSC we analyzed the influence of the nanostructured dissociation interface on the overall efficiency of the devices. We performed a systematic and complete analysis of light absorption, exciton diffusion and carrier transport, all in the same numerical framework, and for a 2D model of such cells. With this, we obtain their dependence on the cell geometrical parameters: pillar diameter and height, and nanostructure period. The donor and the acceptor materials of our cells are P3HT and PCBM, respectively. From the point of view of light absorption, results show that the maximum amount of light is absorbed only for two specific values of the nanopillar height, T = 80 nm and T = 230 nm, independently of the nanopillar diameter. This suggests that it is due to light interference effects. For these nanopillar heights, the maximum absorption is achieved by nanostructures with a period of β = 25 nm.

By simulating the exciton diffusion process the maximum attainable photocurrent density (J_{PHOTO}) can be determined. Results show that to obtain a higher J_{PHOTO} than that of the better planar bilayer structure, small nanostructure periods, up to 100 nm, should be used. By examining the exciton diffusion maps, we can conclude that small nanopillars favour the excitons to reach the Donor–Acceptor (D–A) interface and that

UNIVERSITAT ROVIRA I VIRGILI
DESIGN AND MODELLING OF INTERDIGITATED AND NANOSTRUCTURED POLYMER SOLAR CELLS
Pedro Granero Secilla
Dipòsit Legal: T 891-2015

the upper limit of the nanopillar height is directly related to the limited exciton diffusion length.

Finally, from the current density–voltage (*J*–*V*) characteristics, we obtain the overall efficiency of the cells. We observe that there is a direct correlation between the J_{PHOTO} and the cell efficiency, which indicates that the charge transport has a lower influence on the overall charge collection efficiency. Thus, in order to increase the efficiency, the exciton diffusion process is the key limiting factor and this process is better for the smaller nanopillar diameters. Best results have been achieved for β = 25 nm, T = 80 nm, and γ (ratio of the nanopillar diameter to the period) = 0.75, with an efficiency that is 3.6 times higher than the best planar bilayer reference device.

An optimal interdigitated structure should find a compromise between a high proportion of electron donor to increase light absorption and a small pillar diameter to ensure an extended D–A interface for exciton dissociation. Due to the short exciton diffusion length of organic materials, big nanopillars diameters will result in cells with an efficiency even lower than the one of planar bilayer equivalents. The method developed in this work can be useful to design optimal full organic solar cells, taking into account technological parameters and constraints.

To validate the used simulation method, it has been applied to experimental interdigitated devices manufactured in our facilities. Here we used cells with a structure of ITO/PEDOT:PSS/P3HT/PCBM/Ag. To totally fit the model to the real devices, some adaptations and parameter adjustments have been performed. The adaptations have included:

UNIVERSITAT ROVIRA I VIRGILI
DESIGN AND MODELLING OF INTERDIGITATED AND NANOSTRUCTURED POLYMER SOLAR CELLS
Pedro Granero Secilla
Dipòsit Legal: T 891-2015

- The use of modified optical constants for the PEDOT:PSS layer
- An extended solar spectrum range
- A modified exciton diffusion length for P3HT
- Free charge mobilities adjustments

After these adaptations, the simulated results were in good agreement with the experimental data.

After the experimental validation, different kinds of OSC have been modelled. By varying the D–A interface geometry, we have performed simulations for planar bilayer (PBL), nanopillars (NP), nanowells (NW) and nanopyramids (NPYR) D–A junctions. Two configurations, the conventional and the inverted one, have been used in this study. An optical and exciton diffusion study have been carried out with the exciton diffusion length (L_D) used as a parameter.

Results have shown that there is an important reduction of the amount of absorbed light by the active region (P3HT layer) in the inverted configuration if compared with the amount absorbed by the conventional one. This fact can be attributed to the different layer stacking of each configuration. For the conventional case, light arrives to the P3HT layer by only crossing through the ITO and the PEDOT:PSS layers, which are nearly transparent. For the inverted configuration, light have to cross the PCBM layer instead. This material absorbs in a similar range than the P3HT. So the amount of light that arrives to the active region will be lower.

However, the exciton diffusion study have shown that despite absorbing less light, and as a consequence having a lower exciton generation rate, the inverted configuration can generate higher photocurrents in all cases except for the NPYR D–A

UNIVERSITAT ROVIRA I VIRGILI
DESIGN AND MODELLING OF INTERDIGITATED AND NANOSTRUCTURED POLYMER SOLAR CELLS
Pedro Granero Secilla
Dipòsit Legal: T 891-2015

interface. The exciton concentration maps have shown that for the inverted configuration excitons are distributed in a proper way, i.e. close to the D–A interface to dissociated, so losses due to exciton recombination are reduced. This is an interesting fact since the inverted configuration has the advantage of having a higher stability and durability when exposed to the oxygen and to the water of the atmosphere without degrading than the conventional one. Hence, this configuration can be a promising solution to increase the efficiency and the lifetime of OSC.

In the last part of this Ph. D. thesis, the developed numerical simulation method has been applied and adapted to other devices and structures to demonstrate that it can work correctly not only for the full organic solar cells that we have previously seen. The numerical model has been used to simulate two different cases: hybrid solar cells and gold nanosphere pyramids.

The studied hybrid solar cell has the structure ITO/TiO_2/P3HT:PCBM/PEDOT:PSS/Ag, having therefore an inverted configuration where the ITO/TiO_2 layers act as the cathode and the Ag one acts as the anode. Unlike the previous studied devices, in this cell the active region is a blend of the different organic semiconductors instead of separated materials (bulk heterojunction architecture) and the TiO_2 electron collecting layer is nanostructured. The motivation of this nanostructured electrode is to try to increase the device efficiency, if compared with cells with flat TiO_2 layers, by increasing light absorption and improving charge collection.

Several modifications of the numerical procedure have been done to adapt the model to this different technology. To turn the P3HT/PCBM bilayer into a monolayer blend of P3HT:PCM we have replaced these two layers with only one that will act as the blend. The optical constants of this new layer, the refractive index (n) and the extinction coefficient (k) of the complex index of refraction ($\tilde{n} = n + ik$), have been

UNIVERSITAT ROVIRA I VIRGILI
DESIGN AND MODELLING OF INTERDIGITATED AND NANOSTRUCTURED POLYMER SOLAR CELLS
Pedro Granero Secilla
Dipòsit Legal: T 891-2015

obtained from the literature. The electrical parameters of the blend, such as the hole and the electron mobilities, have also been taken from published articles. Following the approach used to reproduce the experimental values of the interdigitated OSC, we have been able to reproduce experimental results with a difference in the characteristic parameters below the 3%.

Finally, several geometrical parameters of the nanostructured TiO_2 and the P3HT:PCBM layers have been varied in order examine their influence on the device properties and response. The simulation study has included light absorption, exciton diffusion, and electrical simulations of several FLAT-TiO_2 and NIL-TiO_2 devices. The ranges of values for the geometrical parameters have been chosen on the basis of *SEM* estimates from actual devices.

From the obtained exciton generation rate maps, it can be concluded that the carriers are mainly generated near the TiO_2-blend interface due to the strong absorption of the blend. It also have been demonstrated that the NIL-TiO_2 cells achieve higher exciton generation rates than the FLAT-TiO_2 near the TiO_2-blend interface, which comes from a higher light absorption since this magnitude and the exciton generation rate are directly related. From the exciton diffusion analysis, it has been shown that for all the considered cases the NIL structures showed higher J_{PHOTO}. This demonstrates that the nanostructuring of the TiO_2 and of the blend layer helps increasing the amount of absorbed photons. The difference in J_{PHOTO} between the two structures, for the considered parameter ranges, is up to 23.34%. Finally, the electrical analysis has demonstrated that the increase in the efficiency of the NIL-TiO_2 devices with respect the flat ones comes basically from an increase in the short circuit current (J_{sc}). This increase can be attributed to two effects of the nanostructured interface: the increase in the number of absorbed photons discussed above, and also the increase of interface area that improve carriers collection efficiency.

Regarding the gold nanosphere pyramids, we have presented a work about the simulation of the plasmonic effect in pyramids formed by layers of gold nanospheres. This kind of structures is intended to provide cheap ultrasensitive and ultrafast sensors with surface-enhanced Raman scattering (SERS) spectroscopy as the transducer, in our case, to develop a handheld reversible SERS sensor for the live monitoring of carbon monoxide in the atmosphere. The aim of this study has been to demonstrate that the optical part of the simulation procedure can be used to model different effects in geometries in the range of the nm so it is not only restricted to solar cells.

By solving the complete Maxwell equations considering the optical constants of the involved materials as a function of the wavelength and by using the scattered field formulation, the plasmonic effects in nanoparticles have been modelled. The simulated structure reproduces the top part of one gold nanosphere pyramid, that is the four higher layers of nanospheres, in two distributions: one with non-contacting gold nanospheres and another with contacting gold nanospheres.

Before modelling the gold nanosphere pyramids, a single gold nanosphere has been simulated to check the validity of the procedure. From these results, we have concluded that the applied numerical simulation method is able to reproduce, at least in a qualitatively way, the plasmonic effect in a metal nanoparticle. Hence, it can be expected that the simulations of gold nanosphere pyramids will be correct.

Results have shown that in the distribution with the non-contacting gold nanospheres, the electric field is concentrated more in the top of the pyramid, like in the experimental case. However, despite the electric field is concentrated in a lower position in the case where there is not space between nanospheres, it can be considered that this lower position it is still the top of the pyramid. Hence, the optical

UNIVERSITAT ROVIRA I VIRGILI
DESIGN AND MODELLING OF INTERDIGITATED AND NANOSTRUCTURED POLYMER SOLAR CELLS
Pedro Granero Secilla
Dipòsit Legal: T 891-2015

activity of these pyramidal supercrystals has been demonstrated both experimentally and theoretically, with the results matching in a qualitatively way.

A further development of this optical simulation approach can lead to a proper modelling of metallic nanoparticles as constituents of solar cells to enhance its efficiency.

UNIVERSITAT ROVIRA I VIRGILI
DESIGN AND MODELLING OF INTERDIGITATED AND NANOSTRUCTURED POLYMER SOLAR CELLS
Pedro Granero Secilla
Dipòsit Legal: T 891-2015

BIBLIOGRAPHY

REFERENCES

[Alba-2013] M. Alba, N. Pazos-Perez, B. Vaz, P. Formentin, M. Tebbe, M.A. Correa-Duarte, P. Granero, J. Ferré-Borrull, R. Alvarez, J. Pallarès, A. Fery, A.R. de Lera, L.F. Marsal, and R.A. Alvarez-Puebla, "Macroscale plasmonic substrates for highly sensitive surface-enhanced Raman scattering", *Angew. Chem. Int. Ed.* **52** 6459-6463, (2013).

[Alvarez-Puebla-2011] R.A. Alvarez-Puebla, A. Agarwal, P. Manna, B.P. Khanal, P. Aldeanueva-Potel, E. Carbó-Argibay, N. Pazos-Pérez, L. Vigderman, E.R. Zubarev, N.A. Kotov, and L.M. Liz-Marzán, "Gold nanorods 3D-supercrystals as surface enhanced Raman scattering spectroscopy substrates for the rapid detection of scrambled prions", *Proc. Natl. Acad. Sci. USA* **108** 8157-8161, (2011).

[Andersson-2008] V. Andersson, K. Tvingstedt, and O. Inganäs, "Optical modeling of a folded organic solar cell", *J. Appl. Phys.* **103** 094520, (2008).

[Aroca-2005] R.F. Aroca, R.A. Alvarez-Puebla, N. Pieczonka, S. Sanchez-Cortez, and J.V. Garcia-Ramos, "Surface-enhanced Raman scattering on colloidal nanostructures", *Adv. Colloid Interface Sci.* **116** 45-61, (2005).

[Avnon-2011] E. Avnon, N. Yaacobi-Gross, E. Ploshnik, R. Shenhar, and N. Tessler, "Low cost, nanometer scale nanoimprinting – Application to organic solar cells optimization", *Org. Electron.* **12** 1241-1246, (2011).

[Baek-2009] S. Baek, J.B. Park, W. Lee, S.H. Han, J. Lee, and S.H. Lee, "A facile method to prepare regioregular poly(3-hexylthiophene) nanorod arrays using anodic aluminium oxide templates and capillary force", *New J. Chem.* **33** 986-990, (2009).

[Baek2-2009] W.H. Baek, I. Seo, T.S. Yoon, H. H. Lee, C. M. Yun, and Y.S. Kim, "Hybrid inverted bulk heterojunction solar cells with nanoimprinted TiO_2 nanopores", *Sol. Energy Mater. Sol. Cells* **93** 1587-1591, (2009).

[Baker-2005] G.A. Baker, and D.S. Moore, "Progress in plasmonic engineering of surface-enhanced Raman-scattering substrates toward ultra-trace analysis", *Anal. Bioanal. Chem.* **382** 1751-1770, (2005).

[Balderrama-2014] V.S. Balderrama, *Fabrication of bulk and interdigitated organic solar cells and analysis of degradation mechanisms*, (Universitat Rovira i Virgili, Tarragona, 2014).

[Barker-2003] J.A. Barker, C.M. Ramsdale, and N.C. Greenham, "Modeling the current-voltage characteristics of bilayer polymer photovoltaic devices", *Phys. Rev. B* **67** 075205, (2003).

[Bedford-2012] E.E. Bedford, J. Spadavecchia, C.M. Pradier, and F.X. Gu, "Surface plasmon resonance biosensors incorporating gold nanoparticles", *Macromol. Biosci.* **12** 724-739, (2012).

[Born-Wolf-1999] M. Born and E. Wolf, *Principles of optics: Electromagnetic theory of propagation, interference and diffraction of light*, *7th ed.*, (Cambridge University Press, Cambridge, 1999).

[Brabec-2004] C. J. Brabec, "Organic photovoltaics: Technology and market", *Sol. Energy Mater. Sol. Cells* **83** 273-292, (2004).

[Brütting-2005] W. Brütting (editor), *Physics of organics semiconductors*, (WILEY-VCH, Weinheim, 2005).

[Burkhard-2009] G.F. Burkhard, E.T. Hoke, S.R. Scully, and M.D. McGehee, "Incomplete exciton harvesting from fullerenes in bulk heterojunction solar cells", *Nano Lett.* **9** 4037-4041, (2009).

[Chen-2009] L.M. Chen, Z. Hong, G. Li, and Y. Yang, "Recent progress in polymer solar cells: Manipulation of polymer:fullerene morphology and the formation of efficient inverted polymer solar cells", *Adv. Mater.* **21** 1434-1449, (2009).

[Chiang-1977] C.K. Chiang, C.R. Fincher, Y.W. Park, A.J. Heeger, H.Shirakawa, E.J. Louis, S.C. Gau, and A.G. MacDiarmid, "Electrical conductivity in doped polyacetylene", *Phys. Rev. Lett.* **39** 1098-1101, (1977).

[COMSOL-2010] *COMSOL Multiphysics user's guide*, (COMSOL AB, 2010).

[COMSOL RF-2010] *COMSOL Multiphysics RF module user's guide*, (COMSOL AB, 2010).

[Cook-2009] S. Cook, A. Furube, R. Katoh, and L. Han, "Estimate of singlet diffusion lengths in PCBM films by time-resolved emission studies", *Chem. Phys. Lett.* **478** 33-36, (2009).

[de Jong-2000] M.P. de Jong, L.J. van IJzendoorn, and M.J.A. de Voigt, "Stability of the interface between indium-tin-oxide and poly(3,4-ethylenedioxythiophene)/poly(styrene sulfonate) in polymer light-emitting diodes", *Appl. Phys. Lett.* **77** 2255-2257, (2000).

[Defranoux-2010] C. Defranoux, *Spectroscopic ellipsometry applied to solar cell characterization*, (SOPRA Application note).

[Dennler-2007] G. Dennler, K. Forberich, M.C. Scharber, C.J. Brabec, I. Tomiš, K. Hingerl, and T. Fromherz, "Angle dependence of external and internal quantum efficiencies in bulk-heterojunction organic solar cells", *J. Appl. Phys.* **102** 054516, (2007).

[Fang-1974] P.H Fang, "Analysis of conversion efficiency of organic-semiconductor solar cells", *J. Appl. Phys.* **45** 4672-4673, (1974).

[Félidj-2004] N. Félidj, S.L. Truong, J. Aubard, G. Lévi, J.R. Krenn, A. Hohenau, A. Leitner, and F.R. Aussenegg, "Gold particle interaction in regular arrays probed by surface enhanced Raman scattering", *J. Chem. Phys.* **120** 7141-7146, (2004).

[Ghosh-1978] A.K. Ghosh and T. Feng, "Merocyanine organic solar cells", *J. Appl. Phys.* **49** 5982-5989, (1978).

[Granero-2013] P. Granero, V.S. Balderrama, J. Ferré-Borrull, J. Pallarès, and L.F. Marsal, "Two-dimensional finite-element modeling of periodical interdigitated full organic solar cells", *J. Appl. Phys.* **113** 043107, (2013).

[Granero2-2013] P. Granero, V.S. Balderrama, J. Ferré-Borrull, J. Pallarès, and L.F. Marsal, "Light absorption modeling of ordered bulk heterojunction organic solar cells", *Curr. Appl. Phys.* **13** 1801-1807, (2013).

[Greczynski-2001] G. Greczynski, Th. Kugler, M. Keil, W. Osikowicz, M. Fahlman, and W.R. Salaneck, "Photoelectron spectroscopy of thin films of PEDOT–PSS conjugated polymer blend: a mini-review and some new results", *J. Electron. Spectrosc.* **121** 1-17, (2001).

[Green-2014] M.A. Green, K. Emery, Y. Hishikawa, W. Warta, and E.D. Dunlop, "Solar cell efficiency tables (version 44)", *Prog. Photovoltaics.* **22** 701-710, (2014).

[Hadziioannou-Malliaras-2007] G. Hadziioannou and G.G. Malliaras (editors), *Semiconducting polymers: Chemistry, physics and engineering*, (Wiley, Weinheim, 2007).

[Hau-2008] S.K. Hau, H.L. Yip, N.S. Baek, J. Zou, K. O'Malley, and A.K.Y. Jen, "Air-stable inverted flexible polymer solar cells using zinc oxide nanoparticles as an electron selective layer", *Appl. Phys. Lett.* **92** 253301, (2008).

[Hau-2010] S.K. Hau, H.L. Yip, and A.K.Y Jen, "A review on the development of the inverted polymer solar cell architecture", *Polym. Rev.* **50** 474-510, (2010).

[He-2011] X.M. He, F. Gao, G.L. Tu, D.G. Hasko, S. Hüttner, N.C. Greenham, U. Steiner, R.H. Friend, and W.T.S. Huck, "Formation of well-ordered heterojunctions in polymer:PCBM photovoltaic devices", *Adv. Funct. Mater.* **21** 139-146, (2011).

[Henzie-2012] J. Henzie, M. Grünwald, A. Widmer-Cooper, P.L. Geissler, and P. Yang, "Self-assembly of uniform polyhedral silver nanocrystals into densest packings and exotic superlattices", *Nat. Mater.* **11** 131-137, (2012).

[Hoa-2007] X.D. Hoa, A.G. Kirk, and M. Tabrizian, "Towards integrated and sensitive surface plasmon resonance biosensors: A review of recent progress", *Biosens. Bioelectron.* **23** 151-160, (2007).

[Hoppe-2002] H. Hoppe, N.S. Sariciftci, and D. Meissner, "Optical constants of conjugated polymer/fullerene based bulk-heterojunction organic solar cells", *Mol. Cryst. Liq. Crys. A* **385** 233-239, (2002).

[Hoppe-2004] H. Hoppe and N.S. Sariciftci, "Organic solar cells: An overview", *J. Mater. Res.* **19** 1924-1945, (2004).

[Kim-2007] J.Y. Kim, K. Lee, N.E. Coates, D. Moses, T.Q. Nguyen, M. Dante, and A.J. Heeger, "Efficient tandem polymer solar cells fabricated by all-solution processing", *Science* **317** 222-225, (2007).

[Kim-2010] J.S. Kim, Y. Park, D.Y. Lee, J.H. Lee, J.H. Park, J.K. Kim, and K. Cho, "Poly(3-hexylthiophene) nanorods with aligned chain orientation for organic photovoltaics", *Adv. Funct. Mater.* **20** 540-545, (2010).

[Kim2-2010] T. Kim, D. Kurunthu, J.J. Burdett, and C.J. Bardeen, "The effects of nanopillar surface texturing on the photoluminescence of polymer films", *J. Appl. Phys.* **108** 033114, (2010).

[Kim-2011] J. Kim, K. Kim, S.H. Ko, and W. Kim, "Optimum design of ordered bulk heterojunction organic photovoltaics", *Sol. Energy Mater. Sol. Cells* **95** 3021-3024, (2011).

[Kim-2013] S. Kim, C.H. Kim, S.K. Lee, J.H. Jeong, J. Lee, S.H. Jin, W.S. Shin, C.E. Song, J.H. Choi, and J.R. Jeong, "Highly efficient uniform ZnO nanostructures for an

electron transport layer of inverted organic solar cells", *Chem. Commun.* **49** 6033-6035, (2013).

[Kirchartz-2008] T. Kirchartz, B.E. Pieters, K. Taretto, and U. Rau, "Electro-optical modeling of bulk heterojunction solar cells", *J. Appl. Phys.* **104** 094513, (2008).

[Kneipp-2006] K. Kneipp, H. Kneipp, and J. Kneipp, "Surface-enhanced Raman scattering in local optical fields of silver and gold nanoaggregates: From single-molecule Raman spectroscopy to ultrasensitive probing in live cells", *Acc. Chem. Res.* **39** 443-450, (2006).

[Knupfer-2003] M. Knupfer, "Exciton binding energies in organic semiconductors", *Appl. Phys. A-Mater.* **77** 623-626, (2003).

[Koster-2005] L.J.A. Koster, E.C.P. Smits, V.D. Mihailetchi, and P.W.M. Blom, "Device model for the operation of polymer/fullerene bulk heterojunction solar cells" *Phys. Rev. B* **72** 085205, (2005).

[Kotlarski-2008] J.D. Kotlarski, P.W.M. Blom, L.J.A. Koster, M. Lenes, and L.H. Slooff, "Combined optical and electrical modeling of polymer:fullerene bulk heterojunction solar cells", *J. Appl. Phys.* **103** 084502, (2008).

[Kyaw-2008] A.K.K. Kyaw, X.W. Sun, C.Y. Jiang, G. Q. Lo, D.W. Zhao, and D.L. Kwong, "An inverted organic solar cell employing a sol-gel derived ZnO electron selective layer and thermal evaporated MoO_3 hole selective layer", *Appl. Phys. Lett.* **93** 221107, (2008).

[Larouche-2008] S. Larouche and L. Martinu, "OpenFilters: open-source software for the design, optimization, and synthesis of optical filters" *Appl. Optics* **47** C219-C230, (2008).

[Liang-2010] Y. Liang, Z. Xu, J. Xia, S.T. Tsai, Y. Wu, G. Li, C. Ray, and L. Yu, "For the bright future—Bulk heterojunction polymer solar cells with power conversion efficiency of 7.4%", *Adv. Mater.* **22** E135-E138, (2010).

[Liao-2008] H.H. Liao, L.M. Chen, Z. Xu, G. Li, and Y. Yang, "Highly efficient inverted polymer solar cell by low temperature annealing of Cs_2CO_3 interlayer", *Appl. Phys. Lett.* **92** 173303, (2008).

[Lin-2013] Z. Lin, C. Jiang, C. Zhu, and J. Zhang, "Development of inverted organic solar cells with TiO_2 interface layer by using low-temperature atomic layer deposition", *ACS Appl. Mater. Interfaces* **5** 713-718, (2013).

[MacDiarmid-1976] A.G. MacDiarmid, C.M. Mikulski, M.S. Saran, P.J. Russo, M.J. Cohen, A.A. Bright, A.F. Garito, and A.J. Heeger, "Synthesis and selected properties of polymeric sulfur nitride, (polythiazyl), $(SN)_x$", *Adv. Chem. Ser.* **150** 63-72, (1976).

[Maier-2007] S.A. Maier, *Plasmonics: Fundamentals and applications*, (Springer, New York, 2007).

[Masuda-1997] H. Masuda, H. Yamada, M. Satoh, H. Asoh, M. Nakao, and T. Tamamura, "Highly ordered nanochannel-array architecture in anodic alumina", *Appl. Phys. Lett.* **71** 2770-2772, (1997).

[McMahon-2009] J.M. McMahon, A.I. Henry, K.L. Wustholz, M.J. Natan, R.G. Freeman, R.P. Van Duyne, and G.C. Schatz, "Gold nanoparticle dimer plasmonics: Finite element method calculations of the electromagnetic enhancement to surface-enhanced Raman spectroscopy", *Anal. Bioanal. Chem.* **394** 1819-1825, (2009).

[Meng-2010] L. Meng, Y. Shang, Q. Li, Y. Li, X. Zhan, Z. Shuai, R.G.E. Kimber, and A.B. Walker, "Dynamic Monte Carlo simulation for highly efficient polymer blend photovoltaics", *J. Phys. Chem. B* **114** 36-41, (2010).

[Merritt-1976] V.Y. Merritt and H.J. Hovel, "Organic solar cells of hydroxy squarylium", *Appl. Phys. Lett.* **29** 414-415, (1976).

[Mihailetchi-2006] V.D. Mihailetchi, H. Xie, B. de Boer, L.J.A. Koster, and P.W.M. Blom, "Charge transport and photocurrent generation in Poly(3-hexylthiophene):Methanofullerene bulk-heterojunction solar cells", *Adv. Funct. Mater.* **16** 699-708, (2006).

[Monestier-2007] F. Monestier, J.J. Simon, P. Torchio, L. Escoubas, F. Flory, S. Bailly, R. Bettignies, S. Guillerez, C. Defranoux, "Modeling the short-circuit current density of polymer solar cells based on P3HT:PCBM blend", *Sol. Energy Mater. Sol. Cells* **91** 405-410, (2007).

[Monestier-2008] F. Monestier, *Amélioration de l'absorption photonique dans les cellules photovoltaïques organiques*, (Université Paul Cezanne Aix-Marseille III, Marseille, 2008).

[Nakamura-2005] J. Nakamura, K. Murata, and K. Takahashi, "Relation between carrier mobility and cell performance in bulk heterojunction solar cells consisting of soluble polythiophene and fullerene derivatives", *Appl. Phys. Lett.* **87** 132105, (2005).

[Nobel Foundation-2000] *Nobel Prize laureates on chemistry list*, (Nobel Foundation, 2000). Available: http://nobelprize.org/chemistry/laureates/2000/index.html

[Nolasco-2010] J.C. Nolasco, R. Cabré, J. Ferré-Borrull, L.F. Marsal, M. Estrada, and J. Pallarès, "Extraction of poly (3-hexylthiophene) (P3HT) properties from dark current voltage characteristics in a P3HT/*n*-crystalline-silicon solar cell", *J. Appl. Phys.* **107** 044505, (2010).

[Pacios-2006] R. Pacios, A.J. Chatten, K. Kawano, J.R. Durrant, D.D.C. Bradley, and J. Nelson, "Effects of photo-oxidation on the performance of poly[2-methoxy-5-(3',7'-dimethyloctyloxy)-1,4-phenylene vinylene]:[6,6]-phenyl C_{61}-butyric acid methyl ester solar cells", *Adv. Funct. Mater* **16** 2117-2126, (2006).

[Palacios-2008] R. Palacios, P. Formentín, T. Trifonov, M. Estrada, R. Alcubilla, J. Pallarés, and L.F. Marsal, "Semiconducting P3HT microstructures: fibres and tubes obtained from macroporous silicon template", *Phys. Status Solidi Rapid Res. Lett.* **2** 206-208, (2008).

[Palik-1985] E.D. Palik, *Handbook of optical constants of solids*, (Academic Press, Boston, 1985).

[Paulus-2012] G.L.C. Paulus, M.H. Ham, and M.S. Strano, "Anomalous thickness-dependence of photocurrent explained for state-of-the-art planar nano-heterojunction organic solar cells", *Nanotechnology* **23** 095402, (2012).

[Pazos-Perez-2012] N. Pazos-Perez, C.S. Wagner, J.M. Romo-Herrera, L.M. Liz-Marzán, F.J. García de Abajo, A. Wittemann, A. Fery, and R.A. Alvarez-Puebla, "Organized plasmonic clusters with high coordination number and extraordinary enhancement in surface-enhanced Raman scattering (SERS)", *Angew. Chem. Int. Ed.* **51** 12688-12693, (2012).

[Pettersson-1999] L.A.A. Pettersson, L.S. Roman, and O. Inganäs, "Modeling photocurrent action spectra of photovoltaic devices based on organic thin films", *J. Appl. Phys.* **86** 487-496, (1999).

[Pettersson-2002] L.A.A. Pettersson, S. Ghosh, and O. Inganäs, "Optical anisotropy in thin films of poly(3,4-ethylenedioxythiophene)–poly(4-styrenesulfonate)", *Org. Electron.* **3** 143-148, (2002).

[Raba-2014] A. Raba, Y. Leroy, and A.S. Cordan, "Organic solar cells: a rigorous model of the donor-acceptor interface for various bulk heterojunction morphologies", *J. Appl. Phys.* **115** 054508, (2014).

[Rakic-1995] A.D. Rakic, "Algorithm for the determination of intrinsic optical constants of metal films: application to aluminum", *Appl. Opt.* **34** 4755-4767, (1995).

[Red Eléctrica de España-2013] *El sistema eléctrico español*, (Red Eléctrica de España, 2013).

[Reddy-2005] J.N. Reddy, *An introduction to the finite element method, third ed.,* (McGraw-Hill, New York, 2005).

[Repän-2014] T. Repän, S. Pikker, L. Dolgov, A. Loot, J. Hiie, M. Krunks, and I. Sildos, "Increased efficiency inside the CdTe solar cell absorber caused by plasmonic metal nanoparticles", *Energy Procedia* **44** 229-233, (2014).

[Santos-2010] A. Santos, P. Formentín, J. Pallarés, J. Ferré-Borrull, and L.F. Marsal, "Fabrication and characterization of high-density arrays of P3HT nanopillars on ITO/glass substrates", *Sol. Energy Mater. Sol. Cells* **94** 1247-1253, (2010).

[Service-2011] R.F. Service, "Outlook Brightens for Plastic Solar Cells", *Science* **332** 293-293, (2011).

[Shalabney-2011] A. Shalabney, and I. Abdulhalim, "Sensitivity-enhancement methods for surface plasmon sensors", *Laser Photonics Rev.* **5** 571-606, (2011).

[Shang-2011] Y. Shang, Q. Li, L. Meng, D. Wang, and Zhigang Shuai, "Computational characterization of organic photovoltaic devices", *Theor. Chem. Acc.* **129** 291-301 (2011).

[Spanggaard-2004] H. Spanggaard, and F.C. Krebs, "A brief history of the development of organic and polymeric photovoltaics", *Sol. Energ. Mat. Sol. C.* **83** 125-146**,** (2004).

[Stiles-2008] P.L. Stiles, J.A. Dieringer, N.C. Shah, and R.P. Van Duyne, "Surface-enhanced Raman spectroscopy", *Annu. Rev. Anal. Chem.* **1**, 601-626, (2008).

[Synowicki-1998] R.A. Synowicki, "Spectroscopic ellipsometry characterization of indium tin oxide film microstructure and optical constants", *Thin Solid Films* **313** 394-397, (1998).

[Tang-1986] C.W. Tang, "Two-layer organic photovoltaic cell," Appl. Phys. Lett., vol. 48, issue 2, pp. 183–185, Jan. 1986

[Van Dijken-2011] J.G. Van Dijken, M.D. Fleischauer, and M.J. Brett, "Controlled nanostructuring of CuPc thin films *via* glancing angle deposition for idealized organic photovoltaic architectures", *J. Mater. Chem.* **21** 1013-1019, (2011).

[Wang-2011] H. Wang, H.Y. Wang, B.R. Gao, L. Wang, Z.Y. Yang, X.B. Du, Q.D. Chen, J.F. Song, and H.B. Sun, "Exciton diffusion and charge transfer dynamics in nano phase-separated P3HT/PCBM blend films", *Nanoscale* **3** 2280-2285, (2011).

[Wiedemann-2010] W. Wiedemann, L. Sims, A. Abdellah, A. Exner, R. Meier, K.P. Musselman, J.L. MacManus-Driscoll, P. Müller-Buschbaum, G. Scarpa, P. Lugli, and L.

Schmidt-Mende, “Nanostructured interfaces in polymer solar cells”, *Appl. Phys. Lett.* **96** 263109, (2010).

[Würfel-2009] P. Würfel, *Physics of solar cells: From basic principles to advanced concepts, second ed.*, (Wiley, Weinheim, 2009).

[Xu-2009] Z. Xu, L.M. Chen, G. Yang, C.H. Huang, J. Hou, Y. Wu, G. Li, C.S. Hsu, and Y. Yang, “Vertical phase separation in poly(3-hexylthiophene):fullerene derivative blends and its advantage for inverted structure solar cells”, *Adv. Funct. Mater.* **19** 1227-1234, (2009).

[Xue-2004] J.G. Xue, S. Uchida, B.P. Rand, and S.R. Forrest, “Asymmetric tandem organic photovoltaic cells with hybrid planar-mixed molecular heterojunctions”, *Appl. Phys. Lett.* **85** 5757-5759, (2004).

[Yang-2005] F. Yang, M. Shtein, and S.R. Forrest, “Controlled growth of a molecular bulk heterojunction photovoltaic cell”, *Nature Mater.* **4** 37-41, (2005).

[Yang-2008] F. Yang, and S.R. Forrest, “Photocurrent generation in nanostructured organic solar cells”, *ACS Nano* **2** 1022-1032, (2008).

[Yu-1995] G. Yu, J. Gao, J.C. Hummelen, F. Wudl, and A.J. Heeger, “Polymer photovoltaic cells: Enhanced efficiencies via a network of internal donor-acceptor heterojunctions”, *Science* **270** 1789-1791, (1995).

[Yu-2011] S. Yu, C. Klimm, P. Schäfer, J.P. Rabe, B. Rech, and N. Koch, “Organic photovoltaic cells with interdigitated structures based on pentacene nanocolumn arrays”, *Org. Electron.* **12** 2180-2184 (2011).

UNIVERSITAT ROVIRA I VIRGILI
DESIGN AND MODELLING OF INTERDIGITATED AND NANOSTRUCTURED POLYMER SOLAR CELLS
Pedro Granero Secilla
Dipòsit Legal: T 891-2015

[Zeng-2014] S. Zeng, D. Baillargeat, H.P. Ho, and K.T. Yong, "Nanomaterials enhanced surface plasmon resonance for biological and chemical sensing applications", *Chem. Soc. Rev.* **43** 3426-3452, (2014).

[Zheng-2009] Y. Zheng, R. Bekele, J. Ouyang, and J. Xue, "Organic photovoltaic cells with vertically aligned crystalline molecular nanorods", *Org. Electron.* **10** 1621-1625, (2009).

UNIVERSITAT ROVIRA I VIRGILI
DESIGN AND MODELLING OF INTERDIGITATED AND NANOSTRUCTURED POLYMER SOLAR CELLS
Pedro Granero Secilla
Dipòsit Legal: T 891-2015

UNIVERSITAT ROVIRA I VIRGILI
DESIGN AND MODELLING OF INTERDIGITATED AND NANOSTRUCTURED POLYMER SOLAR CELLS
Pedro Granero Secilla
Dipòsit Legal: T 891-2015

UNIVERSITAT ROVIRA I VIRGILI
DESIGN AND MODELLING OF INTERDIGITATED AND NANOSTRUCTURED POLYMER SOLAR CELLS
Pedro Granero Secilla
Dipòsit Legal: T 891-2015

UNIVERSITAT ROVIRA I VIRGILI
DESIGN AND MODELLING OF INTERDIGITATED AND NANOSTRUCTURED POLYMER SOLAR CELLS
Pedro Granero Secilla
Dipòsit Legal: T 891-2015

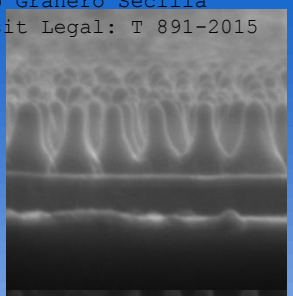

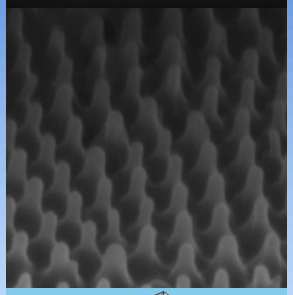

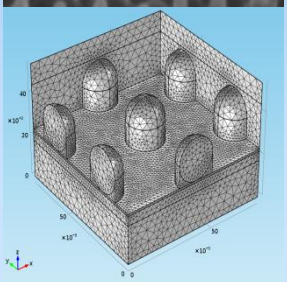

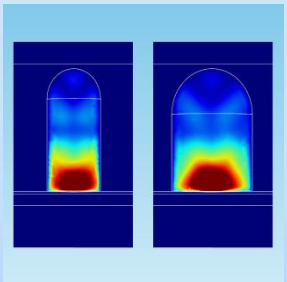

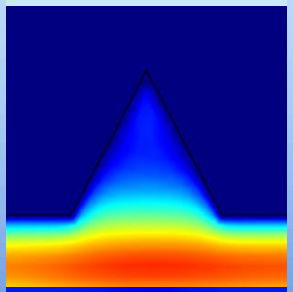

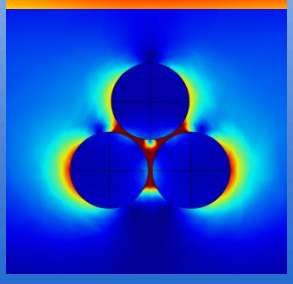

UNIVERSITAT ROVIRA I VIRGILI

Tarragona

2015